

Instituto Tecnológico y de Estudios Superiores de Monterrey

Campus Monterrey

School of Engineering and Sciences



**MODELLING AND POWER QUALITY ASSESSMENT OF AN ELECTROLYTIC  
CLEANING LINE IN THE STEEL-MAKING INDUSTRY**

A thesis presented by

**César Eduardo Suárez Guerrero**

Submitted to the

School of Engineering and Sciences

in partial fulfillment of the requirements for the degree of

**Master of Science in Energy Engineering**

Monterrey, Nuevo León

May 2017



Instituto Tecnológico y de Estudios Superiores de Monterrey

Campus Monterrey

School of Engineering and Sciences

The committee members, hereby, certify that have read the thesis presented by **César Eduardo Suárez Guerrero** and that it is fully adequate in scope and quality as a partial requirement for the degree of Master of Science in Energy Engineering.

---

**Armando Rafael Llamas Terrés, Ph.D.**

Tecnológico de Monterrey  
School of Engineering and Sciences  
Principal Advisor

---

**Oswaldo Miguel Micheloud Vernackt, Ph.D.**

Tecnológico de Monterrey  
Committee Member

---

**Raúl Jaime Acosta Cavazos, M.Sc.**

Ternium México  
Committee Member

---

**Rubén Flores O., B.S.**

Ternium México  
Committee Member

---

**Rubén Morales Menéndez, Ph.D.**

Dean of Graduate Studies  
School of Engineering and Sciences

Monterrey, Nuevo León

May 2017





## Declaration of Authorship

I, **César Eduardo Suárez Guerrero**, declare that this thesis titled, **“Modelling and Power Quality Assessment of an Electrolytic Cleaning Line in the Steel-Making Industry”** and the work presented in it are my own. I confirm that:

- This work was done wholly or mainly while in candidature for a research degree at this University.
- Where any part of this thesis has previously been submitted for a degree or any other qualification at this University or any other institution, this has been clearly stated.
- Where I have consulted the published work of others, this is always clearly attributed.
- Where I have quoted from the work of others, the source is always given. With the exception of such quotations, this thesis is entirely my own work.
- I have acknowledged all main sources of help.
- Where the thesis is based on work done by myself jointly with others, I have made clear exactly what was done by others and what I have contributed myself.

---

César Eduardo Suárez Guerrero  
Monterrey, Nuevo León, May 2017

@2017 by César Eduardo Suárez Guerrero  
All rights reserved



## **Dedication**

*To my mother, Lupita*

*To my sisters, Karen and Sofia*

*To my friends and family*



## **Acknowledgements**

I would like to firstly thank my mother Lupita, who has been a paragon of strength, patience, and tenacity all my life. Her support in all my endeavors and decisions has been key in achieving my goals until this point.

I also thank my sisters, Karen and Sofía, and my family for their unyielding support of my life endeavors.

Thanks to Ternium México for believing in national talent and its potential to make a difference in the current socioeconomic context, and giving me the opportunity to study in such a renowned institution.

Thanks to Tecnológico de Monterrey for having the foresight of having programs to attract talented students and professors, and facilitating them the tools needed in order for their research to have meaningful results.

I would also like to thank Dr. Osvaldo Micheloud, who trusted me with a scholarship through the Industrial Consortium, and gained my respect by going beyond his due in his support of his students under the belief that nurturing research is something that must be done for the wellbeing and further growth of this country, even being a foreigner himself.

Thanks to Dr. Armando Llamas, my mentor while developing this research project. An excellent guide through this challenge, who was always available when the need arose and provided helpful advice and guidance during my studies at this school. He is, undoubtedly, a big part on why this project came to a satisfactory result.

Thanks to Raúl Acosta and Rubén Flores from Ternium for taking some of their time to revise and give their opinions about this document.

Thanks to all the personnel I had the privilege to interact with at Pesquería Plant, with a special mention to José Luis Bosques for his disposition and commitment to this project while dealing with his daily occupations.

A special mention to the people at Ahorro y Calidad de Energía Eléctrica for their helpful advice and support concerning the devices used while developing this thesis.

Thanks to my friends at the Consortium for having my back through this journey.



# MODELLING AND POWER QUALITY ASSESSMENT OF AN ELECTROLYTIC CLEANING LINE IN THE STEEL-MAKING INDUSTRY

by

César Eduardo Suárez Guerrero

## **Abstract**

This thesis deals with the analysis of the electrical operating conditions in an Electrolytic Cleaning line located inside a relatively new steel-making factory property of Ternium México, and the process to obtain a functional model of the main loads' circuit using the commercial software MATLAB/Simulink. The motivation for this project was the appearance of several problems in components – whose severity and frequency were not contemplated during the initial design – that were initially believed to stem from Power Quality issues, and a desire to understand the impact that some planned modifications might have in the entire subsystem. In order to validate the data obtained through the simulated model, several pieces of equipment were used to either continuously capture and verify data during normal operation for a period of four weeks or to obtain data at several different occasions during a six-month timeframe. Meanwhile, the aforementioned computer model was being improved by including real-life parameters and characteristics in order to prepare for the eventual simulation. When that was done, the model was fed with data concerning the behavior that devices like an AFE or FOC-based drives would have during normal processing of a roll going through the line. The obtained results were thus contrasted against the actual data obtained by the different measurement devices, producing a discussion centered on the Power Quality attributed of both datasets oriented specifically towards harmonic distortion and its reduction. Finally, several recommendations are given to reduce the effects that were found during the simulation and the various field inspections done during the execution of the project while emphasizing possible avenues of improvement for prospective future work.





## List of Figures

Figure 1.1. Percent distribution of industrial energy consumption [32].....	1
Figure 1.2. Steel production schema [31].....	2
Figure 2.1. Graphic representation of both kinds of transient phenomena [11] .....	9
Figure 2.2. A momentary fault-induced interruption [11].....	10
Figure 2.3. A sag produced by a Single Line to Ground (SLG) fault [11].....	11
Figure 2.4. An instantaneous voltage swell [11].....	11
Figure 2.5. Waveform and spectrum content of a full-wave diode rectifier .....	12
Figure 2.6. Notching due to electronic device operation [11].....	13
Figure 2.7. Overcharge/Bonification incentives curve given by CFE formulae [15] .....	15
Figure 2.8. Skin effect in conductors .....	18
Figure 2.9. PCC distribution example [27] .....	20
Figure 2.10. Space vector .....	23
Figure 2.11. Sine-triangle modulation .....	26
Figure 2.12. Regular-sampled PWM.....	27
Figure 2.13. SVM sextant with all possible combinations, with an initial reference vector....	28
Figure 2.14. Three-phase active rectifier with leading LCL filter [14].....	29
Figure 2.15. Basic control scheme in an AFE device [30] .....	30
Figure 2.16. Basic circuit representation of AFE system, seen from rectifier side .....	30
Figure 2.17. Main PI controllers involved in AFE operation [25] .....	31
Figure 2.18. Current loop with I/O linearization.....	33
Figure 2.19. AFE behavior in presence of a voltage notch.....	34
Figure 2.20. Phase-to-Ground voltage with a 6-pulse rectifier and an AFE.....	34
Figure 2.21. DC overvoltage produced by common-mode current [8].....	35
Figure 2.22. FOC scheme for a three-phase machine .....	36
Figure 3.1. Main activities of the project .....	37
Figure 3.2. Cold Rolling processes present in Pesquería Plant .....	38
Figure 3.3. Electrolytic Cleaning Line in Steelmaking.....	39
Figure 3.4. One-line representation of the electrical substation.....	40
Figure 3.5. Shared bus by the mentioned lines.....	40
Figure 3.6. Operating values of the transformer .....	41
Figure 3.7. AFE Power Circuit [25] .....	42

Figure 3.8. One-line diagram, AC side.....	43
Figure 3.9. One-line diagram, Tension Reel load .....	44
Figure 3.10. Voltage and current waveforms, 100 ms sample .....	45
Figure 3.11. DC bus voltage during a minute sample .....	45
Figure 3.12. Voltage and current spectrum, 100 ms sample .....	46
Figure 3.13. Current and voltage probes during measurements.....	47
Figure 3.14. Data comparison between PQ sources .....	48
Figure 3.15. Harmonic content in both ECL AFE input currents .....	49
Figure 3.16. Comparison between both systems' Phases A, B, and C, respectively .....	50
Figure 3.17. Waveform from the main and auxiliary loads, respectively .....	51
Figure 3.18. Spectrum from both circuits, with cursor over the 19 <sup>th</sup> harmonic.....	51
Figure 3.19. HMI and dedicated device showing PF (a - No load b - Full speed) .....	52
Figure 3.20. ION measurement devices for the 13.8 kV bus .....	52
Figure 3.21. Pickling One-Line Diagram (Fragment).....	53
Figure 3.22. Waveform and spectrum of Phase A in Pickling .....	53
Figure 3.23. Data stickers placed on the LCL filter.....	56
Figure 3.24. Electric diagram of current LCL Filter in EC line .....	57
Figure 3.25. Common-mode capacitor condition in EC line .....	58
Figure 3.26. Common-mode capacitor condition in Pickling line.....	58
Figure 3.27. Data mask for Tension Reel load.....	59
Figure 3.28. Inverter portion of the modelled system in Simulink .....	60
Figure 3.29. Internal schematic of modelled motor drive .....	61
Figure 3.30. DC Bus Conditioner plate data.....	62
Figure 3.31. Tension Reel Data during roll processing in ibaAnalyzer .....	63
Figure 3.32. File types accepted as reference.....	64
Figure 3.33. Rectifier portion of the modelled system in Simulink.....	66
Figure 3.34. Modelled Active Front End control structure .....	67
Figure 3.35. Interface mask for the LCL filter and the Active Front End .....	68
Figure 3.36. DC and Current Controller, and timing compensation in modelled AFE .....	70
Figure 4.1. Voltage pattern during simulation.....	71
Figure 4.2. Current pattern during simulation period.....	72
Figure 4.3. RMS current during operation .....	72

Figure 4.4. Full simulation model .....	73
Figure 4.5. Power Distribution during simulation.....	74
Figure 4.6. Active and reactive power during roll processing.....	75
Figure 4.7. Simulation Power Factor.....	76
Figure 4.8. Average power factor, per phase.....	76
Figure 4.9. LPF operation, 100 ms sample.....	77
Figure 4.10. Harmonic spectrum for 100 ms sample during LPF operation.....	77
Figure 4.11. HPF operation, 100 ms sample.....	78
Figure 4.12. Harmonic spectrum for 100 ms during HPF operation.....	78
Figure 4.13. Simulation results during full speed processing, 100 ms sample .....	79
Figure 4.14. Harmonic content during simulation, 100 ms sample during full speed .....	80
Figure 4.15. DC Voltage and Current .....	80
Figure 4.16. Stator current and Torque, Tension Reel .....	81
Figure 4.17. Rotor and roll speed, Tension Reel.....	81
Figure 4.18. Single phase equivalent of the harmonic circuit.....	82
Figure 4.19. Voltage amplification according to Equation 4.4 .....	85
Figure 4.20. Frequency response simulation .....	85
Figure 4.21. Frequency response results in Simulink .....	85
Figure 4.22. Wire organization at transformer output .....	86
Figure 4.23. Damped frequency response.....	87
Figure 4.24. LCL damping switching circuit .....	88
Figure 4.25. Currents and harmonic spectrum with no damping resistor .....	89
Figure 4.26. Currents and harmonic spectrum with 0.1 $\Omega$ damping resistor .....	89
Figure 4.27. Currents and harmonic spectrum with a 0.3 $\Omega$ damping resistor .....	89
Figure 4.28. Three-phase power consumption, 0.1 $\Omega$ and 0.3 $\Omega$ respectively.....	90



## List of Tables

Table 2.1. Characteristics of Power Quality phenomena, IEEE 1159-2009 [11].....	8
Table 2.2. Characteristic harmonics of rectifier constructions.....	17
Table 2.3. Change in resistance due to skin effect [15]. ....	19
Table 2.4. Harmonic rotation pattern [15] .....	19
Table 2.5. Voltage distortion limits (IEEE Std 519-2014) [10] .....	21
Table 2.6. Current distortion levels (120 V – 69 kV) [10].....	21
Table 2.7. Current distortion levels (69 kV – 161 kV) [10].....	22
Table 2.8. Current distortion levels (> 161 kV) [10].....	22
Table 3.1. AFE modelling parameters.....	54
Table 3.2. Drive parameters .....	55
Table 3.3. Physical Characteristics of line motors .....	56
Table 3.4. LCL Filter electrical data (per-phase).....	57
Table 3.5. Transformer impedance data .....	68



## Contents

<b>Abstract.....</b>	<b>VII</b>
<b>List of Figures.....</b>	<b>IX</b>
<b>List of Tables .....</b>	<b>XIII</b>
<b>I. Introduction .....</b>	<b>1</b>
1.1. Description and Objectives for the Work.....	3
1.2. Structure of the Work.....	4
<b>II. Theoretical Framework.....</b>	<b>7</b>
2.1. Power Quality .....	7
2.1.1. Transients.....	9
2.1.2. Voltage Variations .....	10
2.1.3. Imbalance.....	11
2.1.4. Waveform distortion.....	12
2.2. Power Factor and Harmonics .....	14
2.3. Rectifier and Inverter Configurations.....	23
2.3.1. Space Vectors.....	23
2.3.2. Gate Logic Generation .....	25
2.3.3. Active Front End.....	28
2.3.4. Field-Oriented Control Drives.....	35
<b>III. Methodology .....</b>	<b>37</b>
3.1. Field Data Recollection .....	38
3.2. Data Verification.....	47
3.3. Device Characterization.....	54
3.4. Load Modelling.....	59
3.5. Rectifier Modelling.....	65

<b>IV. Results and Discussion .....</b>	<b>71</b>
4.1. LCL Filter Resonance.....	82
<b>V. Conclusions and Recommendations .....</b>	<b>91</b>
<b>VI. Future Work .....</b>	<b>93</b>
<b>Annex I.....</b>	<b>95</b>
<b>Annex II .....</b>	<b>97</b>
<b>Annex III.....</b>	<b>99</b>
<b>References.....</b>	<b>105</b>
<b>Curriculum Vitae .....</b>	<b>109</b>



## I. Introduction

Energy consumption has been one of the most relevant topics in the last decade. The increasing focus it has in political and economic circles has put the heat on dedicated research as the general populace shows their preference towards a greener and leaner generation/distribution grid – a tendency that is going to have drastic effects in how the industry manages their own processes to fulfill their own energy and environmental goals, either by law or by self-motivation.

Its relevancy comes from the fact that the industrial sector has the biggest share in consumption of end-use energy than any other one, being equivalent to around 54% of the world's total delivered energy while having a projected growth of 1.2% per year according to data of the U.S. Department of Energy [32]. The biggest part of this surge is expected in the developing world as their industrialization marches on and their integration to the world economy keeps increasing.

Of the increasingly complex industrial matrix, several branches are considered as energy-intensive: food, pulp and paper, basic chemicals, refining, iron and steel, nonferrous metals, and nonmetallic minerals [32]. As **Figure 1.1** shows, together they consolidate half of energy consumption in their category for OECD countries while keeping similar growth patterns for the rest of the world.

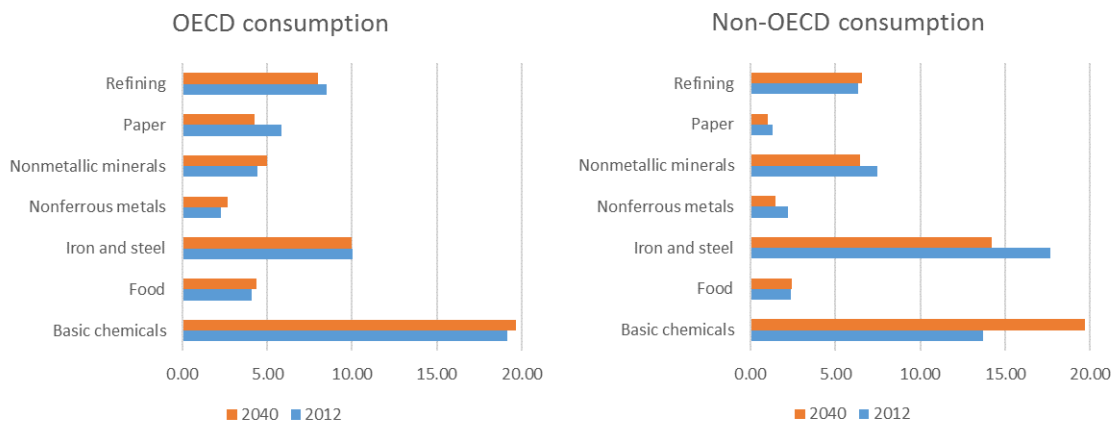


**Figure 1.1.** Percent distribution of industrial energy consumption [32]

From inspection of the previous graphs, it can be surmised that one of the biggest players when dealing with the use of energy is the iron and steel sector, which captures an average global demand of around 10%. This can be explained when considering the diverse processes involved in this industry to produce each step of the value chain, marking the production of a single roll or slab of steel with a predictably substantial amount of invested energy – either in the form of thermal or electric energy. A glance of how big the steel production grid may become in a company can be seen in **Figure 1.2**.

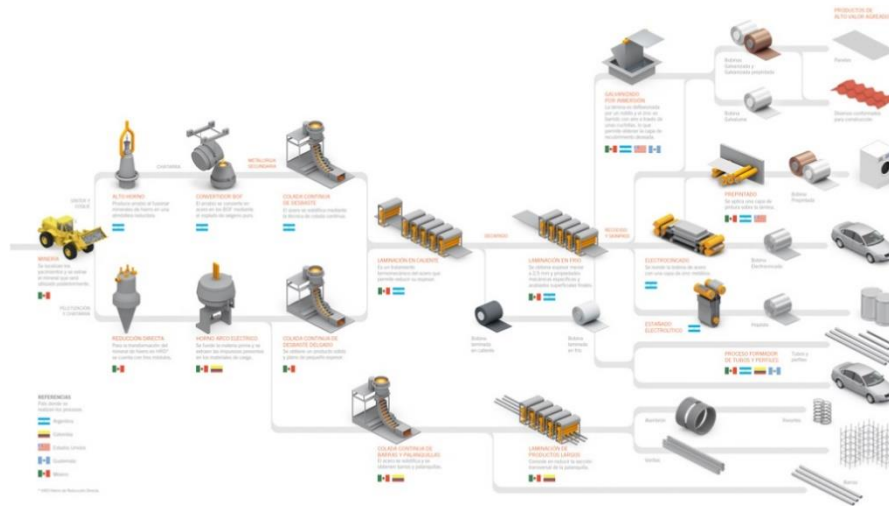


**Figure 1.2.** Steel production schema [31]

But even if the processes are as diversified as shown, there is a constant within this sector and the whole industrial apparatus: electric motors dominate by a large margin the total consumption of electricity. It is estimated that they account between 43% and 46% of all global use of this form of energy, simultaneously leading to an annual amount of emissions around 6,040 Mt of CO<sub>2</sub> [34]. When limiting to their uses and applications inside the steelmaking industry, a DOE-commissioned report indicates that they totaled a share of 7% of the total sector energy demand [35].

And as automation marches on, their use will only go up. It is predicted that by 2030 the yearly global consumption will reach 13,360 TWh per year – an increase that is going to be reflected by a ballooning expenditure upwards USD 900 billion just in electricity charges by end-users [34]. And considering that energy represents around 20% of the total steel manufacturing costs, an important increase in energy costs coming from both the introduction

of specialized equipment and the expected increase in the cost of fuels is bound to eventually make a serious impact in the industry composition and the market [35].

Understanding that, it is not surprising that many of the internal efforts inside companies rely on energy efficiency programs to alleviate this upcoming scenario. It is typical to find them centered around activities such as motor management and maintenance planning, proper sizing of loads (with a preference towards energy-efficient constructions), or power factor correction. Such activities need a deep understanding of the systems involved to recognize how certain modifications and/or configurations can modify its performance, either in a positive or negative way.

It is in this context where the focus of the present document clears, which is centered around the analysis of an Electrolytic Cleaning line property of Ternium México, specifically located in Pesquería Plant. As it is a recent operation, it is of interest of the company to understand the reasons behind the situation that has appeared since its initial commissioning.

For this work, a Power Quality analysis was done to clarify the conditions in which the line was working at the time, which also doubles as a reference framework to compare against the results of a simulation made in the block-based software Simulink, an element of the MATLAB environment.

### **1.1. Description and Objectives for the Work**

Ternium México has codified in its corporate policy the continuous improvement of their production processes, including in those goals an ever-increasing energy efficient workload and the proper management of the involved machinery. Nevertheless, the Electrolytic Cleaning line in its newest industrial complex has shown certain problems that the Electrical Maintenance personnel attribute to a suboptimal design that entails Power Quality events. Although certain modifications have been suggested by the manufacturer of the equipment, it is of their interest to understand and have substantiated evidence of their impact that such changes would have in the general performance of the line.

The main objective of this project was to produce a model using the MATLAB/Simulink environment able to reproduce the operational conditions of the main loads corresponding to

the Electrolytic Cleaning line active in the Pesquería complex, in order to judge how the parameters of the mentioned system interact between them and be able to offer palliatives to undesired developments.

To reach that goal, a subset of objectives was defined:

- Define in a clear manner the current situation experienced in the system.
- Obtain both system parameters and working data during normal operation.
- Produce an acceptable working model of the system.
- Compare data from both sources and give recommendations.

## **1.2. Structure of the Work**

In this section, a small description of the sections that compose this document is presented to the reader.

Chapter 1, the Introduction, mainly deals with the motivations and the scope that encapsulate the current work. How energy has become a bigger issue for the industry and the context that leads to the rise and focus of efficiency programs, specifically in the Iron & Steel sector. The limits of what is going to be touched with the results presented by this document are given to the reader to temper expectations, so the main structure may be rationalized and understood.

The Theoretical Framework is explained through Chapter 2, starting with concepts related to Power Quality and the standards related to them, touching upon the characteristics of the events surrounding this concept and how it interacts with the equipment located in the area. Meanwhile, the second part of this section deals with how the electrical power fed to the system passes through different control schemas to be produce the work carrying the production process. More precisely, the fundamentals of both the active rectifier and the inverters feeding the loads are explained to familiarize the reader with the elements composing the simulation.

The Methodology expanded upon in Chapter 3 encapsulates both the actions taken on site with the physical measurement devices and the development of the model in Simulink in order to successfully characterize the system in question. Also, the reasoning for any differences or conceptions taken during the creation of the model are taken into account through the entire chapter.

Chapter 4 is composed of the Results and Discussion part of the document. After obtaining data from real operation and contrasting it with the set obtained through the simulation of a whole process cycle with the model, a discussion of the meaning of what was obtained, the contrasts between reality and the model, and the possibilities concerning the potential improvement of operation are all touched upon.

Finally, Conclusions and Future Work are contemplated in Chapter 5 and 6 of the present document, explaining how the objectives were achieved and the recommendations that were reached after the analysis of all recovered data. Failings and prospective work threads are also given for further consideration.



## II. Theoretical Framework

### 2.1. Power Quality

The concept of Power Quality encapsulates the capacity of an electrical distribution system to feed power to a system without producing undesirable effects while doing so. This becomes important when characterizing the types of loads that are dependent on a power source, with two categories being relevant:

- A load is considered *critical* when it cannot be disconnected from a voltage source without risking technical and/or economic losses, and potentially endangering human lives [16].
- A *sensitive* load can be defined as one with specific needs of a constant supply of voltage and current, with defined characteristics in order for it to work properly [16].

A grid with elements corresponding to either type of load is more sensitive to problems in the voltage or the current circling through the system, making Power Quality events a concern when dealing with the expected performance of a system. Its relevancy only becomes greater when considering the changes in the grids.

In the last couple of decades the composition of the interconnected distribution networks has progressively changed, as more nonlinear loads enter (such as computers or drive systems) and affect equipment that was not designed for an erratic grid or needs specific characteristics that may not be found in current operation, resulting from neglected data during the initial analysis or modifications during the timeframe between concept and commissioning.

It is desirable to understand how the increasing use of electronics capable of producing electromagnetic disturbances affects sensitive equipment, although segments of both the Electronics and the Power Quality community have used different terms to define the same phenomena [11]. This document uses the widely extended recommended practice published by the Institute of Electrical and Electronics Engineers (IEEE), the Standard 1159, which uses the electromagnetic compatibility concept to describe such phenomena. In said document, a classification for the different Power Quality events was developed, shown in **Table 2.1**.

**Table 2.1.** Characteristics of Power Quality phenomena, IEEE 1159-2009 [11]

Categories	Typical spectral content	Typical duration	Typical voltage magnitude
1.0. Transients			
1.1 Impulsive			
1.1.1 Nanosecond	5 ns rise	< 50 ns	
1.1.2 Microsecond	1 $\mu$ s rise	50 ns – 1 ms	
1.1.3 Millisecond	0.1 ms rise	> 1 ms	
1.2 Oscillatory			
1.2.1 Low frequency	< 5 kHz	0.3–50 ms	0–4 pu
1.2.2 Medium frequency	5–500 kHz	20 $\mu$ s	0–8 pu
1.2.3 High frequency	0.5–5 MHz	5 $\mu$ s	0–4 pu
2.0 Short-duration root-mean-square (rms) variations			
2.1 Instantaneous			
2.1.1 Sag		0.5–30 cycles	0.1–0.9 pu
2.1.2 Swell		0.5–30 cycles	1.1–1.8 pu
2.2 Momentary			
2.2.1 Interruption		0.5 cycles – 3 s	< 0.1 pu
2.2.2 Sag		30 cycles – 3 s	0.1–0.9 pu
2.2.3 Swell		30 cycles – 3 s	1.1–1.4 pu
2.3 Temporary			
2.3.1 Interruption		>3 s – 1 min	< 0.1 pu
2.3.2 Sag		>3 s – 1 min	0.1–0.9 pu
2.3.3 Swell		>3 s – 1 min	1.1–1.2 pu
3.0 Long duration rms variations			
3.1 Interruption, sustained		> 1 min	0.0 pu
3.2 Undervoltages		> 1 min	0.8–0.9 pu
3.3 Overvoltages		> 1 min	1.1–1.2 pu
3.4 Current overload		> 1 min	
4.0 Imbalance			
4.1 Voltage		steady state	0.5–2%
4.2 Current		steady state	1.0–30%
5.0 Waveform distortion			
5.1 DC offset		steady state	0–0.1%
5.2 Harmonics	0–9 kHz	steady state	0–20%
5.3 Interharmonics	0–9 kHz	steady state	0–2%
5.4 Notching		steady state	
5.5 Noise	broadband	steady state	0–1%
6.0 Voltage fluctuations	< 25 Hz	intermittent	0.1–7% 0.2–2 P <sub>st</sub>
7.0 Power frequency variations		< 10 s	$\pm$ 0.10 Hz



### 2.1.1. Transients

A term used in the analysis of variations in power systems, it implies the notion of a momentary, undesirable event in the power supply. Although there is not a clearly defined limit in what exactly classifies as a transient or not, the most accepted view is that a phenomenon is treated like a transient when its duration is less than a cycle compared to the natural frequency of the studied system [11].

For the phenomena that classifies as such, transients are commonly subdivided according to the waveform of the current or voltage event:

- *Impulsive* transients are sudden, nonpower frequency changes from the nominal values of voltage, current, or both with unidirectional polarity, characterized by their rise and decay times [11]. Lightning commonly produces this kind of transients, like the one present in **Figure 2.1a**.
- *Oscillatory* transients, on the other hand, are sudden nonpower frequency changes in the steady-state condition of an electrical signal, including positive and negative values [11]. As such, it is described by magnitude, duration, and its spectral content. Capacitor bank maneuvers are often guilty of this type of transients, as seen in **Figure 2.1b**.

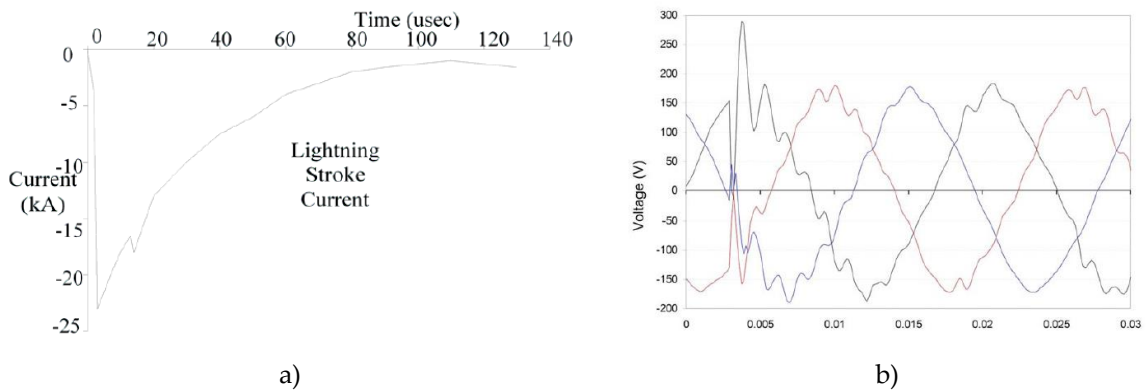


**Figure 2.1.** Graphic representation of both kinds of transient phenomena [11]

### 2.1.2. Voltage Variations

As its name suggests, this category encompasses any variation in the RMS value of voltage in an electrical system. They are almost always caused by faults at some point in the distribution grid, the connection of large loads, or by faulty wiring [11].

Depending on the location of such incidents, the system may experience a dip or a rise compared to the nominal voltage value – sags and swells – or a complete loss of energy – an interruption.

An *interruption* is differentiated from a sag or a swell because it corresponds to a decrease in system voltage equivalent to less than 10% of the nominal [11]. To be considered as momentary or temporary, it cannot endure beyond a minute – otherwise it is treated as permanent (so common protective devices cannot get rid of it) and manual intervention is needed to restore the power supply. **Figure 2.2** exemplifies a typical interruption.

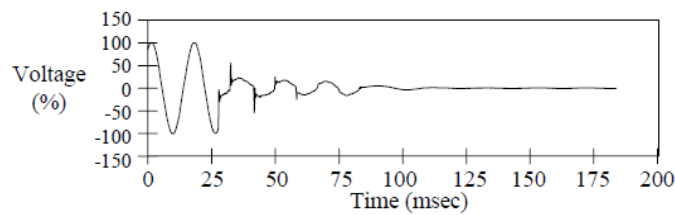


**Figure 2.2.** A momentary fault-induced interruption [11]

Meanwhile, a voltage *sag* is a decrease in RMS value between 0.1 and 0.9 pu, with durations starting from half a cycle to 1 minute. As the sag category encompasses multiple origin and effect possibilities, terminology can be quite varied; it is preferred to describe them in terms of remaining voltage compared to the nominal value [11]. Usually related to faults, they can also arise from the connection of large loads with high starting currents (See **Figure 2.3**). If the reduction lasts beyond 1 minute the event is considered an *undervoltage*, whose typical values hover around 0.8-0.9 pu.

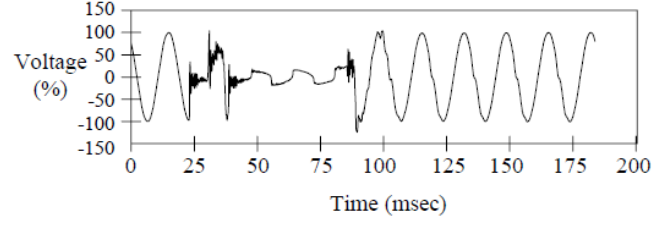


**Figure 2.3.** A sag produced by a Single Line to Ground (SLG) fault [11]

In counterpart, a voltage *swell* is an increase of the RMS value, typically between 1.1-1.2 pu (see **Figure 2.4**). It is described by the ratio between actual and nominal voltage of the system [11]. If it lingers for more than a minute, it is considered an *overvoltage*.

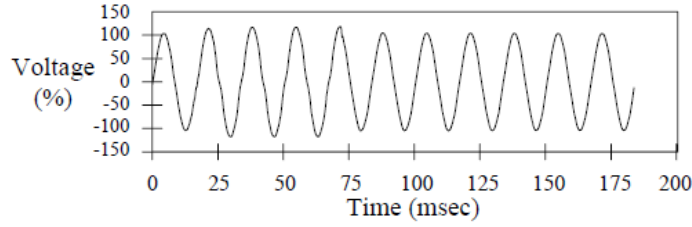


**Figure 2.4.** An instantaneous voltage swell [11]

### 2.1.3. Imbalance

Defined as the ratio of the magnitude of the negative sequence component to the magnitude of the positive sequence component of either voltage or current [11]. It is common to encounter voltage imbalance of around 3%, and it is not strange to find a 30% imbalance between three-phase currents.

Its mathematical expression is as follows, shown by **Equation 2.1**:

$$\% \text{ Imbalance} = \left| \frac{V_{neg}}{V_{pos}} \right| \times 100 \quad (2.1)$$

The standard prefers this definition instead of the one commonly used in measurement devices, which compare the deviation of a voltage against the average phase-to-phase value – exemplified by **Equation 2.2**. This is because it represents more closely the phenomena of interest, instead of relying in approximations and the error within those operations.

$$\% \text{ Imbalance} = \left| \frac{(V_m - V_{pp})}{V_{pp}} \right| \times 100 \quad (2.2)$$

#### 2.1.4. Waveform distortion

Like the previous category, it is a steady-state deviation from the ideal, sinusoidal power supply, but in this case the electric variable is mainly characterized by its spectral content [11]. There are 5 primary types of distortion touched upon the IEEE standard.

The first case deals with the presence of an injected DC voltage or current in an alternating current system, called *DC offset*. It can be detrimental due to increases in component saturation, and the heating associated to such development.

A second form of distortion is the one produced by the presence of sinusoidal *harmonics* in either voltage or current, whose frequencies are integer multiples of the system fundamental one (commonly 50 or 60 Hz) [11]. They appear because of the nonlinear nature of loads in the distribution grid, such as any electronically controlled device. The typical distortion of current shown in **Figure 2.5** of a diode-based, non-controlled rectifier is one of the simplest examples of the appearance of harmonic content in a network.

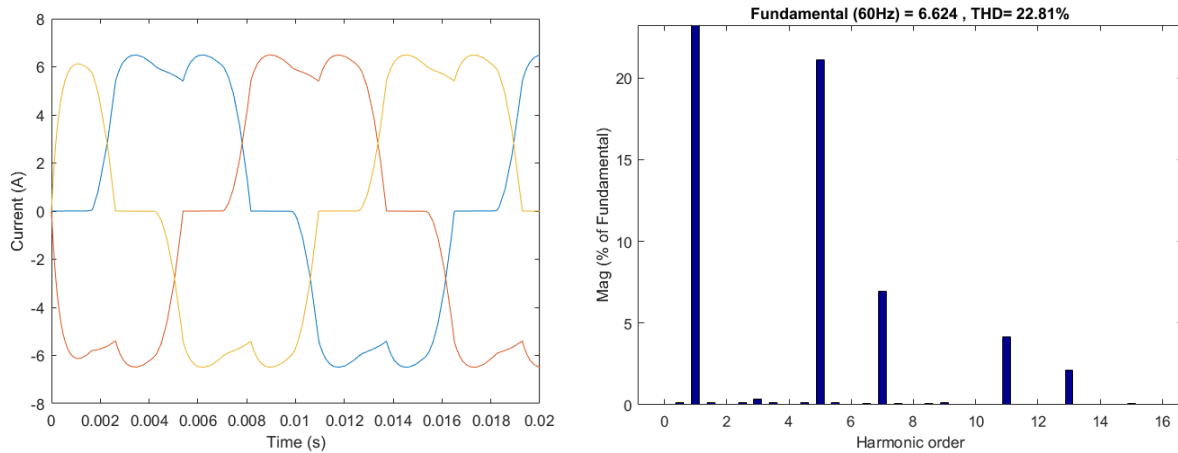


**Figure 2.5.** Waveform and spectrum content of a full-wave diode rectifier

As it is also shown in **Figure 2.5**, distortion levels produced by harmonics can be characterized by a quantity known as Total Harmonic Distortion (THD). This concept and its implications on system performance will be touched in more detail in the next section.

Of course, not only integer values of the fundamental frequency produce distortion in the waveform, as other voltages or currents may appear with discrete frequencies or as a spectrum. That kind of distortion is known as *interharmonics*, and can be found in a variety of networks [11].

Although their effects are not as studied as the ones from harmonics, it is common for their presence to be affecting carrier signaling and be involved in the appearance of flicker events.

Continuing with the pattern of power electronics-induced distortion appears the concept of *notching*, a periodic disturbance that occurs because of the commutation of devices such as diodes, thyristors or IGBTs. This kind of components work in two logic states, and switch their status – in the case they are controlled – at a fast rate. But even at their operation speed they are not completely instantaneous, so there are small periods where there is a short circuit between phases and thus, notching occurs (as seen in **Figure 2.6**).

Their intensity is determined by the source inductance and the insulating inductance between converter, the magnitude of the current and the monitored point.

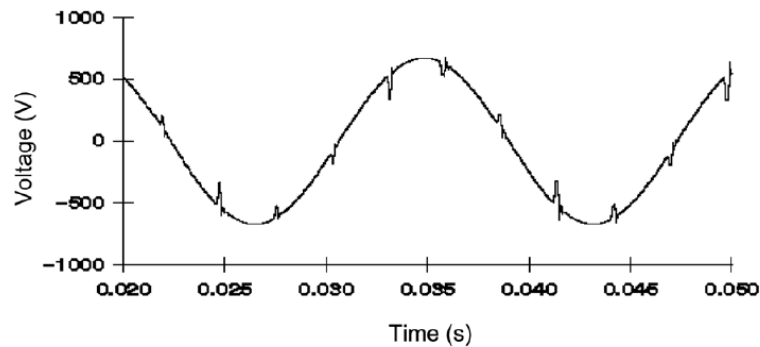


**Figure 2.6.** Notching due to electronic device operation [11]

## 2.2. Power Factor and Harmonics

One relevant quantity for industrial-level machinery is the power factor, which is defined in **Equation 2.3** as the ratio between the real and apparent power in a system [15]:

$$PF = \frac{P}{S} \quad (2.3)$$

In the case of an ideal sinusoidal power supply – or when dealing with the fundamental frequency – the previous equation can be simplified:

$$PF = \frac{P}{S} = \frac{VI \cos \theta}{VI}$$
$$PF = \cos \theta \quad (2.4)$$

Looking to **Equations 2.3** and **2.4** it can be surmised that an ideal power factor is unitary, so no reactive power is produced by the source as apparent and real power have the same magnitude. But in the case of inductive and capacitive loads such as motors and transformers the appearance of reactive currents is unavoidable to create the flux that those components need to work – which will inevitably lead to a fall in the power factor for those types of cases.

Nevertheless, it is important to maintain a reasonably high (90% or higher) value for the power factor so the system may be optimized while avoiding the penalties carried with the use of energy for unproductive purposes. Such goals are commonly tackled by energy efficiency programs inside the industry, as previously mentioned in the Introduction of the current document. It is common to see actions based on the correction of the power factor in distribution system, comprising but not limited to steps like [15]:

- The detection and replacement of overdimensioned motors.
- Installing capacitor banks.
- Installing overexcited synchronous machines.
- Installing filters, either passive or active.
- Installing reactive power compensators.

The reason for such focus in power factor improvement are the benefits obtained when correcting its value. Of those, one of the biggest economic incentives comes in the form of penalizations or bonifications from the power company in the electricity invoice.

In Mexico, the biggest player after the aperture of the Electrical Market, *Comisión Federal de Electricidad* (CFE), applies this measure to their industrial-level loads to promote an efficient and rational use of energy. Using a pair of internal formulas, the company can determine the level of either bonification or overcharge that an individual user will have reflected in their monthly billing, just like **Figure 2.7** illustrates.

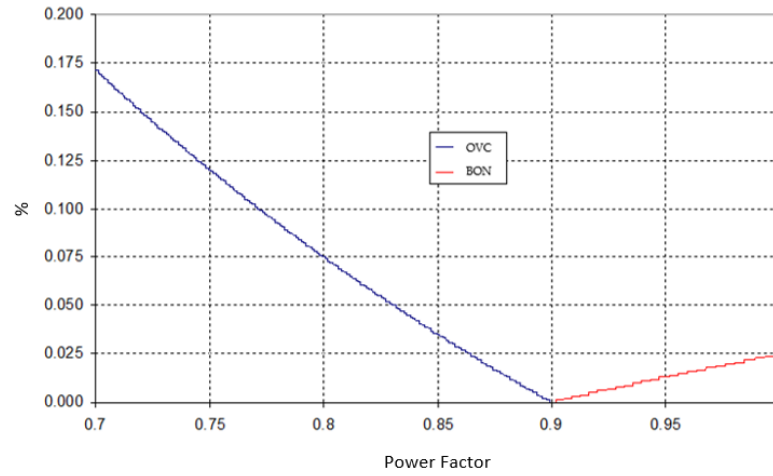


**Figure 2.7.** Overcharge/Bonification incentives curve given by CFE formulae [15]

Other of the benefits that comes with the correction of the power factor is the release of capacity used for reactive power, which allows the possibility of using the same equipment with an increase in loading. Also, as less current goes through the conductive elements in the system the  $I^2R$  losses will inevitably fall. This can be understood by reflecting the changes in the usual loss formula:

$$I_1 = \frac{P}{\sqrt{3}V_{pp}PF_1} \quad I_2 = \frac{P}{\sqrt{3}V_{pp}PF_2}$$

$$\Delta P_{loss} = 3(I_1^2 - I_2^2)R = 3 \frac{P^2}{3V_{pp}^2} \left( \frac{1}{PF_1^2} - \frac{1}{PF_2^2} \right) R$$

The loss reduction after the improvement of the power factor is:

$$\frac{\Delta P_{loss}}{P_{loss1}} = \frac{\frac{P^2}{V_{pp}^2} \left( \frac{1}{PF_1^2} - \frac{1}{PF_1^2} \right) R}{\frac{P^2}{V_{pp}^2} \left( \frac{1}{PF_1^2} \right) R}$$

$$\frac{\Delta P_{loss}}{P_{loss1}} = 1 - \left( \frac{PF_1}{PF_2} \right)^2 \quad (2.5)$$

A consideration must be made about the assumptions already done: The displacement angle between real and apparent power is not the only thing that affects the value of the power factor of a system. Harmonic distortion also plays a role in how much energy is used for useful purposes.

As it was already mentioned in the previous section, the ever-increasing number of nonlinear loads connected to power systems change the intrinsic sinusoidal shape of the AC current and voltage. This is the direct result of the injection of harmonic currents (and the possibility of voltage distortion) into the system, which may cause malfunctioning in elements sensitive to their presence [10].

This kind of electrical noise can be traced to equipment such as electronic converters, arc furnaces, static VAR systems, cycloconverters, rectifiers, and inverters. Those devices are the most common sources of harmonics found in modern industrial environments – each one of them with their own characteristic spectral behaviors and sensibilities.

For the specific case under study, the motor system employs both controlled rectifier and inverter circuits (explained with more detail at the next section). Specifically, as the rectifier is the element that directly interacts with the alternating current power supply, it is of interest to understand its interactions with the AC source. And regardless of its control specifications or the carrier frequency of its gate signal, all rectifiers follow a simple function by which its harmonic generation may be derived [1] [29], shown in **Equation 2.6**:

$$h = kp \pm 1 \quad (2.6)$$

Substituting  $k$  by any integer number, and replacing  $p$  by the number of pulses of the rectifier under study, a specific pattern of harmonics for each kind of energy converter



appears. **Table 2.2** shows the first ten characteristic harmonics of three different AC/DC converter architectures, based on their gate pulses.

**Table 2.2.** Characteristic harmonics of rectifier constructions

Pulses					Harmonics					
2	3	5	7	9	11	13	15	17	19	21
6	5	7	11	13	17	19	23	25	29	31
12	11	13	23	25	35	37	47	49	59	61

Of course, there is the possibility to find non-characteristic harmonic values when the system contains undesirable conditions, such as high imbalance in the network, high voltage distortion, or damaged semiconductor components. The presence of even harmonics is not expected in a properly working rectifier when only considering the structure of the device, so an important presence of them (higher than 3% of the fundamental value) may indicate a problem with the converter device [15].

One point to consider when dealing with harmonic content is how much of the demanded current (and voltage) corresponds to the fundamental frequency and is useful, and how much is being wasted in harmonic generation. This may be measured by THD data, mathematically defined in **Equation 2.7**, and exemplified by currents.

$$\%THD = \frac{Distortion\ RMS}{Fundamental\ RMS} = \frac{\sqrt{I_2^2 + I_3^2 + I_4^2 + \dots + I_h^2}}{I_1} \times 100 \quad (2.7)$$

THD calculation seems to include as many harmonic values as the user desires, but usually they are capped around the 50<sup>th</sup> order [29]. If higher harmonics are needed for a complete overview the limit may be changed to suit individual cases.

Another important concept to consider is the total effect of distortion at the Point of Common Coupling (PCC), known as Total Demand Distortion (TDD). Understood as a percentage of the maximum demand current, it is a ratio of the RMS value of the harmonic content to the RMS of the maximum demand load current, expressed as a percentage of the last value [29]. Its expression is shown in **Equation 2.8**.

$$\%TDD = \frac{\sqrt{\sum_{h=2}^{\infty} I_h^2}}{I_L} \times 100 \quad (2.8)$$

A large amount of harmonic distortion may not be a problem by itself, but depending of the configuration of a system it may bring havoc to its operation. Even if it is difficult to quantify their effects in a specific manner, they commonly show themselves in several ways:

*Cables and conductors.* When current goes through a conductive element, part of the energy it carries is lost because of the Joule effect ( $I^2R$  losses), where the current is a function of the current density and the transversal area of the cable. As the frequency of the transmitted signal increases, the effective area of the conductor starts to decrease as the majority of the current tends to be in the outer layer, increasing the heating losses. This phenomenon is called *skin effect* (see **Figure 2.8**), and it is only relevant in higher frequencies as those are not really considered by manufacturing [15]. An example in circular conductors is shown in **Table 2.3**.

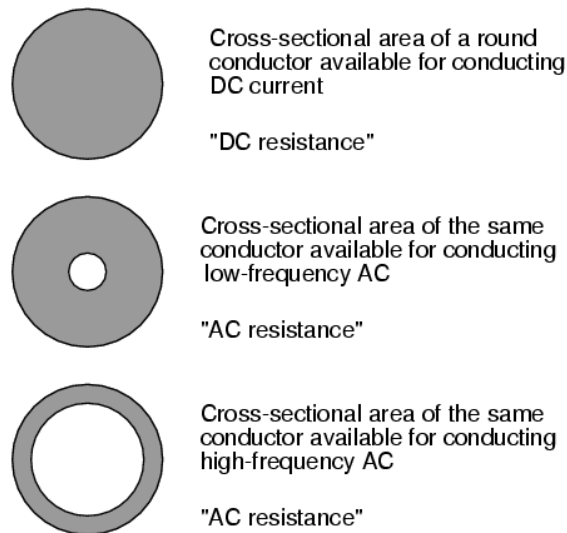


**Figure 2.8.** Skin effect in conductors

*Transformers.* The majority of transformers are designed to work at fundamental frequency (either 50 Hz or 60 Hz). They have losses by design that are augmented when harmonics enter a system. In the case of the core, these are either due to the mentioned skin effect or by Eddy currents, which are proportional the square of the load current and of the operating frequency.

Special attention must be put into  $\Delta/Y$  transformers, as harmonics that correspond to multiples of 3 will only stay in the wye-connection side risking overheating of both windings and the core [15].

**Table 2.3.** Change in resistance due to skin effect [15].

Conductor size	60 Hz resistance	300 Hz resistance
300 MCM	1.01	1.21
450 MCM	1.02	1.35
600 MCM	1.03	1.50
750 MCM	1.04	1.60

*Neutral bars.* Zero sequence currents, contrary to the case of positive and negative sequence ones, are not cancelled when entering the neutral bars but instead are tripled in a balanced load state – so there is a possibility of overloading them when dealing with nonlinear systems. This may become a problem when the predominant harmonics are in the zero sequence, as a pattern appears when increasing the value of the frequency (see **Table 2.4**).

**Table 2.4.** Harmonic rotation pattern [15]

h	1	2	3	4	5	6	7	8	9	10	11	12	13	14	15	16	17	18	19	20	21
Sequence	+	-	0	+	-	0	+	-	0	+	-	0	+	-	0	+	-	0	+	-	0

*System reactance.* The appearance of a harmonic that excites the resonant frequency of the system, either parallel or series, is a problem that may introduce undesired amplification of currents and voltages, as the equivalent admittance steers close to zero. The mentioned heating problems are exacerbated with such phenomenon alongside the needless operation of protective devices or the diminishing lifetime of devices.

Knowing the effects of electrical harmonics in equipment and in the overall stability of the distribution system is key to making efforts to diminish their negative impacts. As the management of harmonic distortion is responsibility of both end-users and the controller of the power supply, a middle ground must be reached as the variety of loads keeps increasing. So, considering the impact of their presence in a variety of loads, the IEEE established a recommended practice in their limits as the Standard 519.

As general goals, the IEEE recommends the levels of distortion shown in **Table 2.5** for voltage, while offering the data in **Table 2.6, 2.7, and 2.8** for currents at the Point of Common Coupling. The PCC is the point where the customer meets the utility, and it usually corresponds to the point between the utility transformer and the customer's facility transformer [27]. The standard defines the limits here for several reasons, one being the fact that the Power Company pays and is responsible for all infrastructure behind the PCC, while user bears the costs of their own distribution system. A helpful diagram can be found at **Figure 2.9**.

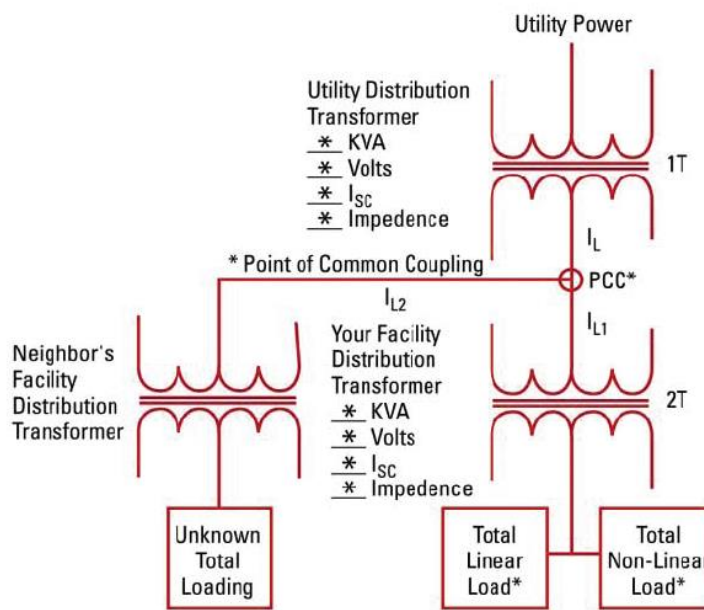


**Figure 2.9.** PCC distribution example [27]

Another reasoning is that going further downstream implies the consideration of local variations that may or may not apply to different systems. As such, the interested parties are encouraged to take such actions as its premise is the reduction of voltage distortion, but if keeping harmonic levels controlled is not enough to favorably modify the situation both players in power delivery should make the necessary changes to have an acceptable power supply [10].

On top of that, another consideration that must be done is that current distortion is based on the ratio between short-circuit current and load current. The short circuit value determines the stiffness of the supply – the higher value of it compared to the nominal current, the higher

allowed harmonic content [27]. Its value is easily obtained knowing the supply side impedance value and **Equation 2.9**.

$$I_{sc} \approx \frac{kVA_{nom}}{Z_{ss, pu} \times V_{secondary} \times \sqrt{3}} \quad (2.9)$$

As a note to all current related tables, the values shown there only apply to odd-numbered harmonics. For even-numbered ones the standard indicates that a 25% factor must be considered.

**Table 2.5.** Voltage distortion limits (IEEE Std 519-2014) [10]

Bus voltage at PCC	Individual harmonic (%)	THD (%)
$V \leq 1.0 \text{ kV}$	5.0	8.0
$1 \text{ kV} < V \leq 69 \text{ kV}$	3.0	5.0
$69 \text{ kV} < V \leq 161 \text{ kV}$	1.5	2.5
$161 \text{ kV} < V$	1.0	1.5

**Table 2.6.** Current distortion levels (120 V – 69 kV) [10]

$I_{sc}/I_L$	$3 \leq h < 11$	$11 \leq h < 17$	$17 \leq h < 23$	$23 \leq h < 35$	$35 \leq h < 50$	TDD
<b>&lt; 20</b>	4.0	2.0	1.5	0.6	0.3	5.0
<b>20 &lt; 50</b>	7.0	3.5	2.5	1.0	0.5	8.0
<b>50 &lt; 100</b>	10.0	4.5	4.0	1.5	0.7	12.0
<b>100 &lt; 1000</b>	12.0	5.5	5.0	2.0	1.0	15.0
<b>&gt; 1000</b>	15.0	7.0	6.0	2.5	1.4	20.0

**Table 2.7.** Current distortion levels (69 kV – 161 kV) [10]

$I_{sc}/I_L$	$3 \leq h < 11$	$11 \leq h < 17$	$17 \leq h < 23$	$23 \leq h < 35$	$35 \leq h < 50$	TDD
<b>&lt; 20</b>	2.0	1.0	0.75	0.3	0.15	2.5
<b>20 &lt; 50</b>	3.5	1.75	1.25	0.5	0.25	4.0
<b>50 &lt; 100</b>	5.0	2.25	2.0	0.75	0.35	6.0
<b>100 &lt; 1000</b>	6.0	2.75	2.5	1.0	0.5	7.5
<b>&gt; 1000</b>	7.5	3.5	3.0	1.25	0.7	10.0

**Table 2.8.** Current distortion levels (> 161 kV) [10]

$I_{sc}/I_L$	$3 \leq h < 11$	$11 \leq h < 17$	$17 \leq h < 23$	$23 \leq h < 35$	$35 \leq h < 50$	TDD
<b>&lt; 20</b>	1.0	0.5	0.38	0.15	0.1	1.5
<b>20 &lt; 50</b>	2.0	1.0	0.75	0.3	0.15	2.5
<b>50 &lt; 100</b>	3.0	1.5	1.15	0.45	0.22	3.75

## 2.3. Rectifier and Inverter Configurations

### 2.3.1. Space Vectors

Inverter loads such as induction and synchronous machines, as a consequence of their highly-coupled nature, have led to the creation and adoption of artificial variables rather than using the actual system variables for the sake of simulation and visualization of data [9].

As **Figure 2.10** shows, the phase variables can be understood as components of a single vector existing in a three-dimensional orthogonal space which, when projected, give place to the instantaneous values of those same variables.

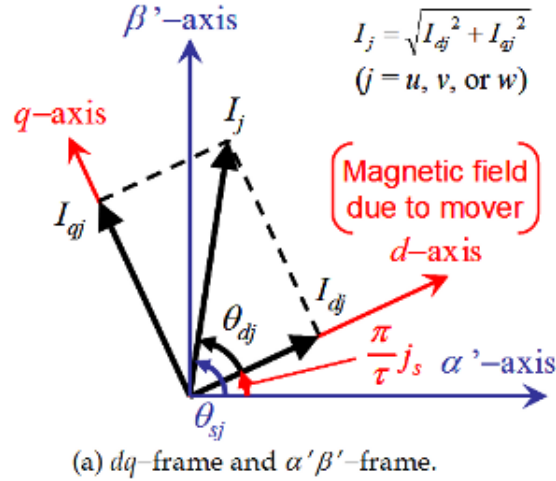


**Figure 2.10.** Space vector

Of course, in a balanced three-phase system the sum of those variables is commonly zero as three-phase loads usually lack a neutral return path, making the space limited to a plane referred as the  $d$ - $q$  plane. In it, the aforementioned vector is made up of two components, while an axis normal to it – the zero component – exists when the system is imbalanced [9]. Conventionally, the projection of the phase A variable on the plane forms the reference  $q$  axis when the axes are not rotating.

**Equation 2.10** shows the transformation of the three phase variables to the  $dq0$  space.

$$\begin{bmatrix} f_q^s \\ f_d^s \\ f_0 \end{bmatrix} = \sqrt{\frac{2}{3}} \begin{bmatrix} 1 & -\frac{1}{2} & -\frac{1}{2} \\ 0 & -\frac{\sqrt{3}}{2} & \frac{\sqrt{3}}{2} \\ \frac{1}{\sqrt{2}} & \frac{1}{\sqrt{2}} & \frac{1}{\sqrt{2}} \end{bmatrix} \begin{bmatrix} f_a \\ f_b \\ f_c \end{bmatrix} \quad (2.10)$$

In the case that the system is balanced, the previous equation is simplified:

$$\begin{bmatrix} f_q^s \\ f_d^s \\ f_0 \end{bmatrix} = \begin{bmatrix} \sqrt{\frac{3}{2}} & 0 & 0 \\ 0 & -\frac{1}{\sqrt{2}} & \frac{1}{\sqrt{2}} \\ 0 & 0 & 0 \end{bmatrix} \begin{bmatrix} f_a \\ f_b \\ f_c \end{bmatrix} \quad (2.11)$$

So, considering the equations defining a balanced three-phase voltage system:

$$\begin{aligned} v_a &= V \sin(\omega_0 t) \\ v_b &= V \sin\left(\omega_0 t - \frac{2\pi}{3}\right) \\ v_c &= V \sin\left(\omega_0 t + \frac{2\pi}{3}\right) \end{aligned} \quad (2.12)$$

When analyzing **Equation 2.11** with the group of equations shown in **Equation 2.12**, the transformations can be simplified even further:

$$\begin{aligned} v_{qs}^s &= \sqrt{\frac{3}{2}} V \sin \omega_0 t \\ v_{ds}^s &= -\sqrt{\frac{3}{2}} V \cos \omega_0 t \\ v_{0s}^s &= 0 \end{aligned} \quad (2.13)$$

It can be easily understood that the vector rotates with an angular velocity equal to the angular frequency of the source voltage [9]. The current and flux vector will also describe such trajectory, while having an offset angle to the voltage vector.

For the sake of a simplified control of induction motors, more akin to the control of a DC motor, a synchronous voltage reference frame is commonly applied in modern control applications where the defined axes are rotating with the stator voltage. Thus, the



transformations may be defined as shown in **Equation 2.14**, divided in two different matrixes for the sake of computational advantage:

$$f_{qdo} = R(\theta)T_{qdo}(0)f_{abc} \quad (2.14)$$

Where,

$$T_{qdo}(0) = \begin{bmatrix} \frac{2}{3} & -\frac{1}{3} & -\frac{1}{3} \\ 0 & -\frac{1}{\sqrt{3}} & \frac{1}{\sqrt{3}} \\ \frac{\sqrt{2}}{3} & \frac{\sqrt{2}}{3} & \frac{\sqrt{2}}{3} \end{bmatrix} \quad (2.15)$$

$$R(\theta) = \begin{bmatrix} \cos \theta & -\sin \theta & 0 \\ \sin \theta & \cos \theta & 0 \\ 0 & 0 & 1 \end{bmatrix} \quad (2.16)$$

### 2.3.2. Gate Logic Generation

Power electronic converters are a family of electrical circuits which convert electrical energy from one level of voltage to another using semiconductor-based electronic switches [9]. Changing the state of said switches in a process called *modulation* has spawned a number of different control strategies for the better part of 3 decades.

One of the most used strategies for controlling the output of power electronic converters is the *Pulse Width Modulation* technique (PWM), which varies the duty cycle of the switches at a high switching frequency to achieve a lower frequency output.

By principle, all modulation schemes aim to create trains of switched pulses with the same fundamental volt-second average as a target reference waveform at any instant [9]. The problem with said trains is the number of harmonics inherent to them. Which makes the main purposes of any modulation scheme the following:

1. Calculate the ON timing which creates the desired output
2. Determine the most effective way of producing the switching process to minimize harmonic distortion.

For the specific case of PWM, three different alternatives have been proposed for the sake of fixed-frequency modulation [9]:

1. Switching at the intersection of a target reference waveform and a high-frequency carrier, *naturally-sampled PWM*.
2. Switching at the intersection between a regularly sampled reference waveform and a high-frequency carrier, *regular-sampled PWM*.
3. Switching so the integrated area of the target reference waveform over the carrier interval is the same as the integrated area of the converted switched input, *direct PWM*.

As for naturally sampled methods, the most common form employed is the one using a triangular carrier in place of a sawtooth one to compare against the reference waveform, as shown in **Figure 2.11**. This type of carrier modulates both sides of the switched output from the phase leg, improving the harmonic content of the pulse train.

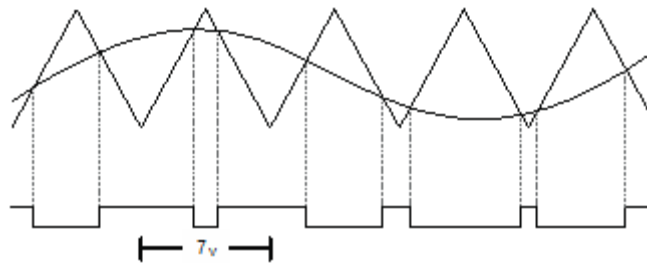


**Figure 2.11.** Sine-triangle modulation

But a disadvantage of this type of PWM implementation is the difficulty to employ it in a digital modulation system because of the complexity involved in the calculation of the transcendental equation defining the intersection between the reference waveform and the carrier [9]. The regular-sampled PWM method overcomes this limitation by sampling and holding the low-frequency reference during each carrier interval, which is then compared against the triangular carrier to control the switching of each phase leg (see **Figure 2.12**). The sampled reference must change value at the peak of the reference waveform, in order to avoid the change at the ramping period – a possible cause of multiple switch transitions [9].

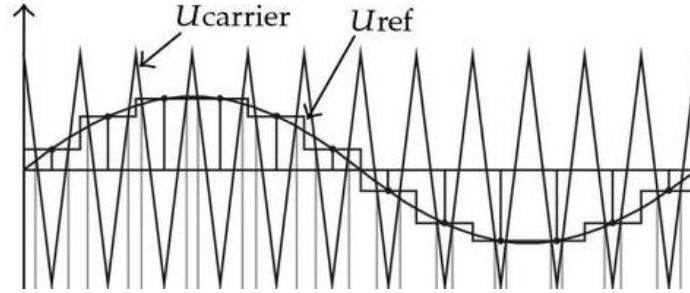


**Figure 2.12.** Regular-sampled PWM

As for the third method, the determining of the width of the switched pulses is done by switching the inverter to create an active pulse interval for each carrier interval that exactly achieves the same volt-second average of the original target [9]. As the explanation implies, this method requires an integration through the carrier interval, and is usually not practical to implement.

An additional alternative for a modulation control technique comes in the form of *Space Vector Modulation* (SVM), which yields a high voltage gain and less harmonic distortion compared to the earlier mentioned techniques [17].

For the specific case of SVM, the three-phase input currents and output voltages are represented as space vectors, with the algorithm being simultaneously applied to both transformed variables – with the transformation detailed in the previous section, while its magnitude is as shown in **Equation 2.17**.

$$V_0 = \frac{2}{3} [v_{ab} + v_{bc}e^{j120^\circ} + v_{ca}e^{-j120^\circ}] \quad (2.17)$$

The possible switching combinations determine the position of the resulting output voltage space vector (in the case of an inverter) while each combination creates six state space vectors that are used for the synthesis of the output [17], creating the six-sextant hexagon shown in **Figure 2.13**.

The modulation *per se* involves the selection of the vectors and their on-time computation: During each sampling period, the algorithm selects four active vectors in addition to a zero vector to construct a desired reference voltage – with the specific selection strategy affecting both the harmonic content of the output and switching losses. Then, the amplitude and phase

angle of the reference are calculated while the desired phase angle of the input current is determined in advance.

As for the ON periods of the chosen vectors, they are combined into two sets that lead into two new vectors adjacent to the reference vector in the sextant and having the same direction as the reference [17], while timings are calculated to obtain the component values shown in **Figure 2.13**.

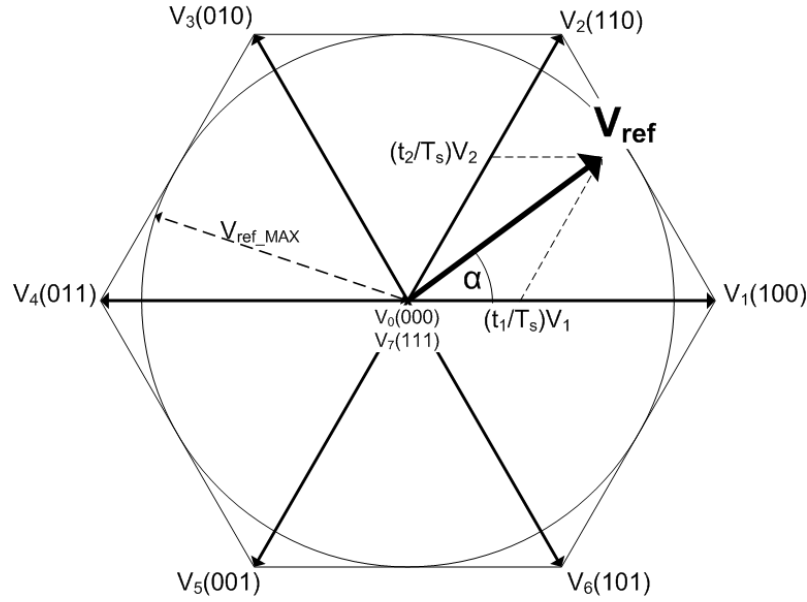


**Figure 2.13.** SVM sextant with all possible combinations, with an initial reference vector

### 2.3.3. Active Front End

The dispositive commonly referred as an Active Front End (AFE) in industrial settings can be understood as a power converter structure – which utilizes IGBT modules as switching devices – that usually works as an active rectifier, but may also work as an inverter when feeding power back to the grid [21].

Aside from its regenerative capabilities, when operating as a rectifier this topology basically works as a *boost* converter [17]. This permits the most desirable characteristics of an AFE device – a *boosted DC-link voltage* and *unity power factor* operation. A common structure found in commissioning is displayed in **Figure 2.14**.

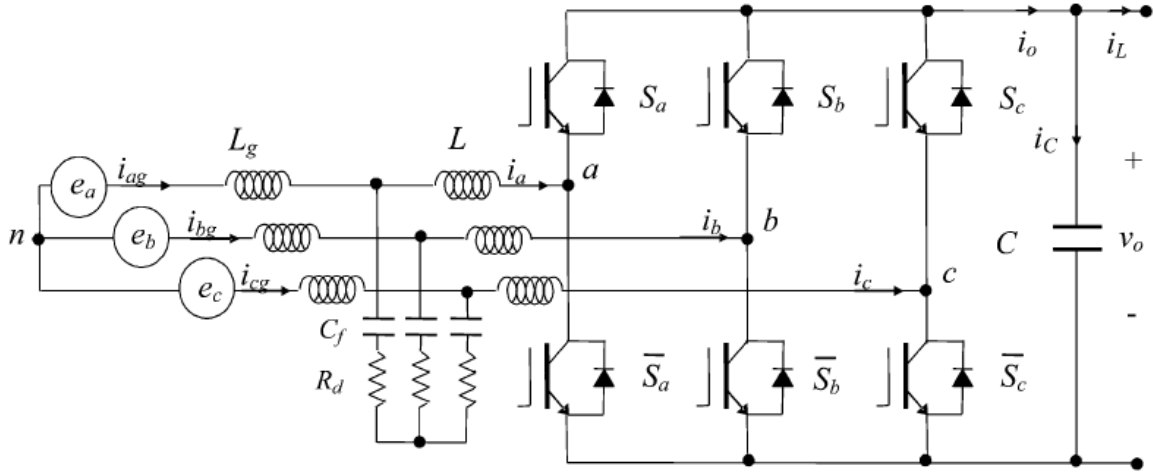


**Figure 2.14.** Three-phase active rectifier with leading LCL filter [14]

Initially proposed by Blaabjerg in [4], this kind of topology allows for an achievable sinusoidal input current with THD below 5% [13] [14], but its typical switching frequencies (ranging between 2 and 15 kHz) may cause disturbances that can negatively affect other equipment in the system [5]. To reduce these harmonic currents a high inductance was used in the initial proposal, but at higher power applications it becomes an expensive endeavor while the dynamic response suffers. Because of this, manufacturers tend to include a LCL filter as an alternative [25] [33].

Such filter should be properly designed in order for the circuit to correctly attenuate high-order harmonics while avoiding oscillation effects [14]. So, special attention must be taken with regards to the switching frequency and the resonance point of the circuit – the switching frequency must be high enough to benefit from damping, but also low enough to avoid a bulky and lossy topology [13].

As for the control of this kind of rectifier, space vector transformations are made to the voltage and current signals [24], which are then introduced into a control scheme similar to the one found in **Figure 2.15**.

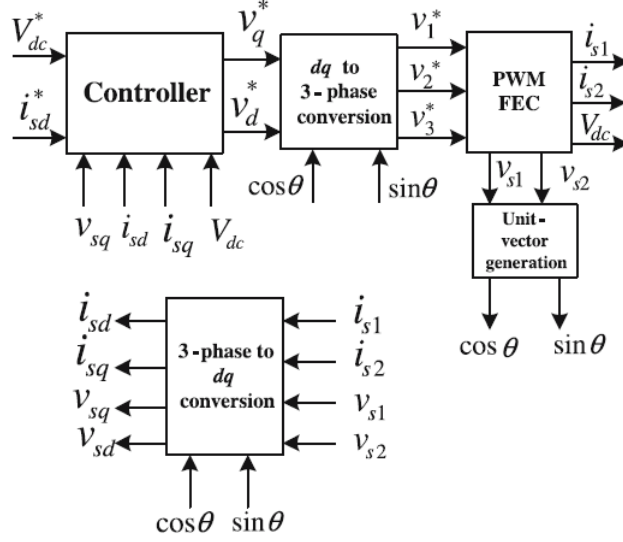


**Figure 2.15.** Basic control scheme in an AFE device [30]

But before fully delving into the control construct, the basic representation of an AFE should be heeded [21] – the one shown in **Figure 2.16**. In a rudimentary level, the circuit leading to an AFE may be represented by an AC power source, a series impedance, and a PWM voltage source representing the rectifier. In that case, the dynamic set of equations for the system takes the following form:

$$\begin{bmatrix} E_a \\ E_b \\ E_c \end{bmatrix} = L \frac{d}{dt} \begin{bmatrix} i_a \\ i_b \\ i_c \end{bmatrix} + R \begin{bmatrix} i_a \\ i_b \\ i_c \end{bmatrix} + \begin{bmatrix} V_a \\ V_b \\ V_c \end{bmatrix} \quad (2.18)$$

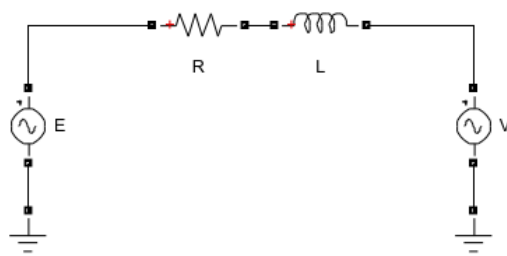


**Figure 2.16.** Basic circuit representation of AFE system, seen from rectifier side

Transforming the previous system of equations into a stationary reference frame:

$$\begin{bmatrix} E_{qs} \\ E_{ds} \end{bmatrix} = L \frac{d}{dt} \begin{bmatrix} i_{qs} \\ i_{ds} \end{bmatrix} + R \begin{bmatrix} i_{qs} \\ i_{ds} \end{bmatrix} + \begin{bmatrix} V_{qs} \\ V_{ds} \end{bmatrix} \quad (2.19)$$

Then, taking into consideration the dynamic transformation matrix in **Equation 2.16**, the system may be transitioned into a reference system rotating at the same angular speed as the electric frequency (With  $R(\theta)$  becoming  $A$  for clarity sake):

$$\begin{aligned}
 A \begin{bmatrix} E_{qs} \\ E_{ds} \end{bmatrix} &= LA \frac{d}{dt} \left( C^{-1} \begin{bmatrix} i_{qe} \\ i_{de} \end{bmatrix} \right) + RA \begin{bmatrix} i_{qs} \\ i_{ds} \end{bmatrix} + A \begin{bmatrix} V_{qs} \\ V_{ds} \end{bmatrix} \\
 \begin{bmatrix} E_{qe} \\ E_{de} \end{bmatrix} &= LA \left\{ \frac{d}{dt} (A^{-1}) \right\} \begin{bmatrix} i_{qe} \\ i_{de} \end{bmatrix} + LAA^{-1} \frac{d}{dt} \left\{ \begin{bmatrix} i_{qs} \\ i_{ds} \end{bmatrix} \right\} + R \begin{bmatrix} i_{qe} \\ i_{de} \end{bmatrix} + \begin{bmatrix} V_{qe} \\ V_{de} \end{bmatrix} \\
 \begin{bmatrix} E_{qe} \\ E_{de} \end{bmatrix} &= L \begin{bmatrix} \cos \theta & -\sin \theta \\ \sin \theta & \cos \theta \end{bmatrix} \left\{ \frac{d}{dt} \begin{bmatrix} \cos \theta & \sin \theta \\ -\sin \theta & \cos \theta \end{bmatrix} \right\} \begin{bmatrix} i_{qe} \\ i_{de} \end{bmatrix} + L \frac{d}{dt} \left\{ \begin{bmatrix} i_{qs} \\ i_{ds} \end{bmatrix} \right\} + R \begin{bmatrix} i_{qe} \\ i_{de} \end{bmatrix} + \begin{bmatrix} V_{qe} \\ V_{de} \end{bmatrix} \\
 \begin{bmatrix} E_{qe} \\ E_{de} \end{bmatrix} &= L \begin{bmatrix} \cos \theta & -\sin \theta \\ \sin \theta & \cos \theta \end{bmatrix} \begin{bmatrix} -\omega \sin \theta & \omega \cos \theta \\ \omega \cos \theta & -\omega \sin \theta \end{bmatrix} \begin{bmatrix} i_{qe} \\ i_{de} \end{bmatrix} + L \frac{d}{dt} \begin{bmatrix} i_{qe} \\ i_{de} \end{bmatrix} + R \begin{bmatrix} i_{qe} \\ i_{de} \end{bmatrix} + \begin{bmatrix} V_{qe} \\ V_{de} \end{bmatrix} \\
 \begin{bmatrix} E_{qe} \\ E_{de} \end{bmatrix} &= \omega L \begin{bmatrix} 0 & 1 \\ -1 & 0 \end{bmatrix} \begin{bmatrix} i_{qe} \\ i_{de} \end{bmatrix} + L \frac{d}{dt} \begin{bmatrix} i_{qe} \\ i_{de} \end{bmatrix} + R \begin{bmatrix} i_{qe} \\ i_{de} \end{bmatrix} + \begin{bmatrix} V_{qe} \\ V_{de} \end{bmatrix} \tag{2.20}
 \end{aligned}$$

Where **Equation 2.20** represents the dynamic model of the system in the  $d$ - $q$  plane.

Returning to the control discussion, as the AFE intends to work while controlling the power factor, the natural conclusion is that the main control variables will be the current components  $i_{qe}$  and  $i_{de}$  [21] [30]. The  $q$ -axis component represents reactive current, and is considered a compensation factor to keep the PF in the desired state; the  $d$ -axis component represents the real portion of the current, needed to keep a constant voltage across the DC capacitance and to drive the loads [21].

For the sake of having an optimal control over the system, the current components must be uncoupled from each other, making a feedback loop needed. And for that to occur, both active and reactive current references must be generated; the reactive reference is commonly specified by the user, while the active reference comes from a DC-link controller, as **Figure 2.17** illustrates.

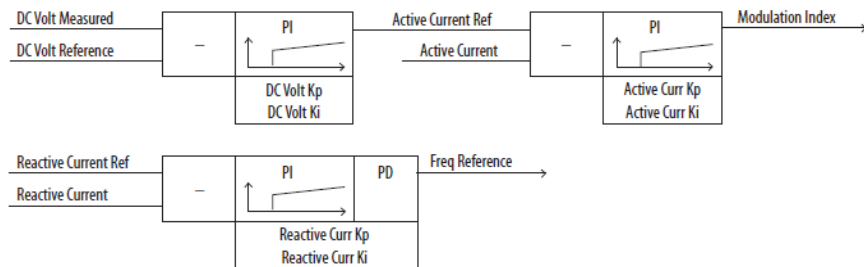


**Figure 2.17.** Main PI controllers involved in AFE operation [25]

The parameters obtained through the output of the current controller indicate the voltage references that go to the PWM-generation controller, producing the switching logic by any of the previously mentioned methods.

*Frequency synchronization.* An important detail that is common in this kind of control strategies is the need of synchronization with the actual working frequency of the power source – as  $dq$ -plane transformations are involved in the generation of the control signals, a slight offset may potentially cause undesirable behavior and flawed feedback, ultimately impacting performance. This kind of control loop is called a *phase-locked loop* (PLL), and is implemented with the reactive current signal, just as **Figure 2.17** shows.

*Linearization.* Another point to consider is the fact that the unbundling of the dynamic equations made by the feedback control loop no longer applies when there are large variations of DC voltage. A large acceleration or deceleration in the loads is a common cause of this kind of behavior [21].

To solve this, new variables referenced to the dynamic description of the system are introduced:

$$\begin{aligned} V'_{qe} &= V_{qe} - E_{qe} + \omega L i_{de} + i_{qe} R \\ V'_{de} &= V_{de} - E_{de} - \omega L i_{qe} + i_{de} R \end{aligned} \quad (2.21)$$

Substituting them in the dynamic model equations for the rectifier,

$$\begin{aligned} L \frac{di_{qe}}{dt} &= -V'_{qe} \\ L \frac{di_{de}}{dt} &= -V'_{de} \end{aligned} \quad (2.22)$$

But even if the current dynamics are now uncoupled, the voltage commands for the PWM controller must consider this change:

$$\begin{aligned} V_{qe}^* &= V'_{qe} + E_{qe} - \omega L i_{de} - i_{qe} R \\ V_{de}^* &= V'_{de} + E_{de} + \omega L i_{qe} - i_{de} R \end{aligned} \quad (2.23)$$



The current control loop including input linearization is shown in a graphic manner in **Figure 2.18**.

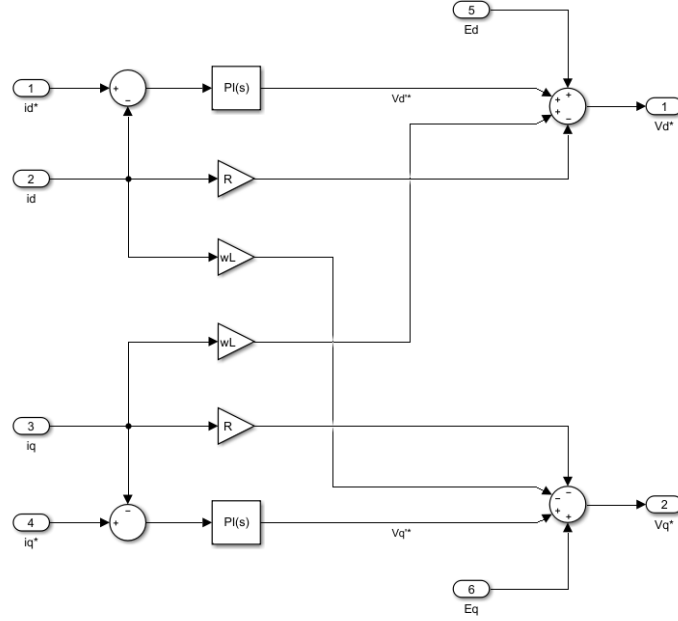


**Figure 2.18.** Current loop with I/O linearization

The control that characterizes an Active Front End not only gives them the previously mentioned abilities of working under UPF while boosting the DC voltage, but it also makes them resistant to common Power Quality events.

In **Figure 2.19** it can be observed the behavior of a common AFE topology in presence of a voltage notch. From the picture, it can be detected that the DC voltage level falls slightly at the same time the current in the faulted phase increases significantly. However, nominal levels of voltage and current recover in less than a cycle [6] [20].

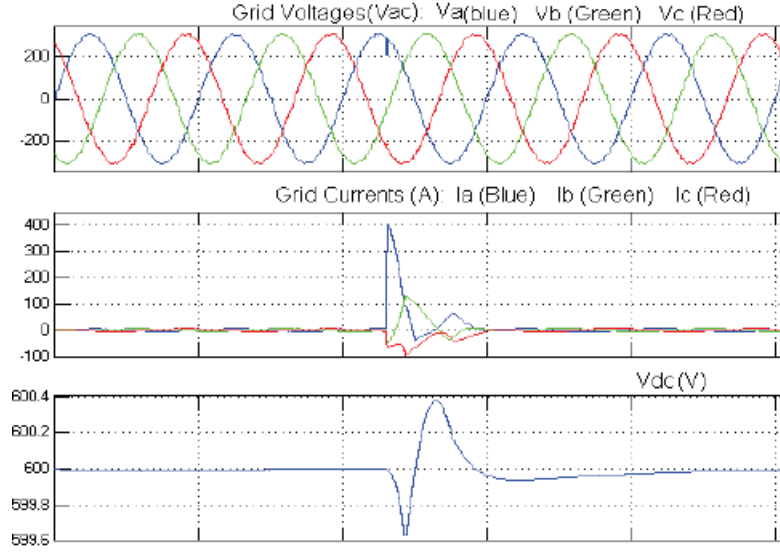


**Figure 2.19.** AFE behavior in presence of a voltage notch

Nevertheless, even this kind of device has its own share of problems. As noted in [19], while operating as an active rectifier the phase to ground voltage distortion increases significantly (see **Figure 2.20**), creating problems with Electromagnetic Compatibility for other loads in the same system in which such characteristics may be critical, such as medical equipment or uninterruptible power supply (UPS) devices [3].

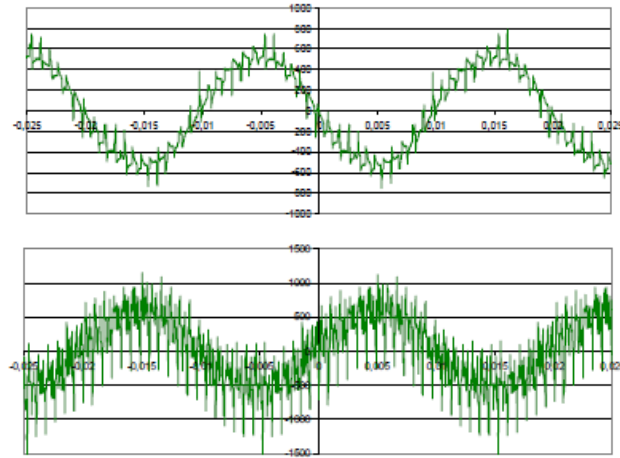


**Figure 2.20.** Phase-to-Ground voltage with a 6-pulse rectifier and an AFE

Another detail that jumps is the fact that the circulation of line current through the input reactor also generates a large current through neutral to ground, which is filled by high-order frequency content when the AFE is working as an active rectifier. Several topologies have

been proposed to deal with this fact, usually grounding capacitance in the DC side of the AFE [3] [12].

One more situation that may arise when both uncontrolled rectifiers and AFE share a power supply is the possibility that the common ground current generated by the active system may return through the capacitors in the inverter side of a diode-based rectifier system. This *pump-up* effect may rise the DC voltage level in the last circuit over design parameters and directly impact the lifetime of the elements connected to it, as seen in **Figure 2.21** [8].

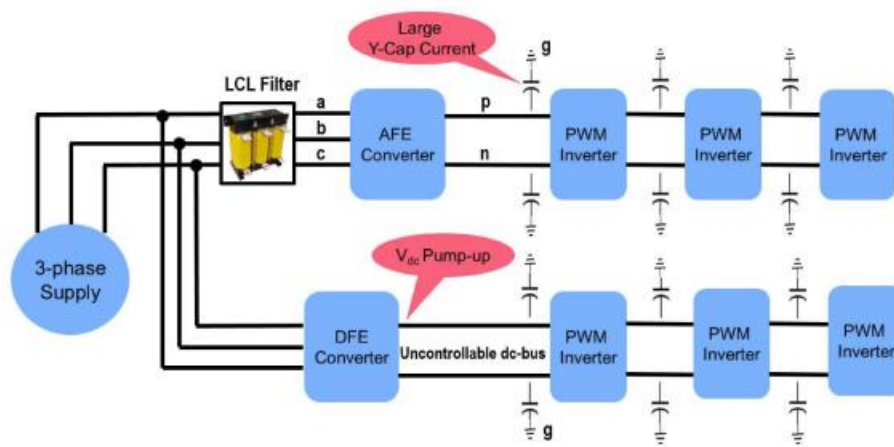


**Figure 2.21.** DC overvoltage produced by common-mode current [8]

#### 2.3.4. Field-Oriented Control Drives

Squirrel-cage induction motors (and AC machines in general) historically lacked a control scheme as simple as the one used with a DC machine; doing so would need a decoupling of magnetic flux and produced torque to maintain linearity between inputs and outputs [2]. This problem was overcome with the advent of space vector representations of those machines' variables, with flux-oriented control strategies allowing their representation in a similar way to the decoupled DC machines.

In a DC motor, torque production depends on armature current and machine flux [2], and to produce maximum torque the magnetic field should be maintained at an optimal value (rated flux) while avoiding saturation in the magnetic circuit. That way, the constant flux will

allow for a linear relationship torque and current. In contrast, when using scalar control in squirrel-cage motors only the stator current is available with no direct way to manipulate the rotor current, making linear control while maintaining maximum torque a difficult proposition to achieve.

Field-oriented control makes possible to introduce the same kind of decoupled control by using vector representation, so the relationships between motor variables may be described in a  $dq$ -plane rotating with motor flux on the  $d$  axis. The basic control scheme used in FOC devices is shown in **Figure 2.22**.

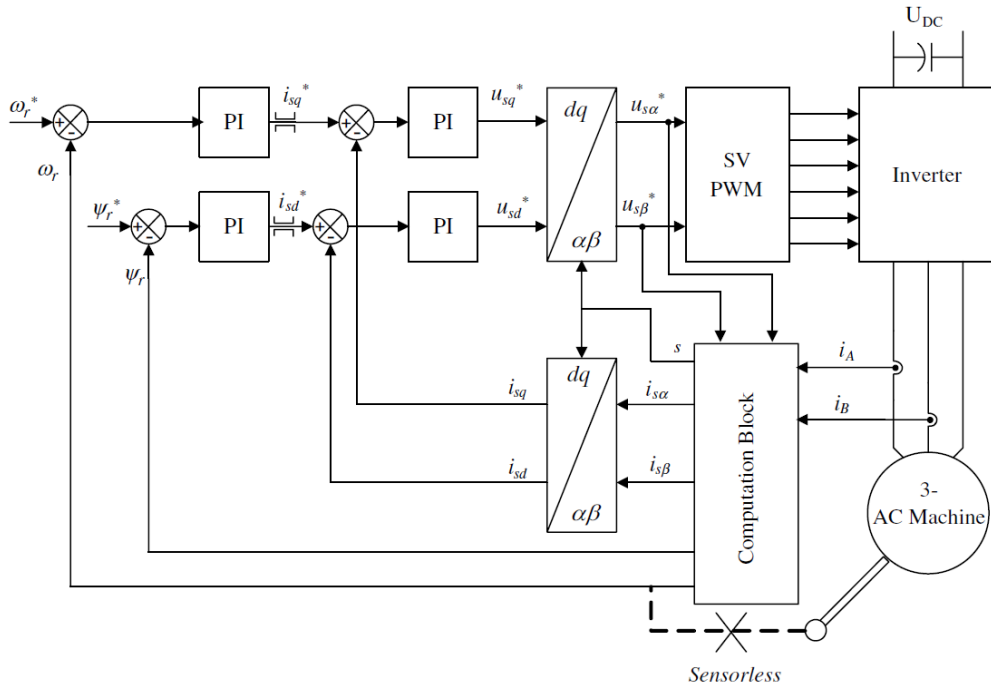


**Figure 2.22.** FOC scheme for a three-phase machine

It can be observed that two motor phase currents and the DC-link voltage are measured. The currents are transformed to the stationary reference axes and then to synchronous system, ultimately obtaining rotating components ( $dq$ ). Those vectors are then compared to reference values obtained through flux and speed controllers, which pass through a controller to become voltage commands.

Similar to the gate logic generation in AFEs, the voltage commands are transformed to an appropriate reference system to be used in a Space Vector Modulation schema.

### III. Methodology

This part of the document deals with the entire chronology of actions taken during the duration of the project concerning the Electrolytic Cleaning line at the Pesquería Industrial Complex property of Ternium México. From the initial actions done in field to the final form of the model, all activities are thoroughly explained through the next sections of this chapter. **Figure 3.1** explains the key activities in a graphic manner as a quick overview.

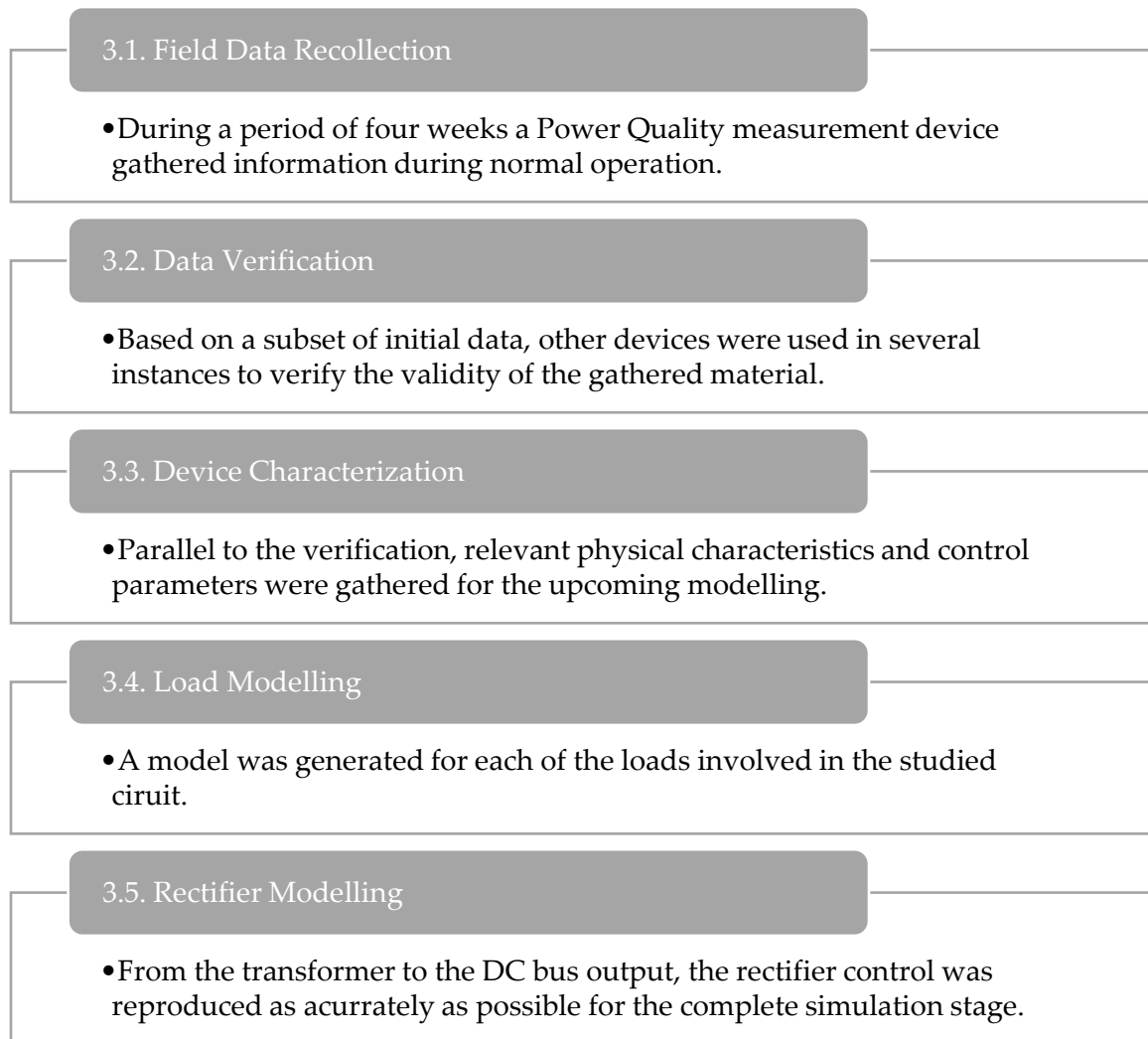


**Figure 3.1.** Main activities of the project

As mentioned earlier, the final model was made from the ground-up in the Simulink environment, part of the MATLAB package. The computational resources available during the entire period were composed of two different machines, working under Windows 10:

- A HP Z800 Workstation, with two parallel Intel Xeon processors working each at 2.60 GHz and a NVIDIA Quadro FX 3800 graphics card with 1 GB of dedicated VRAM. System RAM availability grew from an initial 12 GB to 16 GB, all with underlying DDR3 technology, while working with a 500 GB hard drive.
- A Dell Inspiron 7559 laptop, with an Intel Core i5-6300HQ processor working at 2.30 GHz and a NVIDIA GeForce GTX 690M GPU with 4 GB of GDDR5 VRAM. This computer had 8 GB of DDR3 RAM and a 1 TB hard drive.

The model was done in the Academic version of the R2015b release of MATLAB. Several considerations and concessions were done in the model that differ from the reality, and they will be acknowledged in their corresponding sections.

### 3.1. Field Data Recollection

As an initial approach, an understanding of the processes that happen in the Pesquería complex was needed, in order to clarify the roles that the different machines have in the area.

Pesquería Plant encompasses a group of processes that fall under the umbrella of *Cold Rolling*, which deals with the products of *Hot Rolling* to give them another set of physical and mechanical characteristics that buyers look in the steel they use for their own products. Inside the structure of Ternium this category involves 6 different processes, as shown in **Figure 3.2**.

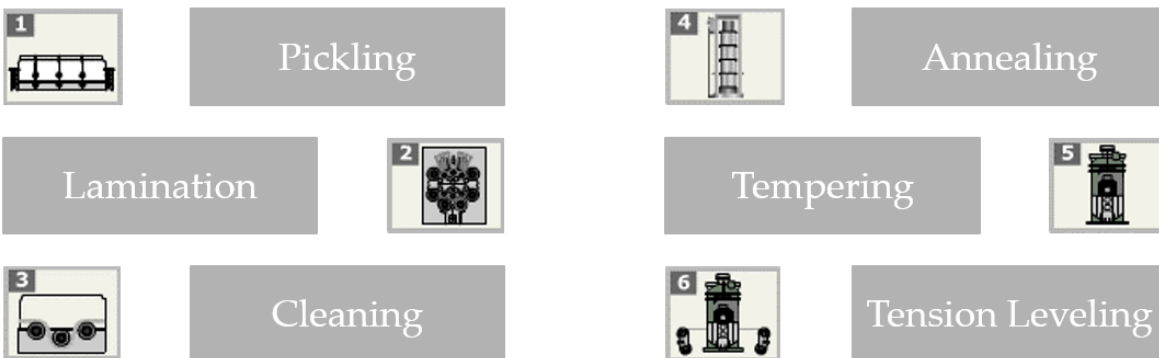


**Figure 3.2.** Cold Rolling processes present in Pesquería Plant

The specific line under study is the Electrolytic Cleaning line, coming after the Pickling and Lamination steps in the value chain. Its main purpose is to clean a steel roll of any impurities that it carried through the Pickling process and/or acquired during the Lamination using an industrial cleaning agent. A generic structure of this type of industrial process is presented in **Figure 3.3**.

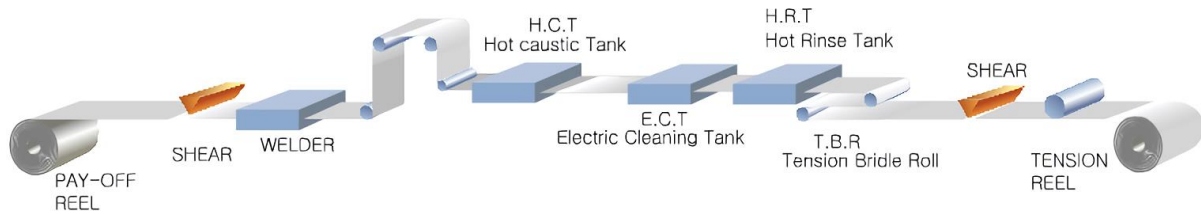


**Figure 3.3.** Electrolytic Cleaning Line in Steelmaking

As for the elements of interest for the current study, they are limited to 3 kinds of loads:

- *Pay Off Reel*, which initially carries the roll after being retrieved from the stock depot.
- *Bridle Roll 1 and 2*, each with two independent tension units.
- *Tension Reel*, which applies the force that makes the product to pass through the line.

These loads are connected to the same electrical circuit, which contains the motors making operation possible. An additional circuit feeds some additional loads, mainly ventilation and auxiliary motors.

As for the electric system, the main distribution of Pesquería Plant comes from a 400 kV High Voltage Line, whose voltage passes through a 400 kV/13.8 kV substation feeding a bus that contains every load in the industrial complex. A section of the general one-line diagram (OLD) illustrating this is shown in **Figure 3.4**.

Going further downstream in the one-line diagram reveals that the Electrolytic Cleaning, Annealing, Tempering, and Tenso Leveling lines share the same 13.8 kV bus, the same one that feeds the transformer directly responsible of the loads studied in this document, as **Figure 3.5** reveals.





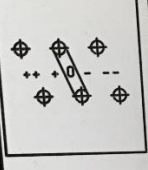
IEEE C57.12.01 **MF** *Trasformatori srl* Calcinato, Brescia Italy, Tel. 030/9636596

THREE-PHASE CAST RESIN TRANSFORMER

1250 kVA N° 081112/1 Year 2013 Phase N° 03

60 Hz Vcc 5.8 % Group Dy11 Overtemp. 85 K Cooling AN

Tap changer like following sketch



Position

Position	High voltage	Low voltage
+++		
++	14490	690
+	14145	1045.9
0	13800	
-	13455	
--	13110	
---		
	52.3	

Thermal insulation class F

Insulation level High voltage 15 / 34 / 95 kV Low voltage 1.2 / 4 / 20 kV

Weights Transformer 3850 kg Enclosure 380 kg Total weight 4230 kg IP Protection IP21

Environmental class: F2 Climatic class: C2 Fire class: F1

**Figure 3.6.** Operating values of the transformer

After it, a long set of cables feed power to the drive room, where a single group of cabinets protects the control systems – the AFE and the related drives. The installed Active Front End is a 1200 kW Allen Bradley PowerFlex 700AFE unit, which has as its output a DC bus common to six Allen Bradley PowerFlex 700S Drives, each with a Field-Oriented Control basis. Each drive output goes through a long group of conductors to arrive to their loads.

It must be mentioned that, heeding Rockwell instructions, a series LCL Filter is leading the three distinct Active Front End power modules while a pre-charge circuit is connected in parallel to limit the DC current. A manufacturer-made schematic can be seen in **Figure 3.7**, while a one-line diagram for both the rectification circuit and the loads are found in **Figure 3.8** and **3.9**.

In addition to the electric layout, the project team became aware of some initial recommendations done by the manufacturer acknowledging deficiencies inherent to the operative design. Those comprised the following points, some already implemented:

1. DC capacitance inherent to the loads is insufficient to diminish the ripple in DC voltage. According to their calculations, around 40,000  $\mu\text{F}$  are needed. Recently a bank of a slightly smaller capacitance was approved by Ternium, although its installation is still pending.

2. The DC snubber module was deemed as faulty, and needed to be replaced. This was done around the end of October 2016, and no related problems have appeared since then.
3. According to a drive installation manual of Rockwell, a Common Mode Core (CMC) is needed both at the DC output of the Active Front End and at each of the loads. Also, the CMC corresponding to the Tension Reel needed to be replaced.
4. Damping resistors should be added to the  $dv/dt$  filters at each motor.

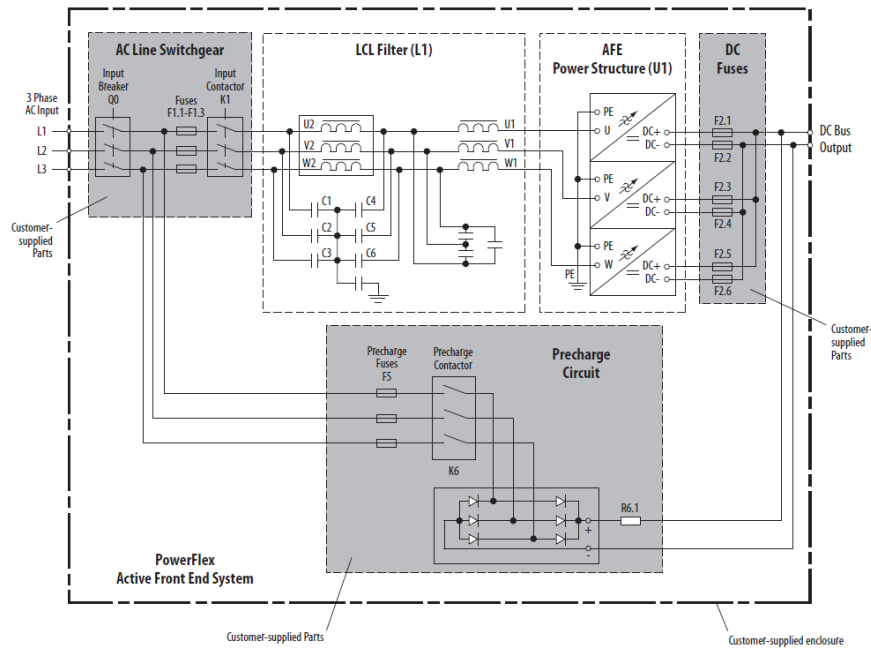


**Figure 3.7.** AFE Power Circuit [25]

With all information at hand, it was decided that two Power Quality devices – a pair of ELSPEC BLACKBOX – were to be installed for a lapse of time in both AC and DC sides, measuring voltage and current during normal operation of the system. The AC measurements were done in the 690 V side of the transformer, while the DC voltage measurement was done directly in the common DC bus.

Although they were installed through the entirety of November 2016, an initial subset of data was extracted for an initial analysis. Those preliminary results had a surprising pattern.

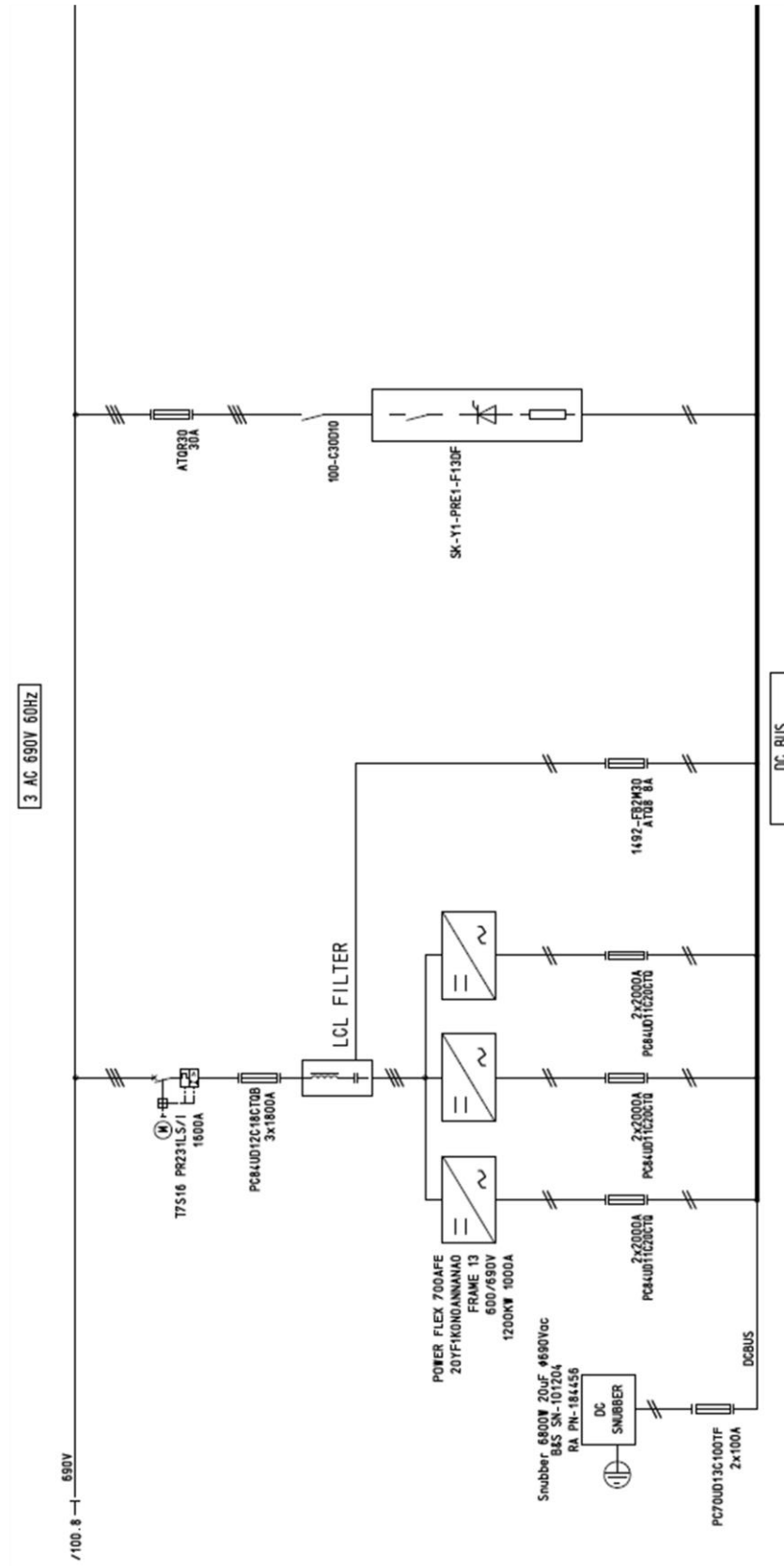
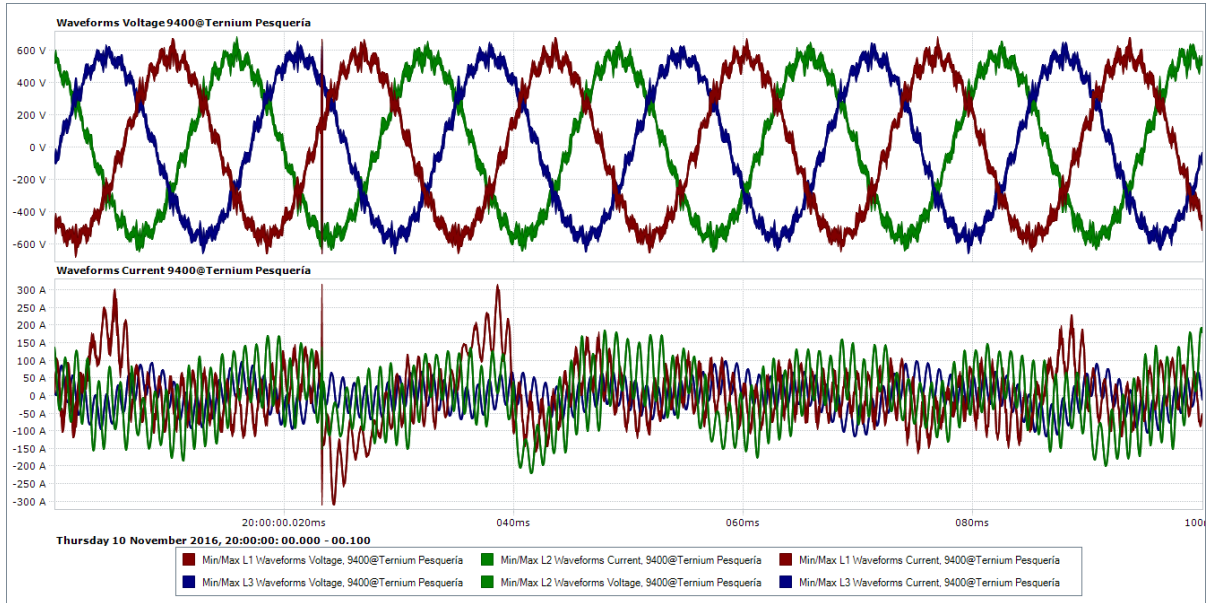


Figure 3.8. One-line diagram, AC side



As **Figure 3.10** clearly indicates, at a randomly selected 100 ms sample of that subset a highly distorted current waveform was found, while a slight distortion was found in the voltage waves. **Figure 3.11** presents the DC voltage in larger period (1 minute) to illustrate the ripple present, just as it was expected.



**Figure 3.10.** Voltage and current waveforms, 100 ms sample

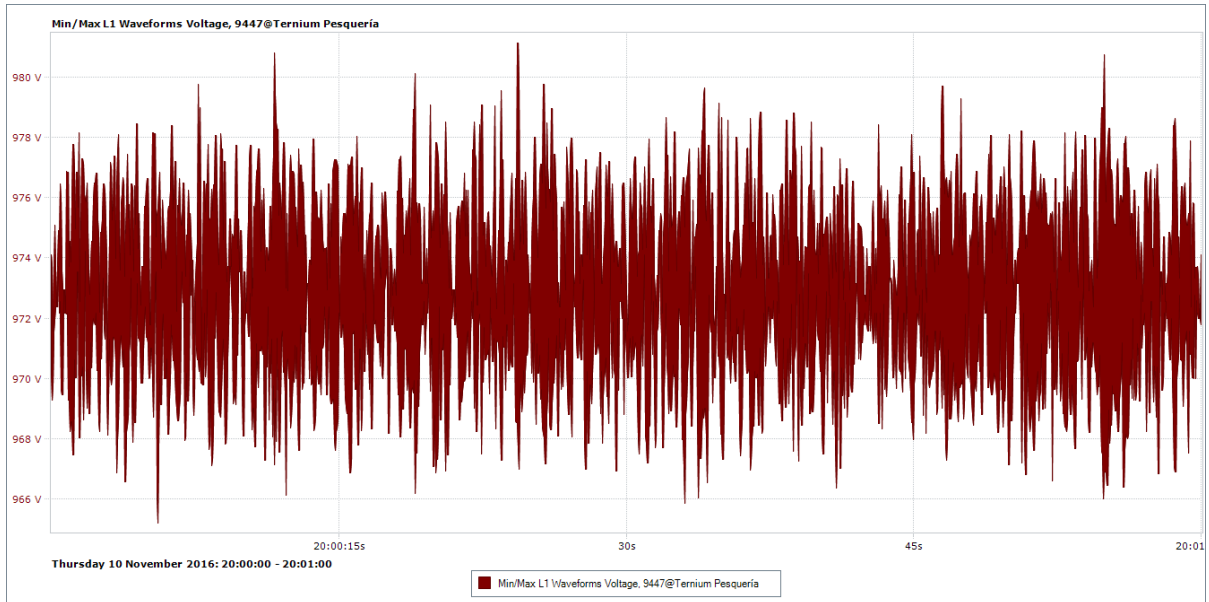


**Figure 3.11.** DC bus voltage during a minute sample

The pattern of a highly-distorted current with a noticeable voltage distortion was repeated during the whole initial data, and it eventually was found in the whole database when both ELSPEC devices were taken offline and their data was recovered.

The fact that there was a high quantity of harmonic content in the transformer 690 V side was worrisome, as the Active Front End control is supposed to regulate the amount of reactive current to zero or a close value. The frequency spectrum of both voltage and current signals threw an interesting picture, with the 17<sup>th</sup> harmonic (1.02 kHz) becoming quite important, as it was the main distortion source in the voltage for all phases (aside from high frequency noise, measured around the tens of kilohertz) and one of the highest current distortion sources aside from the second harmonic. Both are shown in **Figure 3.12**.

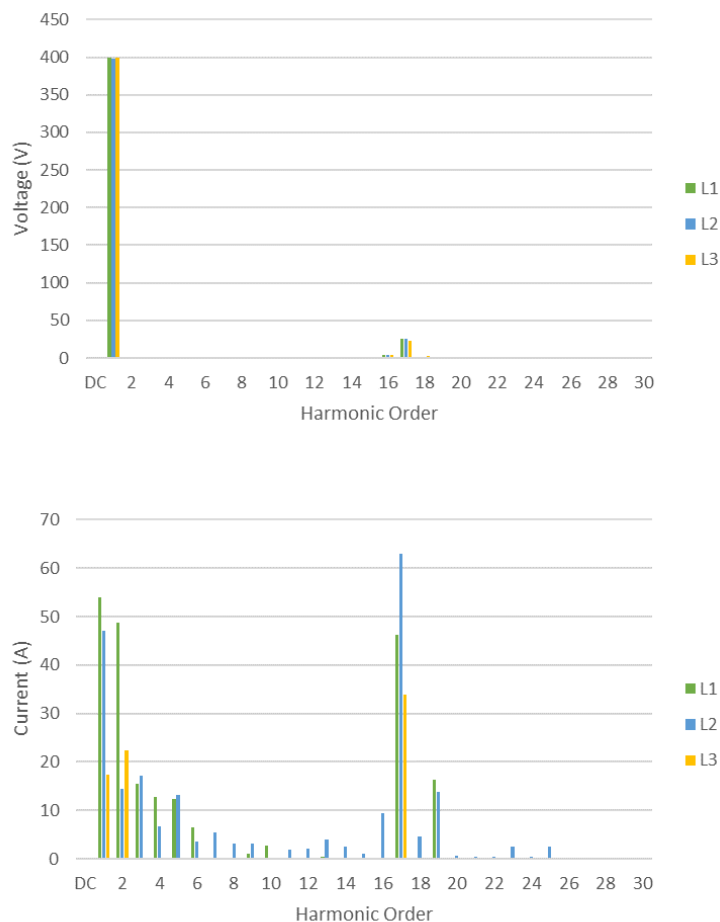


**Figure 3.12.** Voltage and current spectrum, 100 ms sample

### 3.2. Data Verification

As was mentioned in the last section, the initial data results from the AC side were astonishing, as the power factor suffered because of the high amount of harmonic content – especially in the current. Because of this, several actions were taken to verify the validity of the results.

For a first step, a re-inspection of how the devices were connected to the transformer was done in a later visit to the plant. A pair of photographs illustrating these connections is presented in **Figure 3.13**. The connection to ground was also verified, as it would imply a change in the parameters of the ELSPEC measurements and scraping the data. It was ultimately deemed unnecessary as the connections were considered correct.

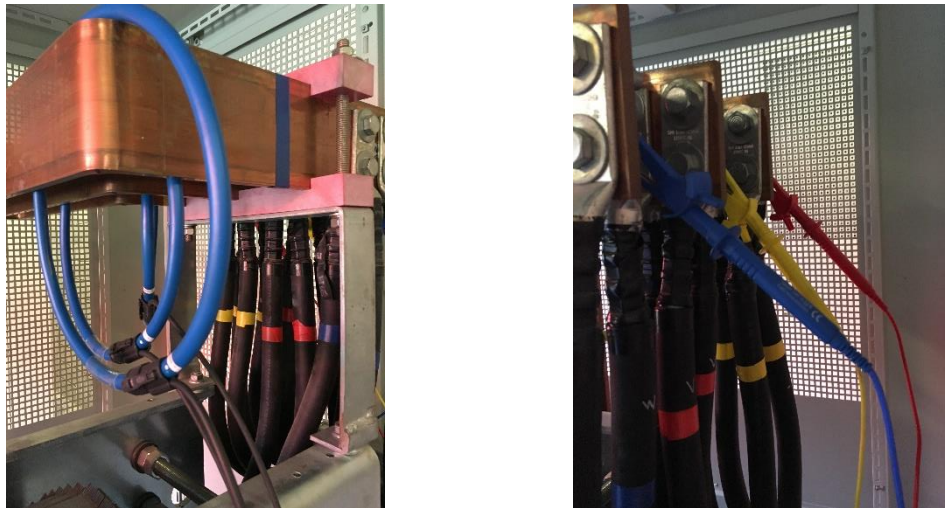


**Figure 3.13.** Current and voltage probes during measurements

As the physical connections and the probes' condition seemed in order, a second measurement device was used to corroborate the compiled data to discard the possibility of internal damage or misconfiguration, a FLUKE 43-B.

As the FLUKE is a portable device it was possible to check data during operation, but for internal safety protocols the use of the voltage probes was not authorized for the risk of electrocution. Any portable data was to be based on current values.

**Figure 3.14** shows the comparison between ELSPEC and 43-B data, with samples around the same time for Phase A. Additional data for Phase B and C can be found in Annex I.

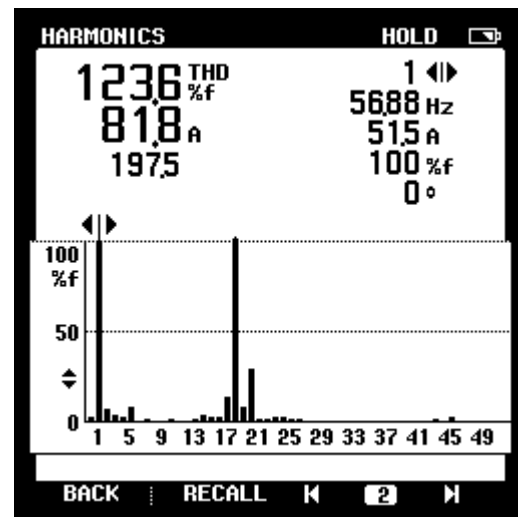
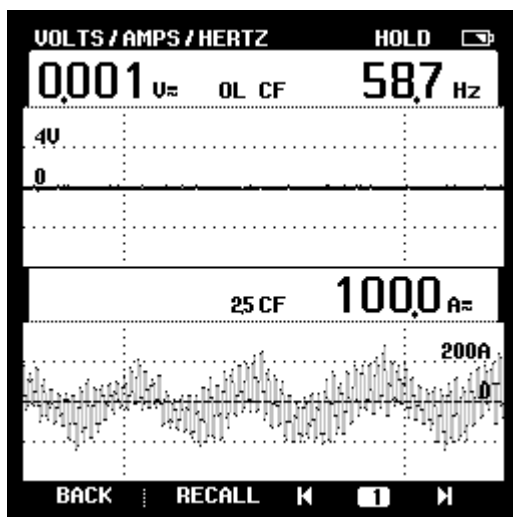
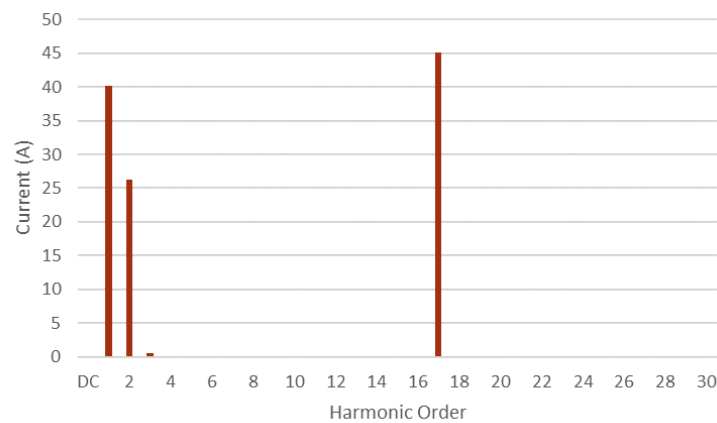
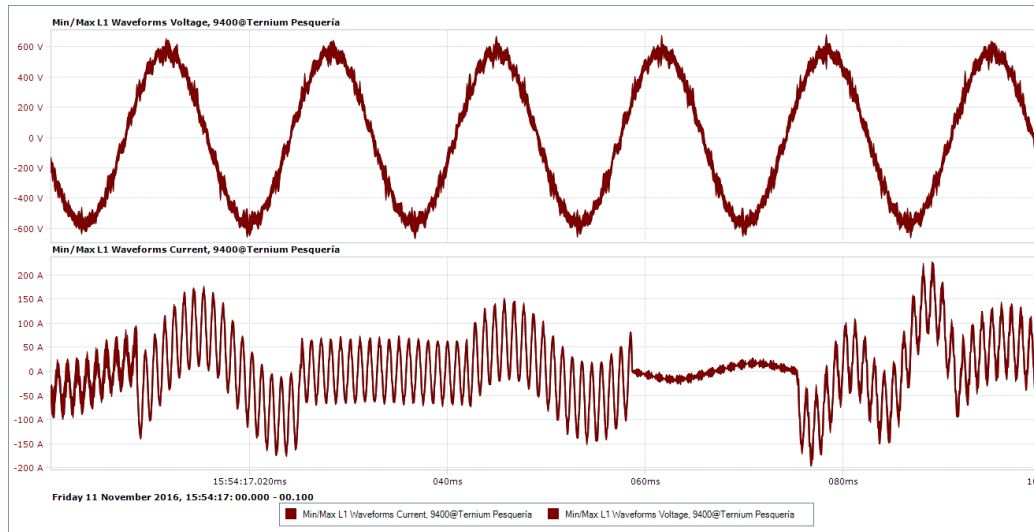


Figure 3.14. Data comparison between PQ sources



The results in all phases were consistent between the two devices, so the validity of the gathered data was accepted. In consequence, questions about the conditions that are prevalent in the productive line were raised; the focus shifted to the possibility that the results came from a systemic deficiency that may appear in other lines.

Working under this assumption, and after the ELSPEC devices were taken off from the power conductors, a comparison between two similar subsystems was done. One was the main load circuit that is the object of study, while the other one was a smaller AFE circuit. This additional system works with a voltage of 480 V, and deals with the accessory loads that also participate in the Electrolytic Cleaning line. A comparison between waveforms from all phases at the input side of both AFE devices is shown in **Figure 3.16**.

Their power supply comes from the same 13.8 kV bus (as seen in the general distribution one-line diagram in **Figure 3.5**), but each circuit relies on their own step-down transformer because of the difference between operating voltages. Nevertheless, from the samples in **Figure 3.16** it can be surmised that a similar harmonic distortion is happening in both EC power circuits, with the difference that the 480 V signals show more symmetry between cycles compared to the main loads' circuit.

Furthermore, as **Figure 3.15** shows, the harmonic content between both devices input currents differs slightly, with the 690 V line showing the previously mentioned 17<sup>th</sup> harmonic. Meanwhile, 19<sup>th</sup> harmonic content was more prevalent in the smaller capacity AFE.

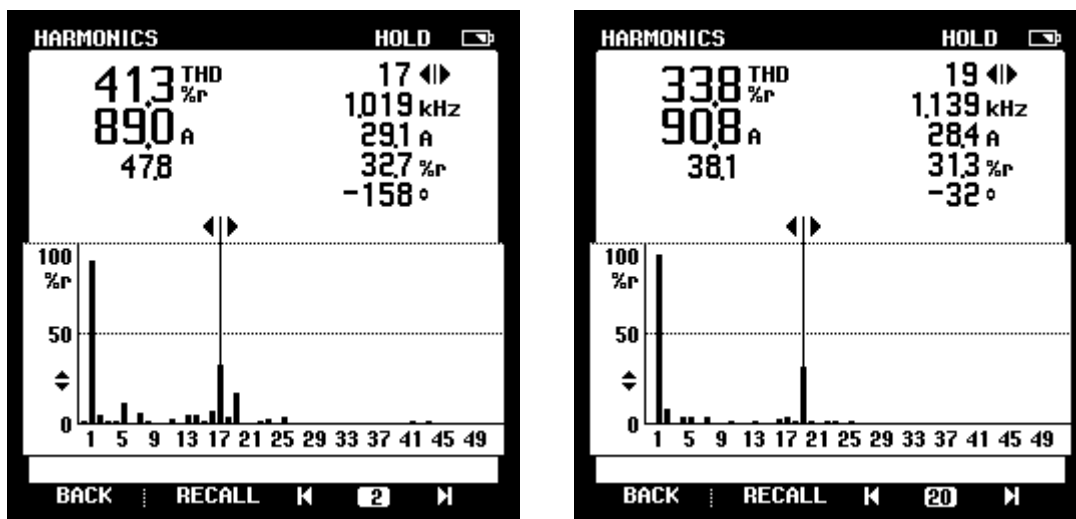


**Figure 3.15.** Harmonic content in both ECL AFE input currents

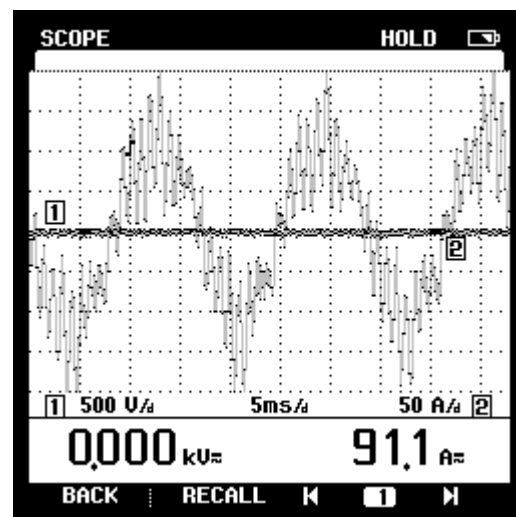
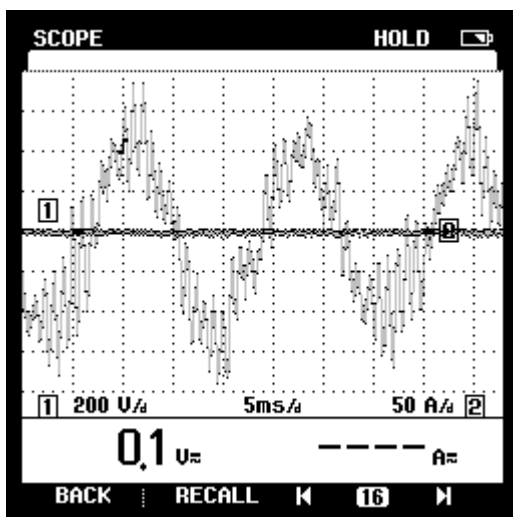
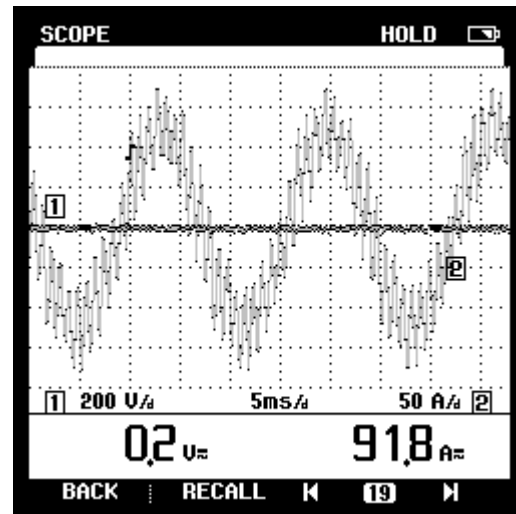
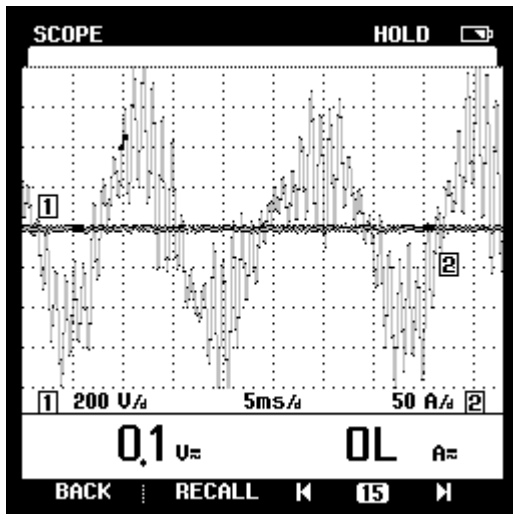
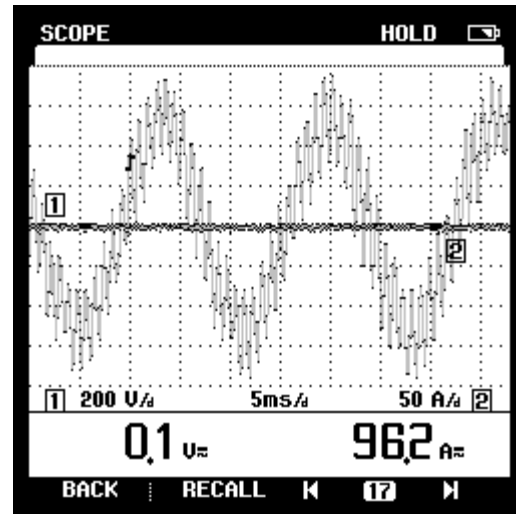
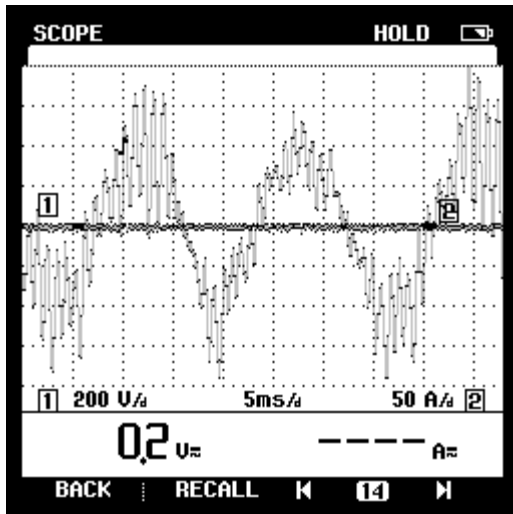
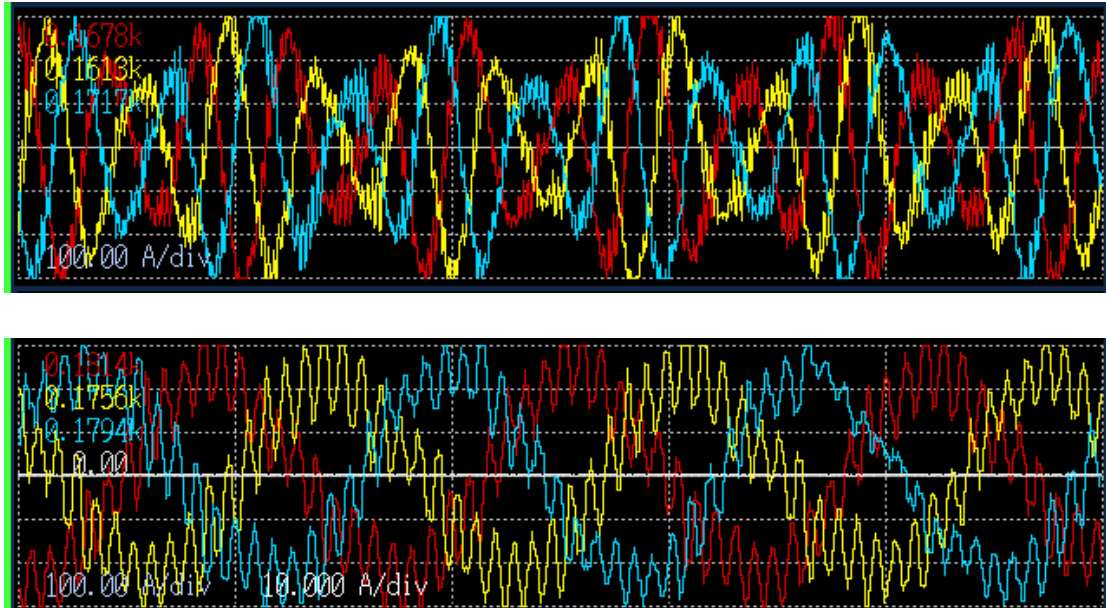
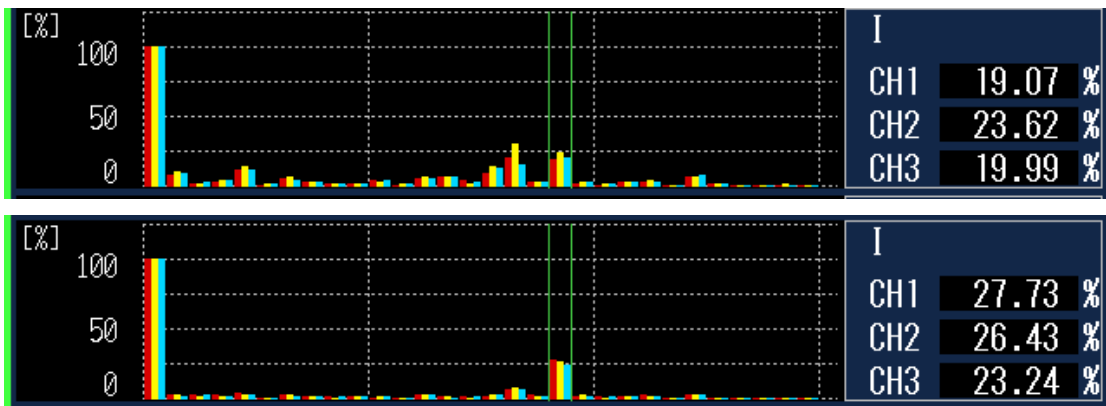


Figure 3.16. Comparison between both systems' Phases A, B, and C, respectively

A further comparison was made between the same devices with a different measuring device – this time with a HIOKI PQ3100. The results were similar to what was observed with both the 43-B and the ELSPEC devices, as **Figure 3.17** and **3.18** make clear.



**Figure 3.17.** Waveform from the main and auxiliary loads, respectively



**Figure 3.18.** Spectrum from both circuits, with cursor over the 19<sup>th</sup> harmonic

One detail that happened during the sampling time and must be noted is that the power factor presented a variant value during observed operation. During the time that no roll was going through the system or a change in speed was being done its value was lower than when a product was going through the process at full speed. This can be appreciated in **Figure 3.19**.



**Figure 3.19.** HMI and dedicated device showing PF (a - No load b - Full speed)

Another development to notice is that the distortion was also present in the 13.8 kV bus, not only in the currents but also in the voltage – oscillating around 30% and 5%, respectively (See **Figure 3.20**).



**Figure 3.20.** ION measurement devices for the 13.8 kV bus

Finally, a comparison was made to a similar enough line with enough electrical distance to the Electrolytic Cleaning one; this was done to avoid any kind of meaningful interference between both. A circuit in the Pickling line was chosen for this characterization, although a big difference between it and the EC circuit is that the DC bus voltage (already higher than the one found in EC) was being fed by two parallel AFEs, even if the transformer feeding that specific circuit was of the same characteristics than the one analyzed earlier. A fragment of its one-line diagram is reproduced in **Figure 3.21**.

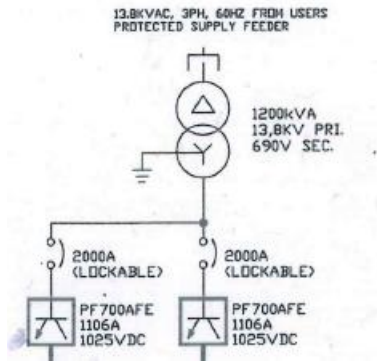


**Figure 3.21.** Pickling One-Line Diagram (Fragment)

Surprisingly, the data from all three phases was essentially clean of harmonics (see **Figure 3.22** for Phase A, for the rest Annex II), showing a clear contrast to the information found in the EC AFE circuits. In contrast, a core group of parameters (the same detailed in the next section) were checked against the operating values in the HMI, finding essentially no changes. As the line was working at that time, data recording was limited due to security reasons, but a change was noted in the leading LCL Filter. This will be also detailed in the next section.

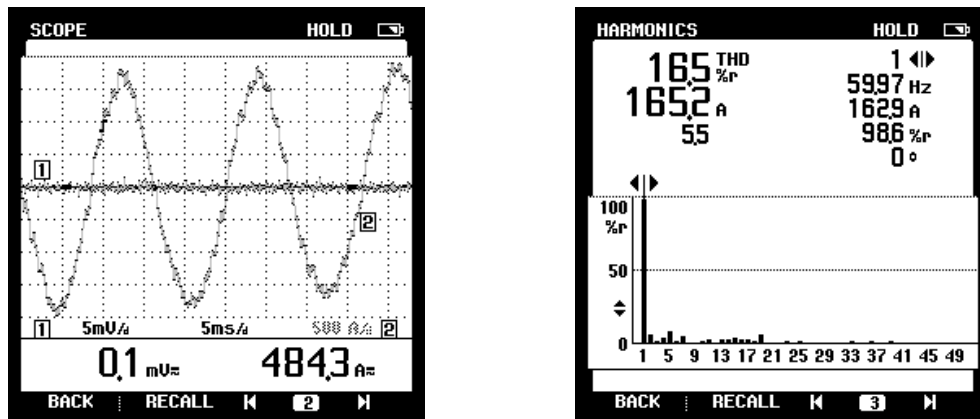


**Figure 3.22.** Waveform and spectrum of Phase A in Pickling

### 3.3. Device Characterization

At the same timeframe that the verification activities were done, physical characteristics and control parameters from the loads that were deemed relevant to the modelling of the system were either lifted from manufacturer catalogues or from the various HMIs located in the control rooms assigned to the Electrolytic Cleaning line. As for default values, they were taken from both AFE and drive manuals provided by Rockwell [25] [26] and by the Electrical Maintenance team from Ternium.

**Table 3.1** contains the data recovered from all sources pertaining to the Active Front End in operation. Meanwhile, **Table 3.2** contains all data recovered from the various HMI in charge of the loads, and **Table 3.3** is composed of data found in various Siemens and ABB product catalogues.

**Table 3.1.** AFE modelling parameters

#	Name	Value	#	Name	Value
1	Input Voltage	687 V	20	Regen MWh	0 MWh
2	AC Line Freq	59.9 Hz	21	Elapsed Run Time	5724 h
3	Total Current	113 A	30	Rated kW	1037 kW
4	Active Current	9 A	31	Rated Volts	600 V
5	Reactive Current	101.9 A	32	Rated Amps	1030 A
6	Input Current R	111 A	33	Control SW Ver	1.003
7	Input Current S	111 A	40	Nom Input Volt	690 V
8	Input Current T	102 A	41	PWM Frequency	3.6 kHz
9	I Imbalance	10 %	42	Modulation Type	2
10	Ground Current	20 A	43	Modulation Index	100 %
11	DC Bus Volt	978 V	62	DC Volt Kp	200
12	DC Bus Current	21 A	63	DC Volt Ki	0.004 s
13	AC Line kW	20 kW	64	Active I Ref	-75 A
14	AC Line kVAr	120 kVAr	65	Reactive I Ref	0 A
15	AC Line KVA	157 kVA	66	Active I Kp	400
16	Power Factor	0.05	67	Active I Ki	0.0266 s
17	Heatsink Temp	27 °C	68	Reactive I Kp	2000
18	Cmd DC Volt	978 V	69	Reactive I Ki	0.04 s
19	Motoring MWh	2.5 MWh	77	Current Lmt Val	1545 A

**Table 3.2.** Drive parameters

Parameter	Name	Description	TR	PR	B21	B22	B11	B12	Units
1	Motor NP Volts	Set to the motor nameplate rated volts	690	690	690	690	690	690 V	
2	Motor NP FLA	Set to the motor nameplate rated full load amps	883	385	200	130	77	56 A	
3	Motor NP Hertz	Set to the motor nameplate rated frequency	50.2	50	50	50	50	50 Hz	
4	Motor NP RPM	Set to the motor nameplate rated RPM	1000	990	1490	1488	1485	1485 RPM	
5	Motor NP Power	Set to the motor nameplate rated power	800	380	200	132	75	55 kW	
7	Motor Poles	Set to the number of motor poles indicated on the motor nameplate	6	6	4	4	4	4	
9	Total Inertia	Time, in seconds, for a motor coupled to a load to accelerate from zero to base speed, at rated motor torque	1.195	1.257	1.028	1.21	1.722	2.111 s	
30	Rev Speed Limit	Sets a limit on the speed reference in the negative direction	-2014	-2000	-1850	-1850	-1900	-1900 RPM	
31	Fwd Speed Limit	Sets a limit on the speed reference in the positive direction	2014	2000	1850	1850	1900	1900 RPM	
32	Accel Time	Sets the rate of acceleration for all speed increases, with time in seconds to base speed	4	4	4	4	4	4 s	
33	Decel Time	Sets the rate of deceleration for all speed decreases, with time in seconds to base speed	8	4	4	4	4	4 s	
81	Spd Reg P Gain	Sets the proportional gain of the speed regulator	11.95	12.57	10.28	12.1	20	20	
82	Spd Reg I Gain	Sets the integral gain of the speed regulator	29.87	31.41	25.69	30.25	0	0 1/sec	
301	Motor Speed Ref	Displays the speed reference value, after the limit function	0	385	190.7	0	699	33.12 RPM	
303	Motor Torque Re	Displays the reference value of motor torque	0	-0.52	-0.2	0	-0.64	-0.67 p.u.	
306	DC Bus Voltage	Displays measured bus voltage	975	975	975	975	975	981 V	
307	Output Voltage	Displays RMS line-to-line fundamental motor voltage	195	385	82	0	300	64 V	
308	Output Current	Displays measured RMS motor current	469	243	71	0	52	33 A	
336	Service Factor	Sets the minimum level of current that causes a motor overload trip under continuous operation	1.5	1.3	1.15	1.15	1	1 p.u.	
402	PWM Frequency	Sets the carrier frequency for the PWM output of the drive	2	2	2	2	2	2 kHz	
410	PreChrg TimeOu	Sets the time duration of precharge	30	30	30	30	30	30 s	
490	StatorInductance	Displays the sum of the stator and cable inductances of the motor	174.12	224.49	290.41	280.47	260.96	282.76 %	
491	StatorResistance	Displays the sum of the stator and cable resistances of the motor	0.61	1.57	1.34	1.21	2.12	2.26 %	
492	Leak Inductance	Displays the sum of the motor stator, rotor leakage, and motor cable inductances	12.98	16.41	14.4	14.75	15.61	16.55 %	
502	Rotor Resistance	Displays rotor resistance	0.29	2.97	0.43	0.68	0.61	0.73 %	

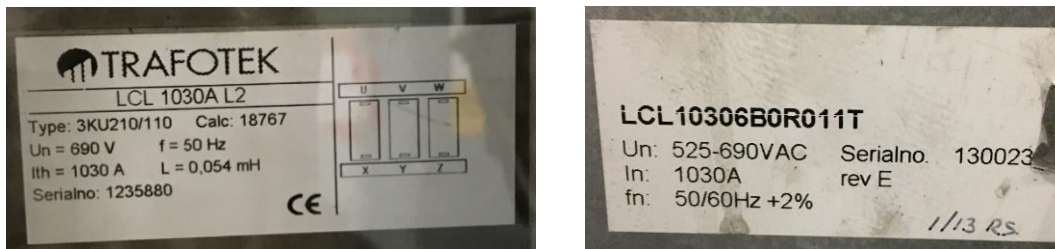


**Table 3.3.** Physical Characteristics of line motors

Manufacturer	ABB	Siemens	Siemens	Siemens	Siemens	Siemens	
Model	HXR 450LM6	1PQ8 357-6PM80	1LG6 317-4PM80-Z	1LG6 313-4PM80-Z	1LG6 280-4PM80-Z	1LG6 253-4PM80-Z	
Power Factor	0.82	0.86	0.88	0.88	0.87	0.87	
Efficiency	0.966	0.964	0.961	0.959	0.947	0.948	
Apparent Power	1009947.988	458361.4783	236496.0742	156412.9301	91031.56975	66686.06625	VA
Base Impedance	0.471410415	1.038699853	2.01314124	3.043866	5.23005372	7.139422473	Ohm
Stator Resistance	0.002875604	0.016307588	0.026976093	0.036830779	0.110877139	0.161350948	Ohm
Stator Leak Inductance	9.69974E-05	0.000271281	0.000461378	0.000714558	0.001299359	0.001880534	H
Magnetization Inductance	0.002505344	0.007150997	0.018148175	0.026459974	0.042144683	0.062378054	H
Rotor Leak Inductance	9.69974E-05	0.000271281	0.000461378	0.000714558	0.001299359	0.001880534	H
Rotor Resistance	0.00136709	0.030849386	0.008656507	0.020698289	0.031903328	0.052117784	Ohm
Magnetization Current	291.7910876	113.4280829	54.8452368	35.64940392	21.91909289	15.94115847	A
Rated Flux	0.731036995	0.811123885	0.995340952	0.943282285	0.923773211	0.994378452	Wb
Motor Inertia	49	16	4.2	2.9	1.4	0.86	kgm2
Rated Torque	7638	3658	1282	847	482	354	Nm
Acceleration Ramp	250	247.5	372.5	372	371.25	371.25	rpm/s
Deceleration Ramp	-125	-247.5	-372.5	-372	-371.25	-371.25	rpm/s
Shaft Diameter	110	95	80	80	75	65	mm
Gear Ratio	6.7	6.7	11	11	11	11	

Aside from the aforementioned data, the installation of the devices was classified as usual, so the model would not diverge too much from the mathematical basis presented earlier and in the manuals.

Beyond that, the sole source of uncertainty within all physical elements was the LCL Filter, as it doesn't have much information beyond some basic data (shown in **Figure 3.23**) stamped in its structure because the manufacturer sells it as a part of a tuned set with the Active Front End.

**Figure 3.23.** Data stickers placed on the LCL filter

Because of the importance of having the entire parameter set from the actual system it was deemed necessary to make some tests on the unit – something initially not allowed on it as it was vital for the continuous operation of the system. Fortunately, a redundant unit was available in storage, and after confirming it was indeed the same unit the data present in **Table 3.4** was obtained, corresponding to the circuit in **Figure 3.24**.



**Table 3.4.** LCL Filter electrical data (per-phase)

Parameter	Value
<b>Grid-side inductance</b>	54 $\mu$ H
<b>Common mode capacitance</b>	10 $\mu$ F
<b>Filter capacitance</b>	159 $\mu$ F
<b>Filter-side inductance</b>	162 $\mu$ H

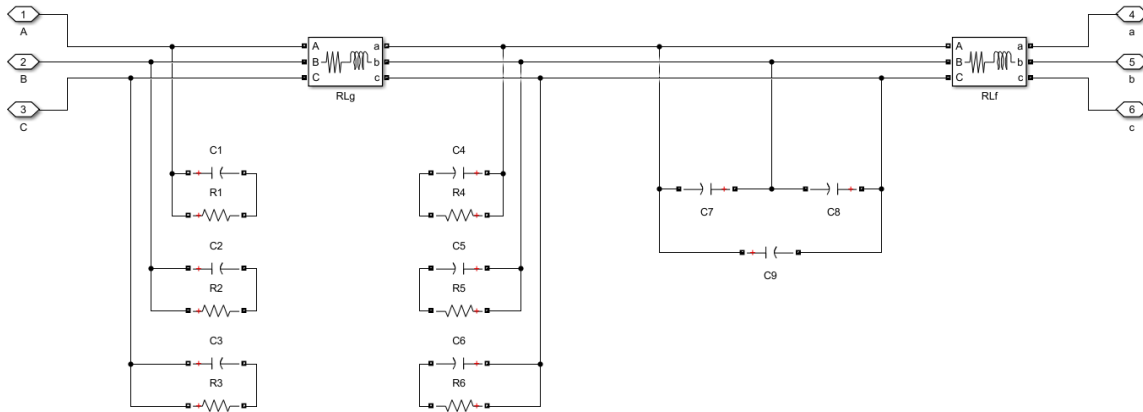


**Figure 3.24.** Electric diagram of current LCL Filter in EC line

The previous table contains the equivalent values of capacitance for the sake of simplification, in real life the wye-capacitance is provided by two 20  $\mu$ F connected in series, while the delta capacitance is composed of three 53  $\mu$ F capacitors connected in parallel.

One interesting detail that jumps is the fact that the common mode capacitors are not connected to ground (shown in **Figure 3.25** with the actual units). This was an interesting development, as Rockwell [25] and at least another manufacturer [33] don't consider this practice until one of two conditions is met:

1. The Active Front End is installed on a high resistance grounded distribution system
2. The AFE is connected to an ungrounded distribution where line-to-ground voltages on any phase exceed 125% of the nominal line-to-line value.

As neither of those conditions really apply to Pesquería Plant, the rationale on why the line is permitted to operate in this manner appears to be faulty.

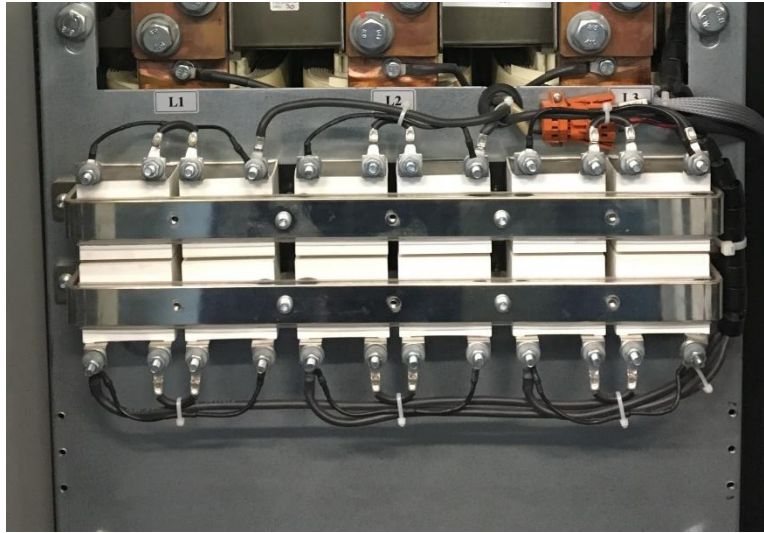


**Figure 3.25.** Common-mode capacitor condition in EC line

This is even more strange when the Pickling line is considered – as their power supply is quite similar – but in that installation the capacitors were properly grounded (see **Figure 3.26**).



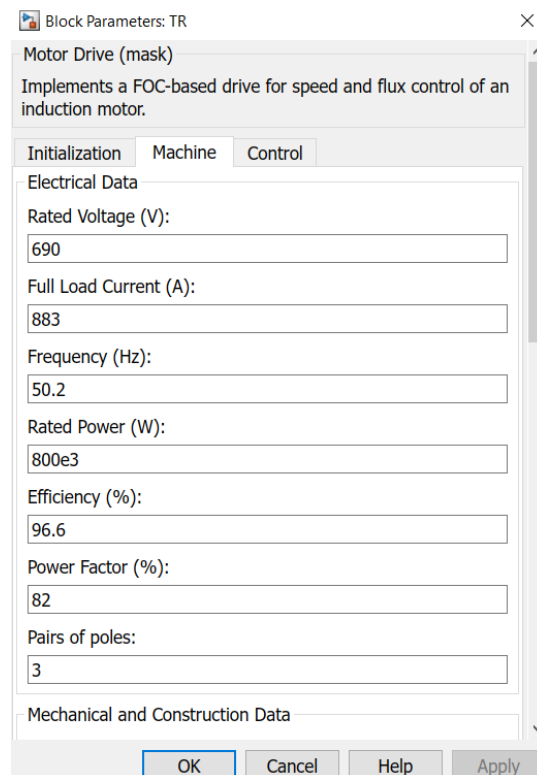
**Figure 3.26.** Common-mode capacitor condition in Pickling line

### 3.4. Load Modelling

With all data gathered the modelling in Simulink could properly begin. For the creation of the model the *Simscape Power Systems* library was vital, alongside its reference manual [18] and the vast amount of online documentation provided by The MathWorks. The complete modelled loading topology can be found in **Figure 3.28**.

It can be seen in the mentioned picture that the loads in the Electrolytic Cleaning circuit are connected to an infinite bus, but in the complete model used for the upcoming Results chapter the whole model is connected, rectifier and inverters. The image was only produced for the sake of having a clear picture of the load side.

As for the loads, the Rockwell drives that are used for control in the actual line clearly indicate they work under a Field Oriented Control scheme [26]. As such, the MATLAB models are based in the diagram shown in the section concerning FOC back in Chapter 2.



The screenshot shows the 'Block Parameters: TR' dialog box for a 'Motor Drive (mask)'. The dialog has three tabs: 'Initialization', 'Machine', and 'Control'. The 'Machine' tab is selected. Under the 'Electrical Data' section, the following parameters are listed:

- Rated Voltage (V): 690
- Full Load Current (A): 883
- Frequency (Hz): 50.2
- Rated Power (W): 800e3
- Efficiency (%): 96.6
- Power Factor (%): 82
- Pairs of poles: 3

Below the 'Electrical Data' section is the 'Mechanical and Construction Data' section, which is currently empty. At the bottom of the dialog are four buttons: 'OK', 'Cancel', 'Help', and 'Apply'.

**Figure 3.27.** Data mask for Tension Reel load

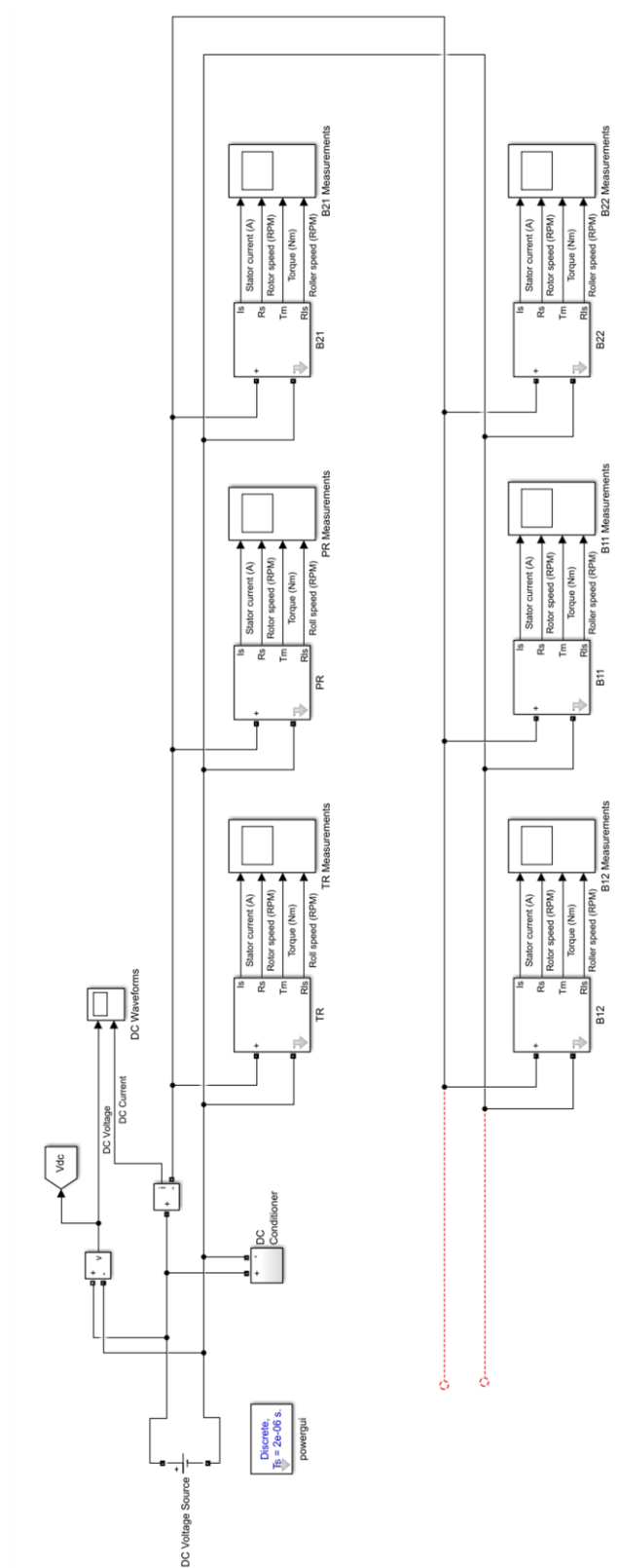


**Figure 3.28.** Inverter portion of the modelled system in Simulink

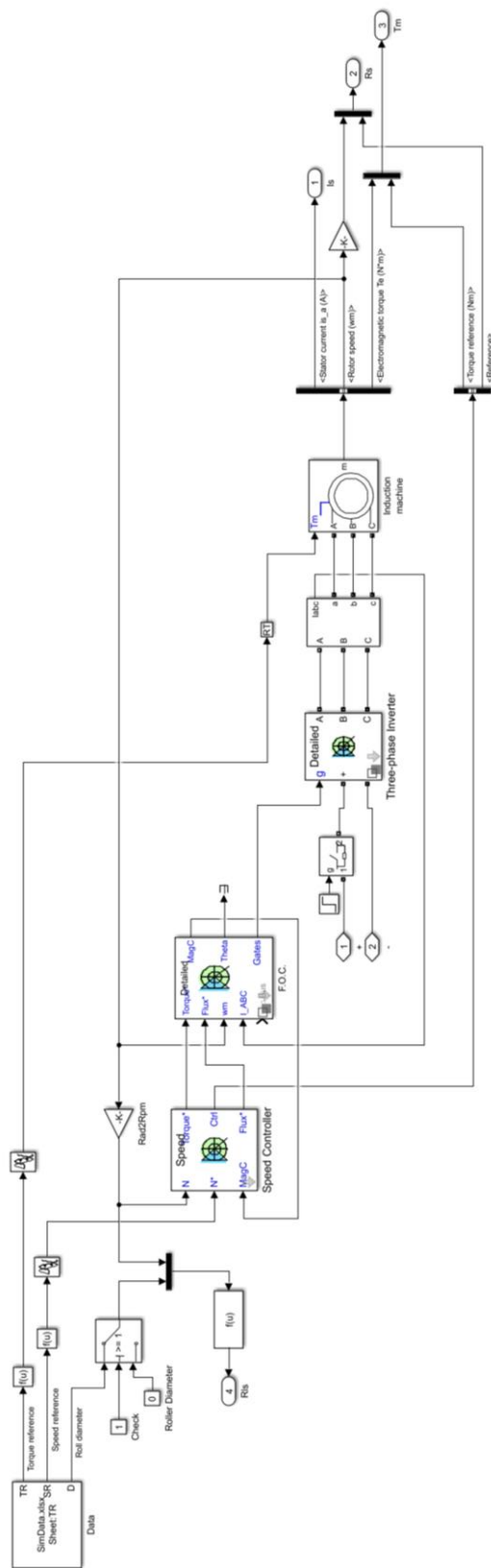
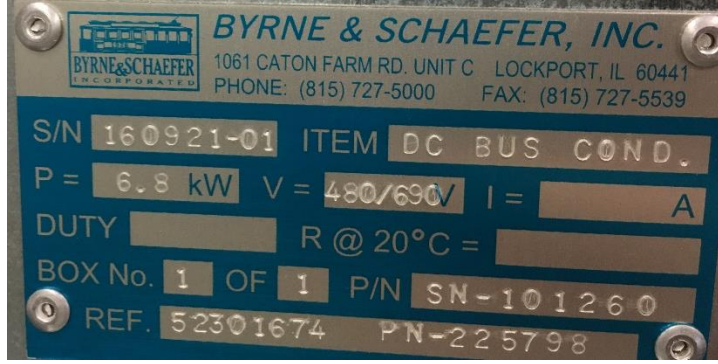


Figure 3.29. Internal schematic of modelled motor drive

Each one of the drives is modelled through a Simulink block subsystem (as seen in **Figure 3.29**), concealed behind programmatical masks as the one shown in **Figure 3.27** for the sake of ease of access and limit potential human error when entering parameter data. Said masks work with nominal data taken from the manufacturer of the motor load and control parameters directly taken from the working HMI, the same data seen in **Table 3.2** and **3.3**. From the same picture, a DC conditioner based on the recently installed one was modelled using the plate data visible in **Figure 3.30**.



**Figure 3.30.** DC Bus Conditioner plate data

From **Figure 3.29**, a Speed Controller and a Field Oriented Controller are used inside each of the loads. These are based on MATLAB blocks present in the Simscape Power Systems Library, which use the nominal values of the machine and the control parameters to control the flux vector – as explained in **Figure 2.22**. The output switching logic is then fed to an inverter which feeds the modelled induction machine.

Said induction machine works with a nominal flux value, which was calculated according to [1]:

$$i_{mag} = \frac{1}{\sqrt{3}} i_{nom} (\sqrt{1 - PF^2}) \quad (3.1)$$

Which is based on the premise that the current that is not used for work is needed for flux generation, which concludes in **Equation 3.2**.

$$\phi_{nom} = i_{mag} L_{mag} \quad (3.1)$$

As for the speed and torque references that are needed for both the induction machine and the speed controller, they are lifted from field data recovered by the internal systems at Ternium, obtained through files visible in the ibaAnalyzer program, as **Figure 3.31** shows:

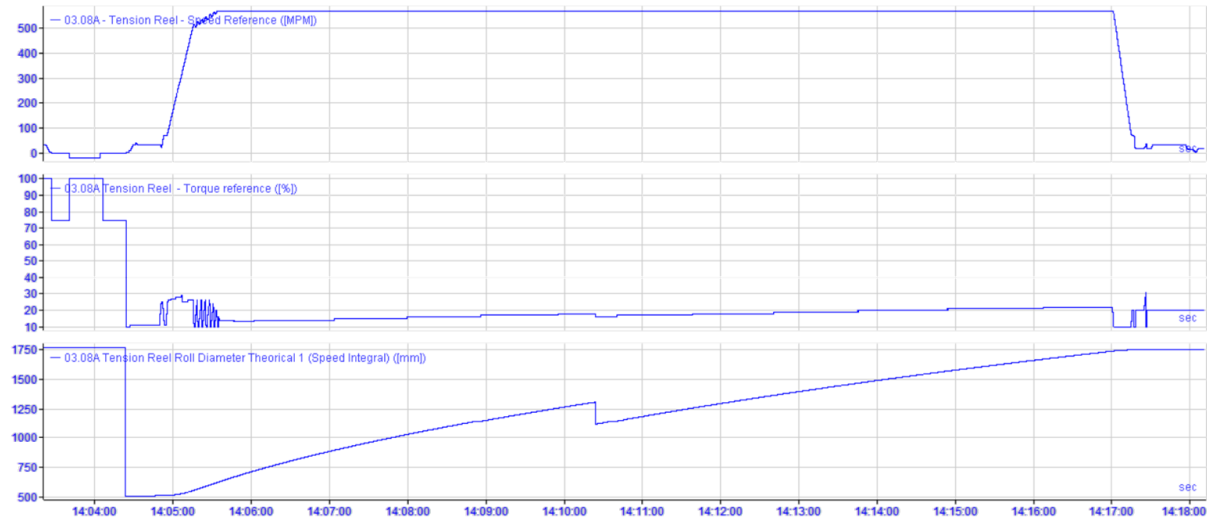


**Figure 3.31.** Tension Reel Data during roll processing in ibaAnalyzer

For all six loads – Tension Reel, Pay Off Reel, Bridle Roll 1 Unit 1 and 2, and Bridle Roll 2 Unit 1 and 2 – data to use as reference was recovered during the processing of a roll, specifically one passing through the line on November 14<sup>th</sup>, 2016 between 14:04 and 14:18 (according to ibaAnalyzer registries). Two variables were taken for each load:

- Speed reference in MPM
- Torque reference as a percentage of the nominal value

Additionally, a third variable was taken for both the Tension Reel and the Pay Off Reel – the calculated diameter of the roll in each side of the line, for the sake of obtaining the speed of the roll seen from each side of the simulated line. For the each of the Bridle loads, the roller speed is displayed instead.

The data obtained in ibaAnalyzer was then exported to a text file, which was then taken to an Excel worksheet for the sake of clarity and compatibility with Simulink. Said data was then reorganized into recognizable sets and sheets to be easily understandable by outsiders, and then passed through embedded conversions as the Simulink blocks have expected units.

From the model, the data obtained from the load side comprises:

- DC voltage (V)
- DC current (A)
- Stator current (A)
- Rotor speed (RPM)
- Torque (N·m)
- Roll / Roller speed (RPM)

The model is compatible with both Excel 97-2003 (.xls) and 2007-2016 (.xlsx) formats, and it also works with Comma Separated Values files (.csv), as **Figure 3.32** shows. The same figure also makes it clear that the load model is universal, as both roll and roller parameters are accepted, depending on what type of load is needed.

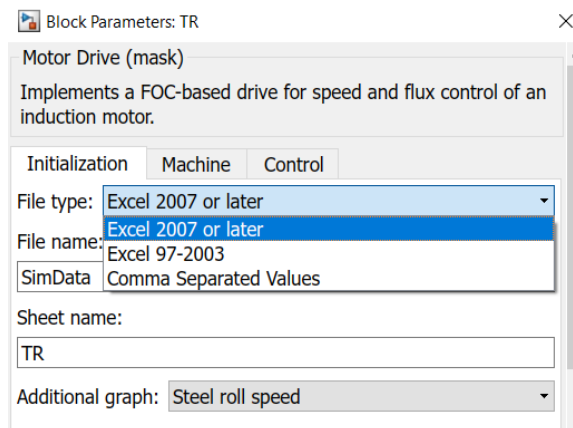


**Figure 3.32.** File types accepted as reference

A point to consider is the fact that the entire model uses a fixed-step model, as the controllers are not compatible with continuous simulation solvers such as ode45 or ode23. As such, a fixed step size of  $2 \times 10^{-6} s$  is used through the entire simulation, while controllers used sample step sizes of  $20 \times 10^{-6} s$  and  $100 \times 10^{-6} s$ .



### 3.5. Rectifier Modelling

In a similar way to the loads, the Active Front End circuit (as seen in **Figure 3.33**) was modelled in Simulink using the Simscape Power Systems library. As proposed by Aswathi in [7], the model that was generated complies with the characteristic control behavior explained in Chapter 2.

All data in the simulation was obtained through both field visits and data plate information, although some concessions were done with the control algorithm of the Active Front End. In that specific case, and in contrast to the amount of data found in the manual of the drive systems used in the Electrolytic Cleaning line, the manual for the AFE was slim in the amount of detail given about its control method. Nevertheless, it confirmed the use of feedback loops for current control and power factor manipulation [25].

As no manufacturer data was available, the actual AFE system can be considered a black box one. So, all data obtained through the model has the caveat that it may not be entirely compatible with field values. Aside from that, the manual also confirmed the use of sine-triangle PWM. The frequency of the carrier is as stated in **Table 3.1**, 3.6 kHz.

Another caveat of the whole model is the use of a X/R factor of 10 for the sake of stability during simulation, a value considered as common in high power settings. Only when the resistance data was available was such consideration ignored.

As for the LCL Filter (with a structure just like the one in **Figure 3.24**) and the AFE, both were modelled as subsystems under programmed masks in the interest of avoiding human error to the minimum and speeding the model construction by using HMI and plate data. Those interfaces can be seen in **Figure 3.35**.

Both the 13.8 kV power source and the  $\Delta/Y_g$  transformer data were cross-referenced to both the general and the area-specific one line diagram, with the input values in the transformer using the per unit system.



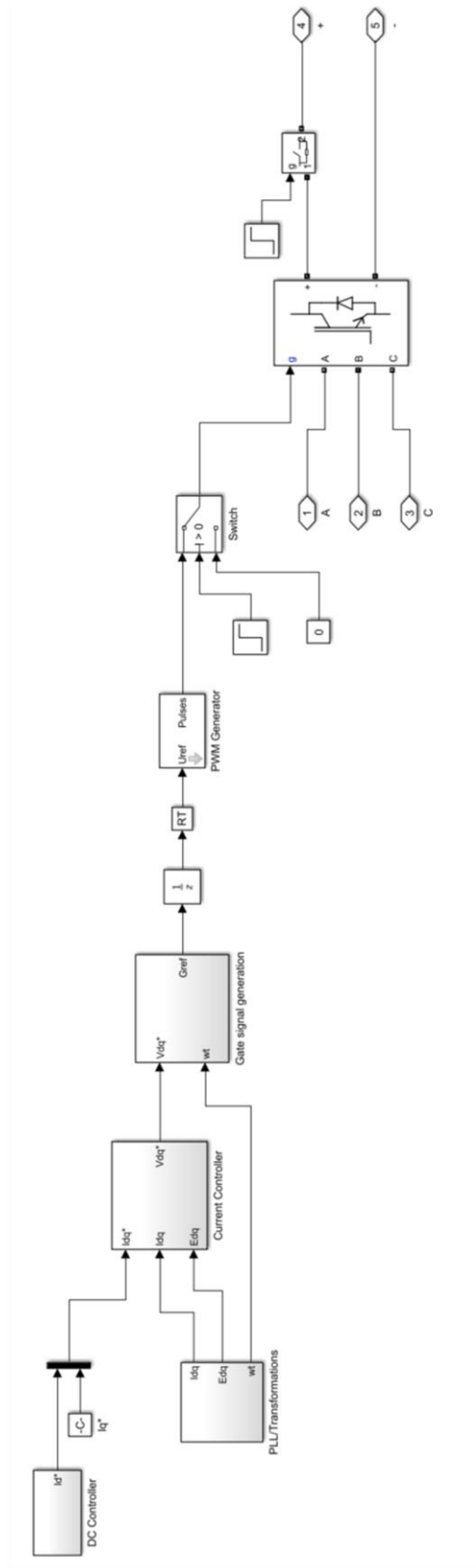


**Figure 3.34.** Modelled Active Front End control structure

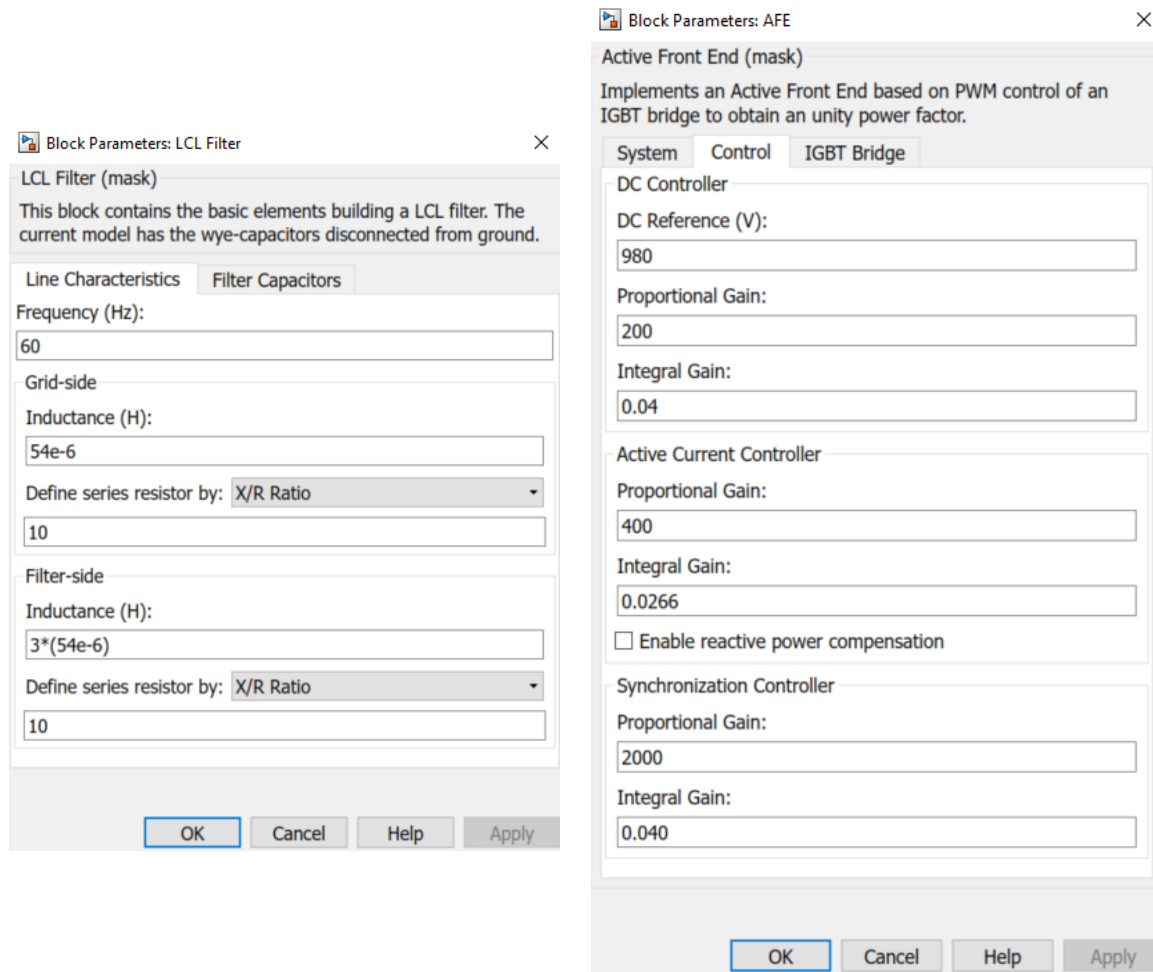


**Figure 3.35.** Interface mask for the LCL filter and the Active Front End

The transformer is based on a three-limb core model pre-existent in Simulink, with the consideration from plate data of a 13.8 kV / 690 V unit with 5.8% impedance. The calculation and transformation of its data to the per unit system is shown in **Table 3.5**.

**Table 3.5.** Transformer impedance data

<i>High Voltage</i>	R <sub>base</sub>	457.0560 Ω	R	1.3254624 Ω	2.90×10 <sup>-3</sup> pu
	L <sub>base</sub>	1.2124 H	L	3.5159×10 <sup>-2</sup> H	2.90×10 <sup>-2</sup> pu
<i>Low Voltage</i>	R <sub>base</sub>	0.3809 Ω	R	1.1046×10 <sup>-3</sup> Ω	2.90×10 <sup>-3</sup> pu
	L <sub>base</sub>	1.0103×10 <sup>-3</sup> H	L	2.9299×10 <sup>-5</sup> H	2.90×10 <sup>-2</sup> pu

The pre-charge circuit is composed of a simple diode rectifier, with a 5% leading impedance. The DC side includes a 10 μF capacitor and a 1 Ω resistor, with values taken from Rockwell catalogues.

The main control scheme (shown in **Figure 3.34**) works as explained in Chapter 2, with the DC controller supplying the active current reference, and the reactive current taking a zero-reference value – although the model is prepared to supply a different value if the need arises. The voltage and current measurements go through a phase-locked loop to synchronize their  $dq$  transformation to the actual frequency circulating through the system.

The main difference when compared to the Theoretical Framework version is a series of compensations happening during the gate switching reference stage, mainly to make up for the fact that the controller runs at a sampling rate lower than the rest of model ( $2 \times 10^{-6}$  s vs  $100 \times 10^{-4}$  s). The output signal then enters a sine-carrier PWM algorithm to produce the pulse train destined for rectifier control.

A closeup of the main stages of control may be observed in **Figure 3.36**.

This side of the model outputs several variables, both from the three-phase supply system and the same DC bus signals as the load circuit:

- AC Voltage waveforms (V)
- AC Current waveforms (A)
- Active Power (kW)
- Displacement Reactive Power (kVAr)
- Distortion Reactive Power (kVAd)
- Power Factor
- Harmonic spectrum and THD
- DC Voltage (V)
- DC Current (A)

The differencing between the components of the reactive power is to differentiate the impact of harmonic distortion from the lack of synchronization made by the inherent reactance in the system.

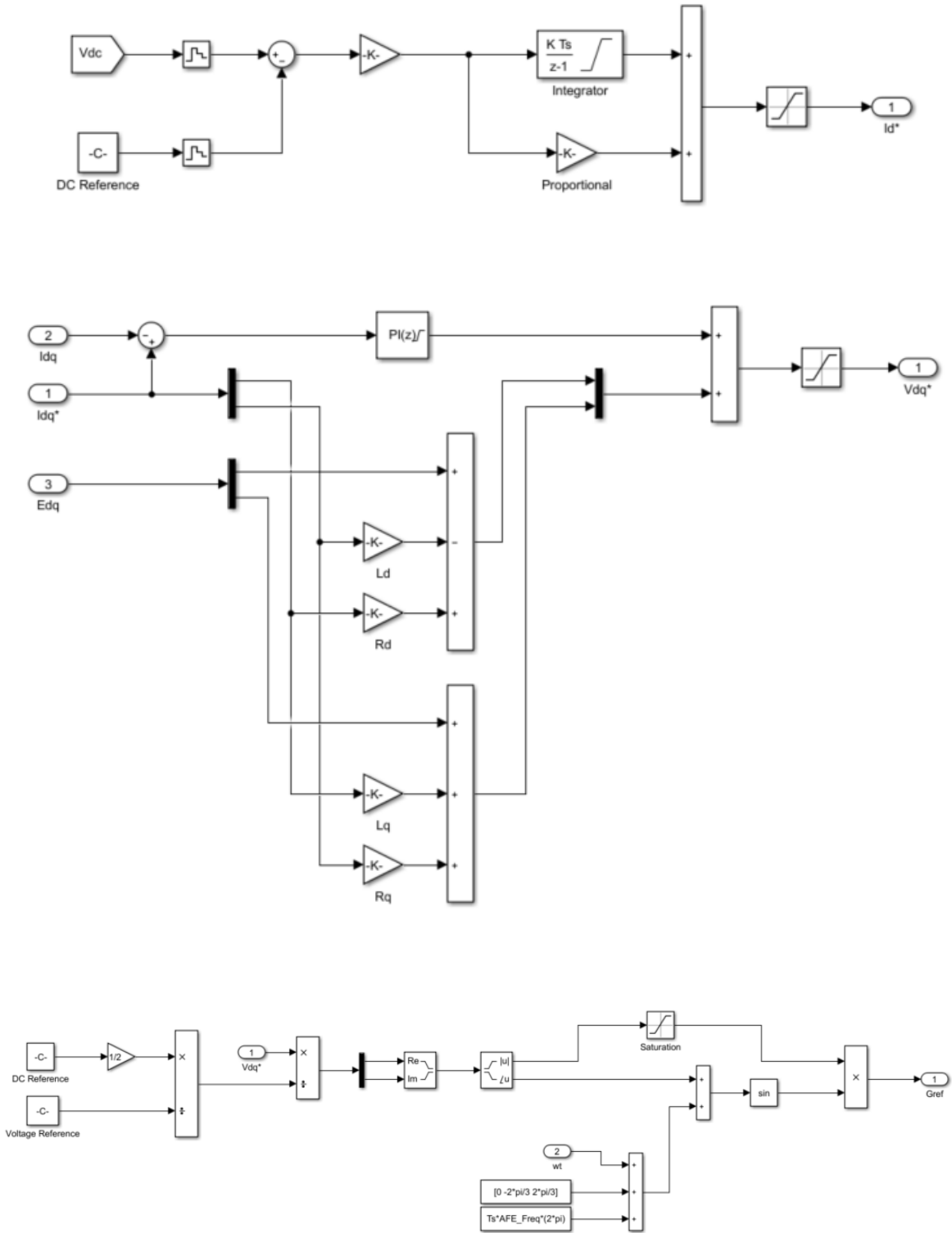


**Figure 3.36.** DC and Current Controller, and timing compensation in modelled AFE

## IV. Results and Discussion

The finished modelled system can be seen in **Figure 4.4**. It incorporates both rectifier and load topologies, and all the data mentioned in the last chapter can be obtained.

The total simulation time for effects of this documents was 900 s, around the same time it took the roll process used as reference data for the load internal controllers to go through the Electrolytic Cleaning line in its entirety.

As a caveat for the entire dataset that will be presented, and because of the step size used for the sake of the controllers in both rectifier and inverter elements in the model, each resulting variable was downsampled in a 100x manner. This was done because each variable at the end of the simulation surpassed the 200-million-point barrier per vector, making its treatment unfeasible for the computational capabilities available for this work. Initial tests with a limited set of data proved that an insignificant amount of variability was lost when applying such downsampling with MATLAB internal algorithms.

As for the simulation itself, it took around 4 days and half of continuous operation from start to finish.

After the simulation was done, the pattern described by all phases of AC voltage and AC current through the entire period was as it is shown in **Figure 4.1** and **4.2**.

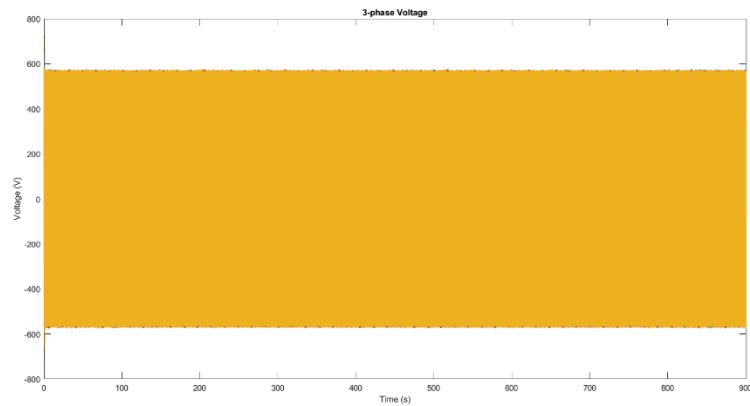


**Figure 4.1.** Voltage pattern during simulation

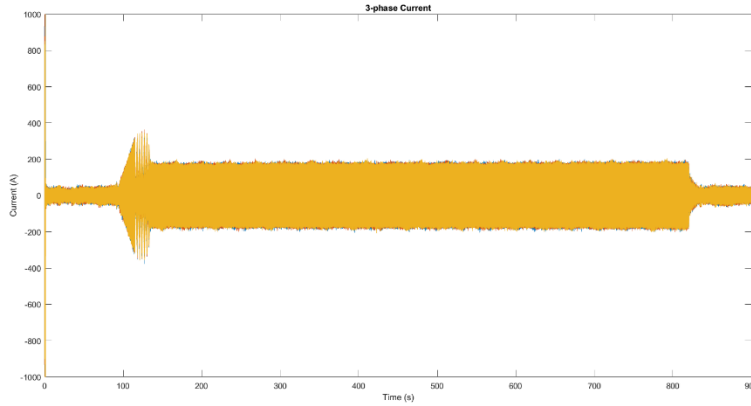


**Figure 4.2.** Current pattern during simulation period

While the voltage stood pretty much unchanged from its nominal value, the current experienced three main stages after the initialization transients: two periods with a low magnitude at each extreme of the graphic shown in **Figure 4.2**, and a long period with a peak phase-to-ground value of 200 A. Those pattern means the existence of low and high loading periods, equivalent to the moments a steel roll is being slowly processed or when it is going through at peak speed.

Comparing that graph to the average RMS current value obtained in-line for the same period (see **Figure 4.3**), it can be observed that the obtained values are similar. Nevertheless, the real line presented some transients around the end of the process that are not present in the model. There is also an increase in current around the second half of the roll going through at the line; this can be attributed to the operator of the line accelerating the real roll for the sake of maintaining or increasing the production level of the line.

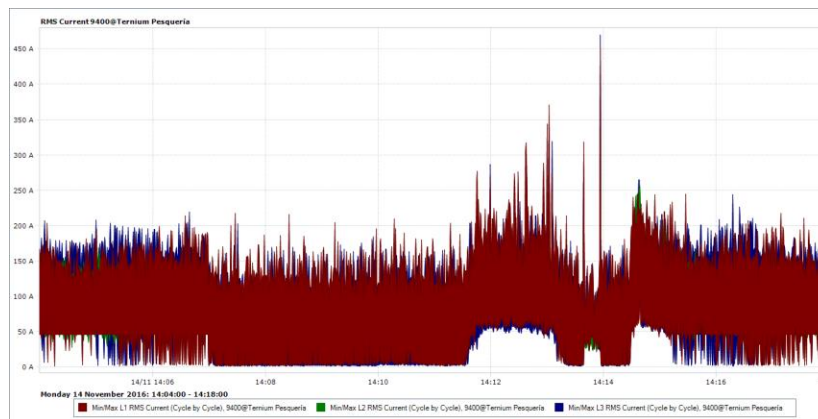


**Figure 4.3.** RMS current during operation





Meanwhile, the power distribution took the form shown in **Figure 4.5**.

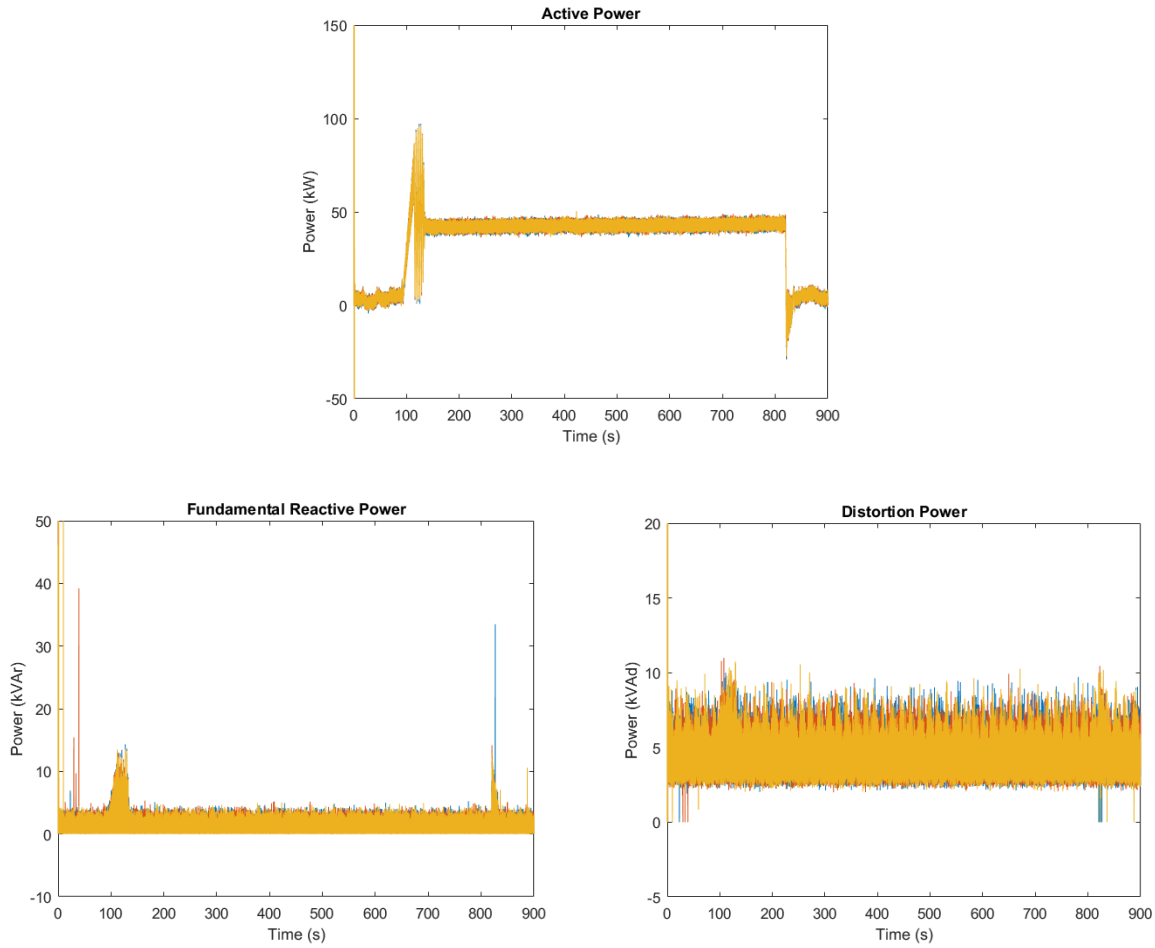


**Figure 4.5.** Power Distribution during simulation

During the simulation, the maximum demanded power from the distribution network totaled around 100 kW in the height of acceleration, then lowering to around 50 kW while the roll was speeding through the line – something that may be attributed to model deficiencies. Parallel to such performance, the reactive power components totaled 10 kVAr by themselves, implying there is a significant amount of reactive power during normal operation. When comparing these results against real data, the simulation compared in a favorable way to the data obtained through the ELSPEC device in the transformer (see **Figure 4.6**).

The biggest difference between both datasets is the amount of variability in the behavior of the powers detected by the power quality measurement device, as they tend to oscillate

between further apart magnitudes compared to the simulation. Also, in real life the amount of reactive power is higher than what was obtained through the model.

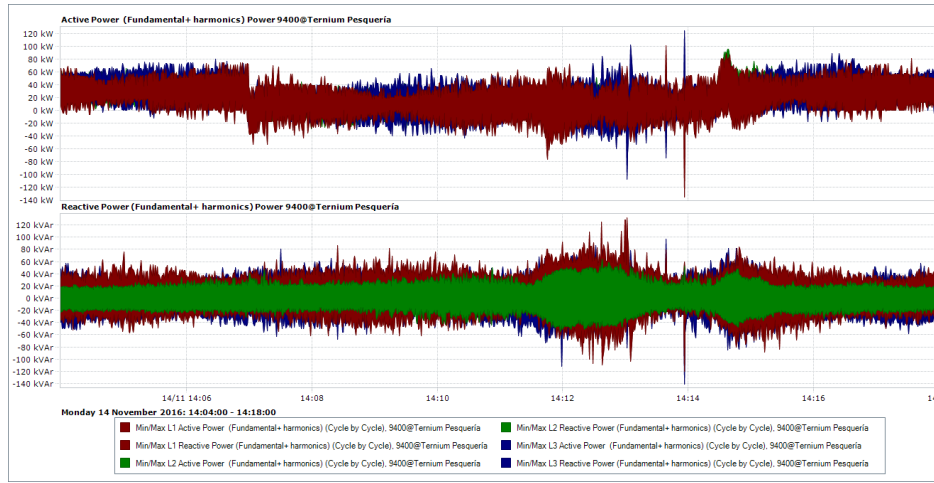


**Figure 4.6.** Active and reactive power during roll processing

The influence that such changes would have in the power factor in both data sets is undeniable, as the comparison between the simulation and the real data shows (see **Figure 4.7** and **4.8**). For the ELSPEC-captured data, the power factor during the main process was oscillating around the inductive and capacitive sides of the PF spectrum, although its tendency is clearly orientated towards lower values in the inductive side of the graph. This may indicate either a high amount of harmonic content or a big offset between currents and voltages; such findings become egregious when compared to the almost-UPF simulation results.

This is more critical when dealing with an Active Front End – considering that control of the power factor is a defining characteristic of an AFE system, it is cause of concern that it falls in such an obstreperous manner. It would indicate a problem in the control parametrization of the machine, which has its characteristics deliberately obfuscated by the manufacturer.

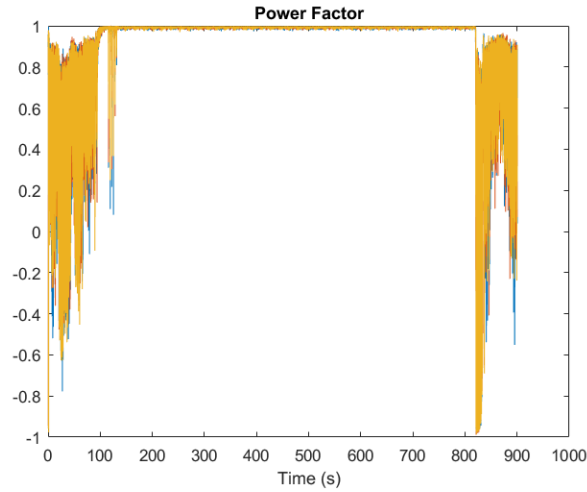


**Figure 4.7.** Simulation Power Factor

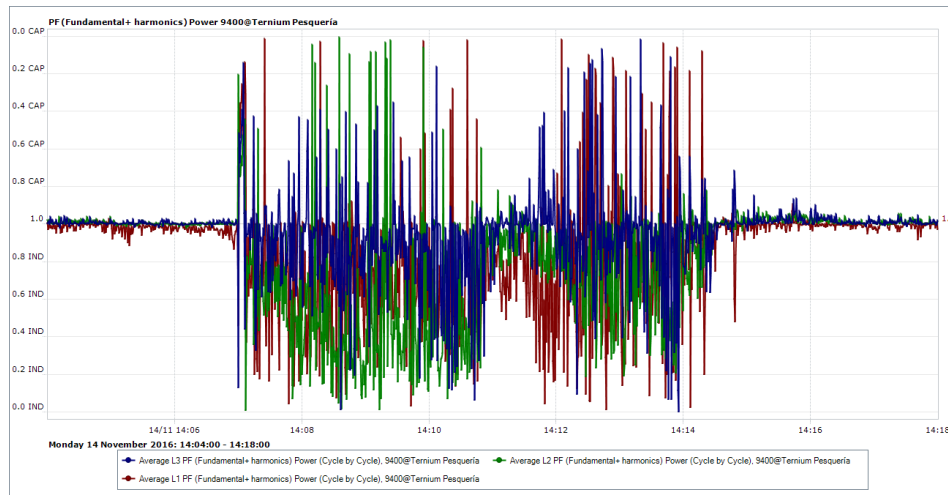


**Figure 4.8.** Average power factor, per phase

For the sake of a more apt comparison, a 100 ms sample was taken during the period with low power factor and from the period with an almost UPF operation. As **Figure 4.9** shows, during the selected sample taken from the first subset of data there is some distortion in the voltage waveforms, while the currents present a high amount of harmonic content in comparison.

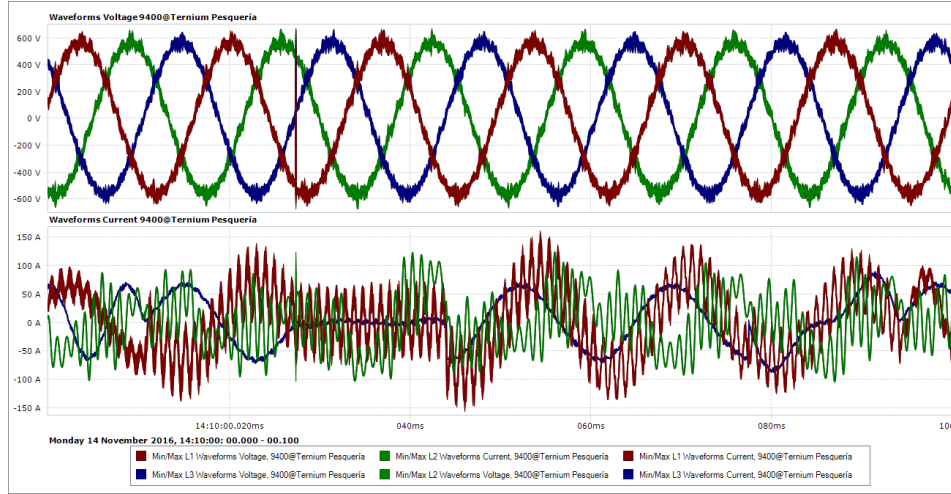


**Figure 4.9.** LPF operation, 100 ms sample

This would indicate that operation of the controller is erratic at best, as there is a high amount of distortion and displacement between voltage and current. Its worst showing is in Phase C, where it falls to 0 A for a cycle. A fuller picture might be drawn by producing the harmonic spectrum displayed by both signals, shown in **Figure 4.10**.

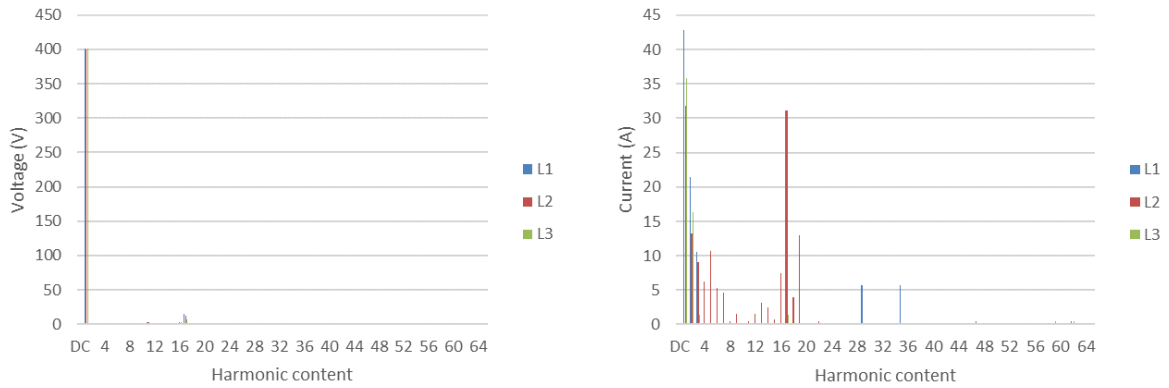


**Figure 4.10.** Harmonic spectrum for 100 ms sample during LPF operation

Like the initial results exposed in the Methodology chapter, the 17<sup>th</sup> harmonic is predominant in all phases of the current, reaching around 75% of the fundamental value. There is also an important number of low-order harmonics components in Phase B, an expected result considering its waveform, while Phase A contains harmonics around the 30<sup>th</sup>. As for the carrier frequency, its value is insignificant, so it can be concluded that the LCL filter is properly making its function.

Meanwhile, the picture painted by the high-power factor operation (see **Figure 4.11**) is a different one:

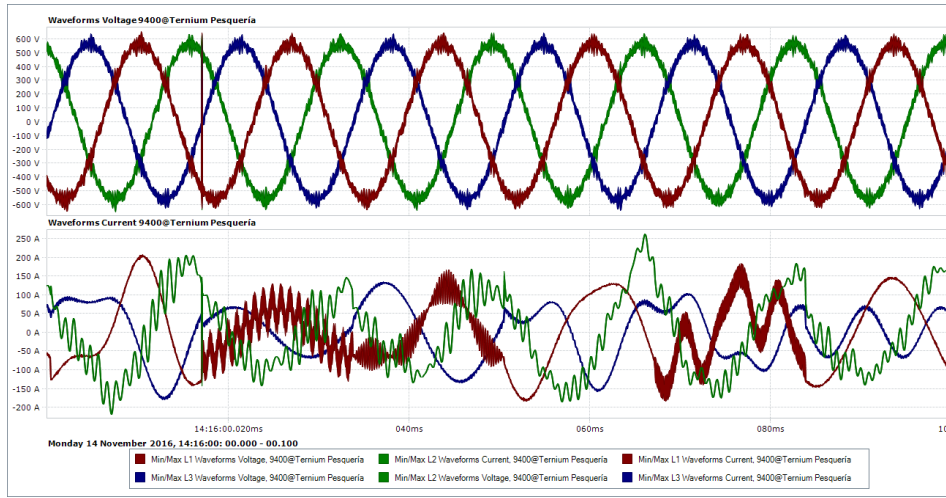


**Figure 4.11.** HPF operation, 100 ms sample

The distortion is diminished in both voltage and current waveforms, and from inspection the fundamental waveform is in phase with the voltages. Nevertheless, the currents still present an important amount of distortion, as the spectrum in **Figure 4.12** shows.

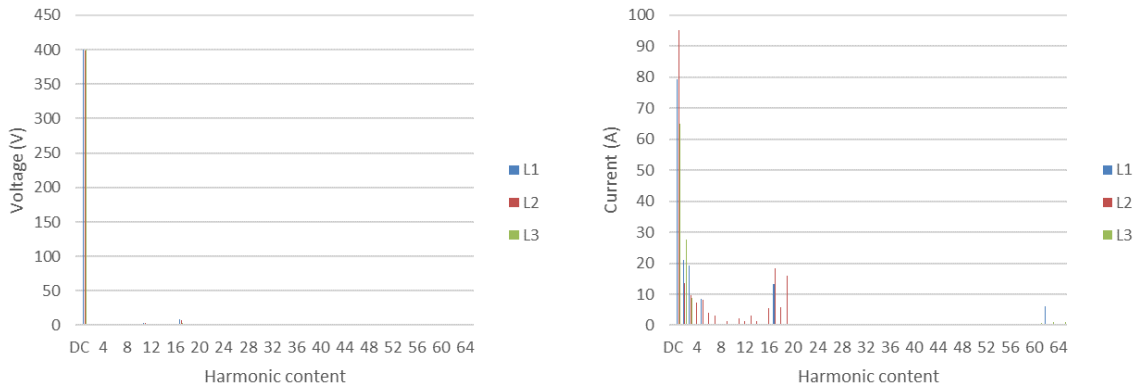


**Figure 4.12.** Harmonic spectrum for 100 ms during HPF operation

In contrast to the results in LPF operation, this subset of data presents negligible voltage distortion, and the highest current harmonic component – the 17<sup>th</sup> – only takes a value around 20% of the fundamental. As for the reason this discrepancy appears, it is plausible to be originated in the control scheme, as the torque and speed references stay equal for the period when most of the steel roll is processed.

As for the simulation, the behavior of the roll processing is quite different, with the modelled control scheme keeping the amount of distortion in the current limited, while the voltage distortion is almost inexistent (see **Figure 4.13**).

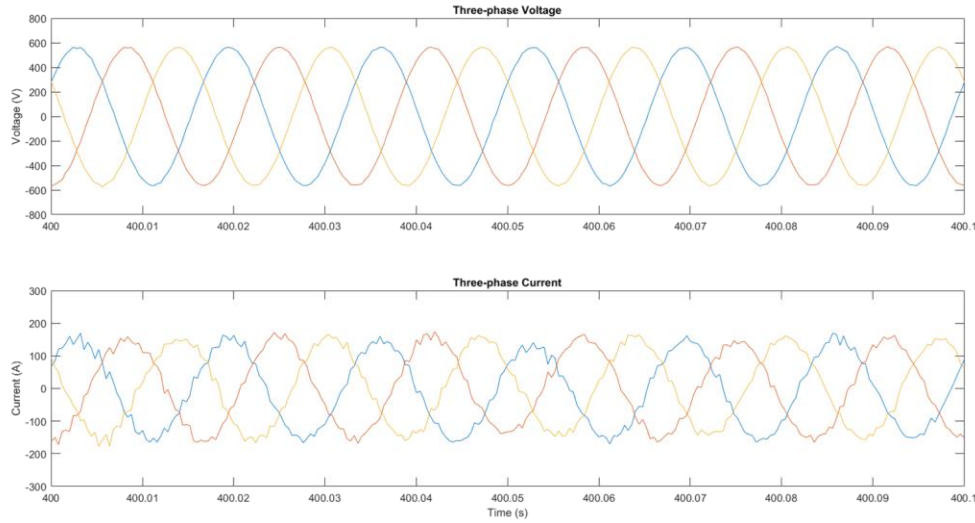


**Figure 4.13.** Simulation results during full speed processing, 100 ms sample

Meanwhile, the harmonic content has similar distribution of harmonics, although both the pervasiveness of harmonic distortion in the current and the harmonic multiple with the highest value differ from what is seen in reality. As **Figure 4.14** shows, voltage distortion is irrelevant in the simulation, taking values lower than 0.45% of the fundamental magnitude. As for the currents, the highest distortion component while simulating is less than 4% of the fundamental, centering around an interharmonic 14.5 times the fundamental frequency, 870 Hz.

As for the reason there is such a disconnect between the harmonic spectrum results of the simulation when compared with real data, the next section will deal with that.

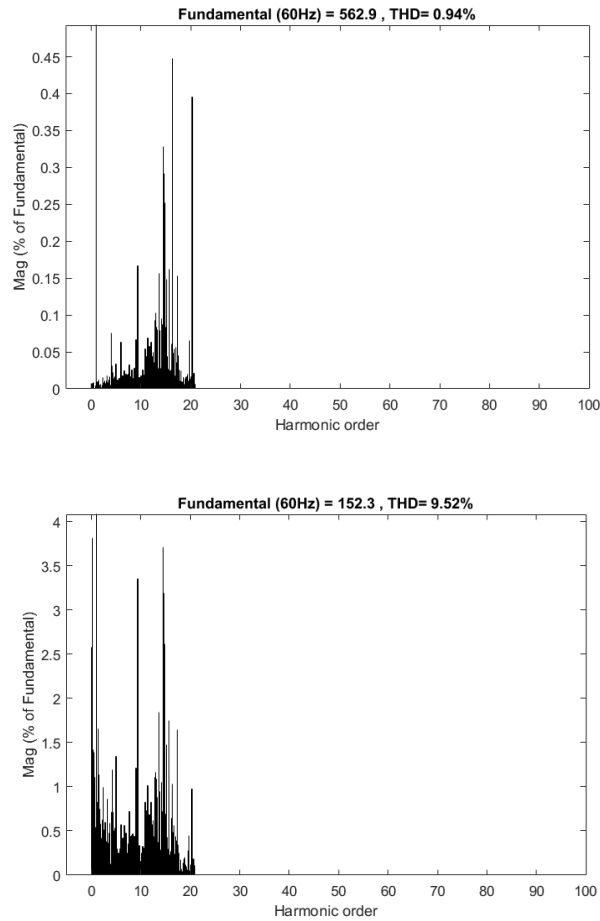


**Figure 4.14.** Harmonic content during simulation, 100 ms sample during full speed

As for the rest of the model, its behavior fell into what was expected from, with some caveats because of the size of the simulation step. **Figure 4.15** shows the voltage and current of the DC bus.

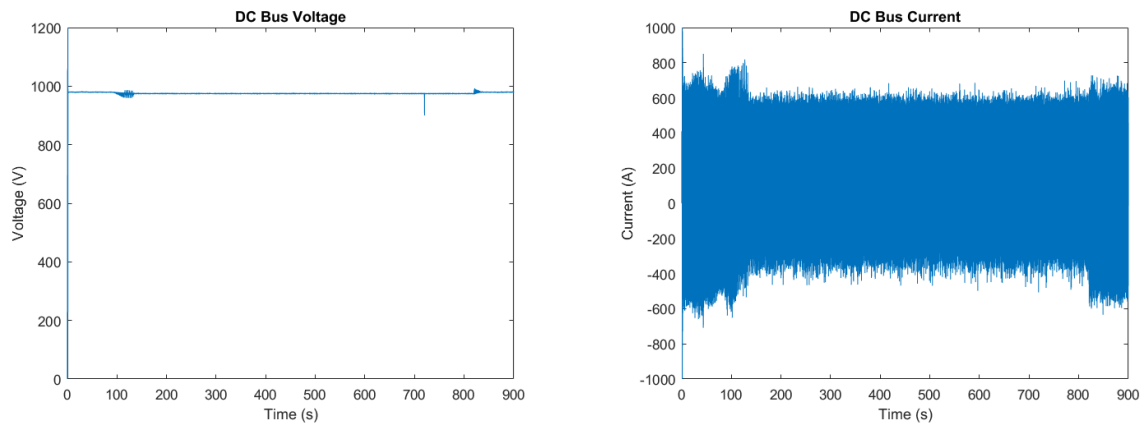


**Figure 4.15.** DC Voltage and Current



As **Figures 4.16** and **4.17** show, the Tension Roll motor complies with the dictated references taken from the ibaAnalyzer data. As for the torque – in all loads, as seen in Annex III – the variation around the value taken from the Excel source can be explained as a consequence of the stepsize used for the simulation. It was found that when the value of the step is further reduced, the torque output is less variant than the behavior seen in **Figure 4.16**, but it comes at the cost of even more points being calculated – a prohibitive measure considering the computational resources available for this project.

Regrettably, as no load data was stored by the line during the research project, it was impossible to obtain patterns from the actual process and compare both outputs.

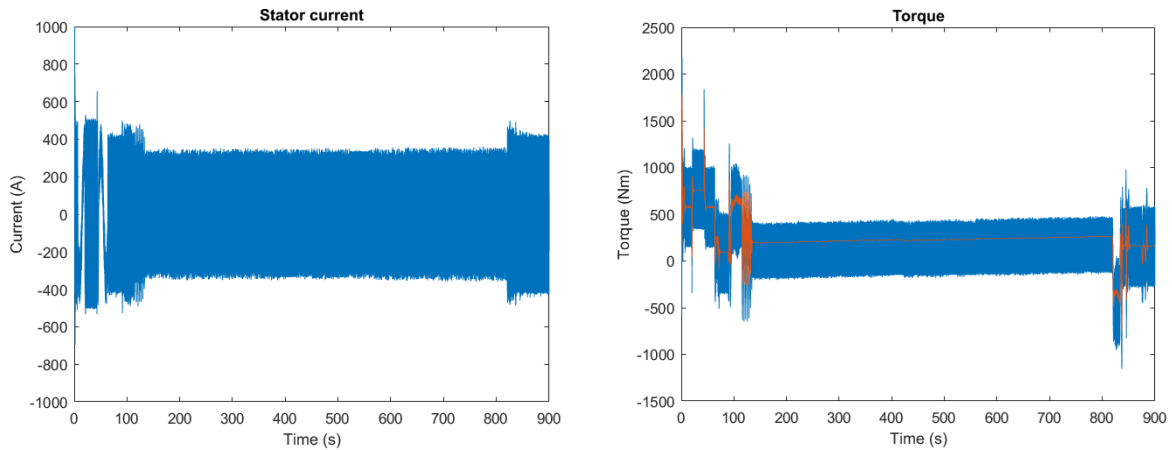


**Figure 4.16.** Stator current and Torque, Tension Reel

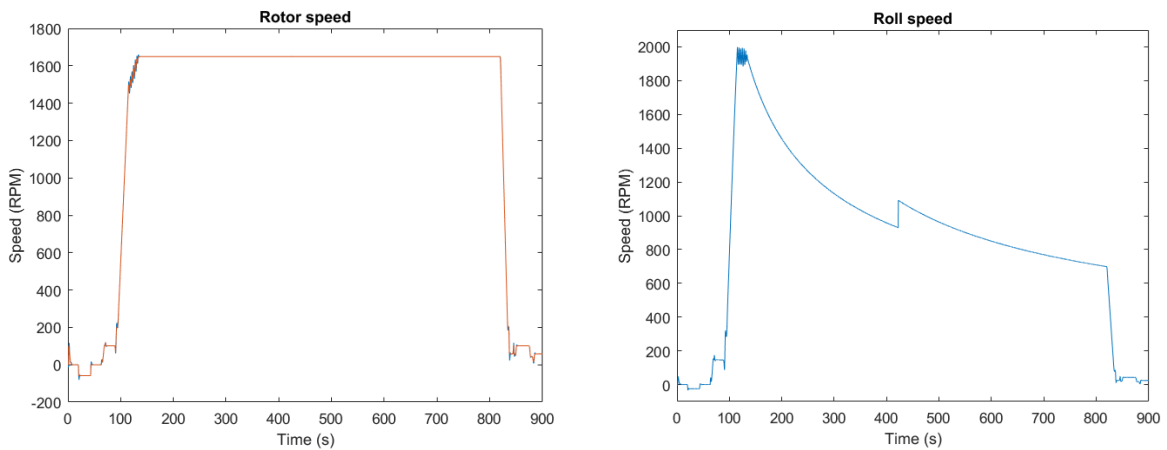


**Figure 4.17.** Rotor and roll speed, Tension Reel

#### 4.1. LCL Filter Resonance

Both the data obtained through normal operation and the simulation results include a high amount of 15<sup>th</sup>-19<sup>th</sup> harmonic content, which can be explained through a resonance analysis of the LCL filter – a common problem in Active Front End topologies [23]. To do so, the superposition principle can be applied to decouple fundamental and harmonic behavior, so in the second case the power source may be shorted and the rectifier replaced by a harmonic source (see **Figure 4.18**).

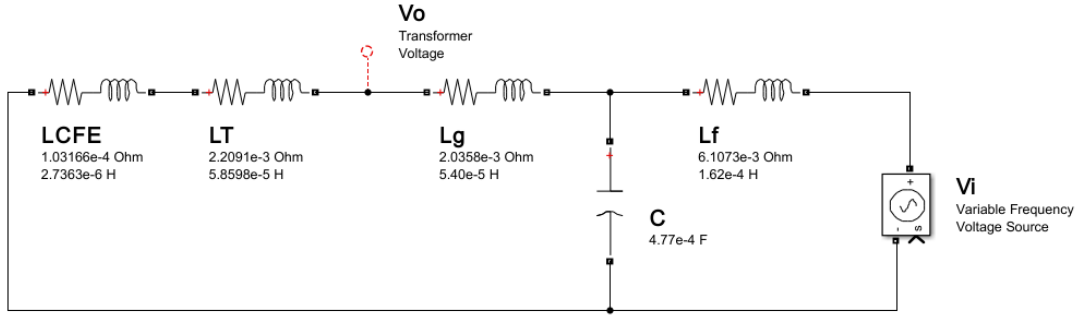


**Figure 4.18.** Single phase equivalent of the harmonic circuit

Reducing the system to its single-phase equivalent it is possible to ascertain the resonant frequency for the system. Combining the transformer and power supply inductance into a single  $L_T$  variable, and disregarding the common-mode capacitance, the grid side of the system may be described:

$$\begin{aligned}
 Y_1 &= j\omega C + \frac{1}{j\omega(L_T + L_g)} = j \left[ \omega C - \frac{1}{\omega(L_T + L_g)} \right] \\
 Y_1 &= j \frac{\omega^2 C(L_T + L_g) - 1}{\omega(L_T + L_g)} \left[ \frac{C(L_T + L_g)}{C(L_T + L_g)} \right] = j \left[ \frac{\omega^2 - \frac{1}{C(L_T + L_g)}}{\frac{\omega}{C}} \right] \\
 Y_1 &= j \frac{C}{\omega} \left( \omega^2 - \frac{1}{C(L_T + L_g)} \right)
 \end{aligned} \tag{4.1}$$

Taking the calculated admittance, the impedance of the whole system is defined by:

$$\begin{aligned}\mathbb{Z}_1 &= j \frac{\omega}{C} \left[ \frac{1}{\frac{1}{C(L_T + L_g)} - \omega^2} \right] \\ \mathbb{Z} &= j\omega \left\{ \frac{1}{C \left[ \frac{1}{C(L_T + L_g)} - \omega^2 \right]} + L_f \right\} = j\omega \left\{ \frac{L_f C \left[ \frac{1}{C(L_T + L_g)} - \omega^2 \right] + 1}{C \left[ \frac{1}{C(L_T + L_g)} - \omega^2 \right]} \right\}\end{aligned}\quad (4.2)$$

Considering the equivalent impedance of the grid side circuit, and remembering both Ohm's and Kirchhoff's laws, the amplification of output (transformer-side) voltage is:

$$\begin{aligned}\mathbb{I}_1 &= \frac{\mathbb{V}}{\mathbb{Z}} & \mathbb{V}_c &= \mathbb{Z}_1 \cdot \mathbb{I}_1 = \mathbb{V} \frac{\mathbb{Z}_1}{\mathbb{Z}} \\ \mathbb{I}_2 &= \mathbb{V}_c \frac{1}{j\omega(L_T + L_g)} & \mathbb{V}_o &= j\omega L_T \left( \frac{\mathbb{V}_c}{j\omega(L_T + L_g)} \right) \\ \frac{\mathbb{V}_o}{\mathbb{V}_{in}} &= \frac{L_T}{L_T + L_g} \left( \frac{\mathbb{Z}_1}{\mathbb{Z}} \right)\end{aligned}\quad (4.3)$$

Substituting the impedance expressions in the ratio and simplifying:

$$\begin{aligned}\frac{\mathbb{Z}_1}{\mathbb{Z}} &= \frac{j \frac{\omega}{C} \left[ \frac{1}{\frac{1}{C(L_T + L_g)} - \omega^2} \right]}{j\omega \left\{ \frac{L_f C \left[ \frac{1}{C(L_T + L_g)} - \omega^2 \right] + 1}{C \left[ \frac{1}{C(L_T + L_g)} - \omega^2 \right]} \right\}} \\ \frac{\mathbb{Z}_1}{\mathbb{Z}} &= \frac{1}{L_f C \left[ \frac{1}{C(L_T + L_g)} - \omega^2 \right] + 1} = \frac{1}{\frac{L_f C [1 - \omega^2 C(L_T + L_g)] + C(L_T + L_g)}{C(L_T + L_g)}} \\ \frac{\mathbb{Z}_1}{\mathbb{Z}} &= \frac{L_T + L_g}{L_f + L_T + L_g - \omega^2 L_f C(L_T + L_g)}\end{aligned}\quad (4.4)$$

Substituting **Equation 4.4** into **4.3**:

$$\begin{aligned}\frac{V_o}{V_{in}} &= \frac{L_T}{L_T + L_g} \left[ \frac{L_T + L_g}{L_f + L_T + L_g - \omega^2 L_f C (L_T + L_g)} \right] \\ \frac{V_o}{V_{in}} &= \frac{L_T}{L_f + L_T + L_g - \omega^2 L_f C (L_T + L_g)}\end{aligned}\quad (4.4)$$

Considering the resonance frequency appears when the denominator becomes zero and undefines the solution, its value can be obtained by the expression:

$$\begin{aligned}\omega_r^2 &= (2\pi f_f h_r)^2 = \frac{L_f + L_T + L_g}{L_f C (L_T + L_g)} \\ h_r &= \frac{1}{2\pi f_f} \sqrt{\frac{L_f + L_T + L_g}{L_f C (L_T + L_g)}}\end{aligned}\quad (4.5)$$

Finally, and when substituting the single-phase equivalents of all reactance values, the resonance frequency value for the Electrolytic Cleaning line main load circuit is found as:

$$\begin{aligned}h_r &= \frac{1}{2\pi(60 \text{ Hz})} \sqrt{\frac{(1.62 \times 10^{-4} \text{ H}) + (6.13 \times 10^{-5} \text{ H}) + (5.40 \times 10^{-5} \text{ H})}{(1.62 \times 10^{-4} \text{ H})(4.77 \times 10^{-4} \text{ F})[(6.13 \times 10^{-5} \text{ H}) + (5.40 \times 10^{-5} \text{ H})]}} \\ h_r &= 14.80 \\ \omega_r &= 887.8222 \text{ Hz}\end{aligned}$$

To verify the theoretical value, the amplification ratio expression (**Equation 4.4**) was given a set of values that included the resonance frequency, and data was plotted through the whole set to have a visual representation of how the circuit behavior changed through the changing frequency values – that graph is found in this document as **Figure 4.19**.

Furthermore, a simulation (pictured in **Figure 4.20**) with the actual elements used in the process model was produced for the sake of a second verification of such data. Using a controlled power source going through a rising frequency slope, the results found in **Figure 4.21** corroborate both the theoretical value and the graph in **Figure 4.19**.

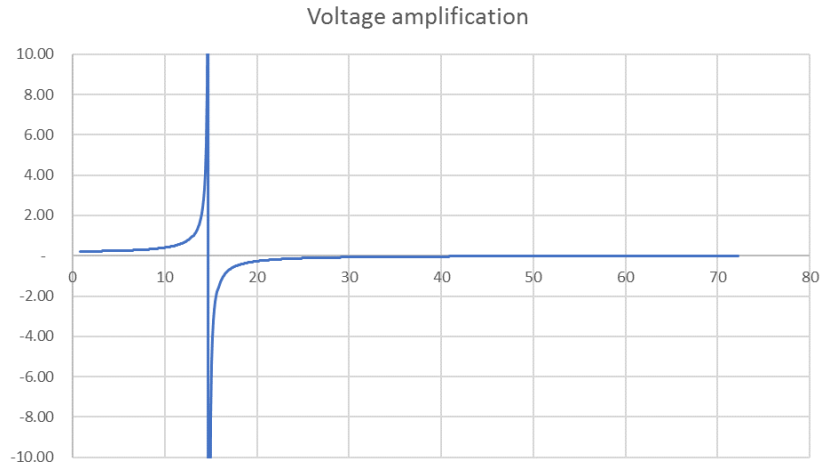


**Figure 4.19.** Voltage amplification according to Equation 4.4

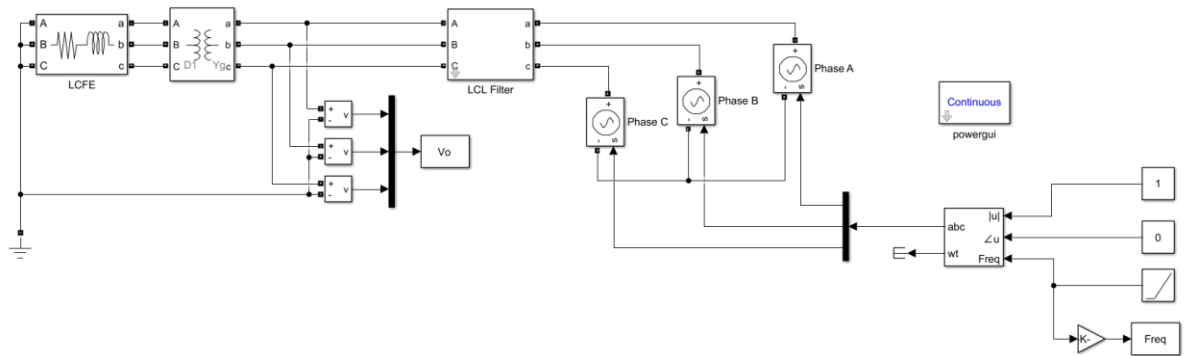


**Figure 4.20.** Frequency response simulation

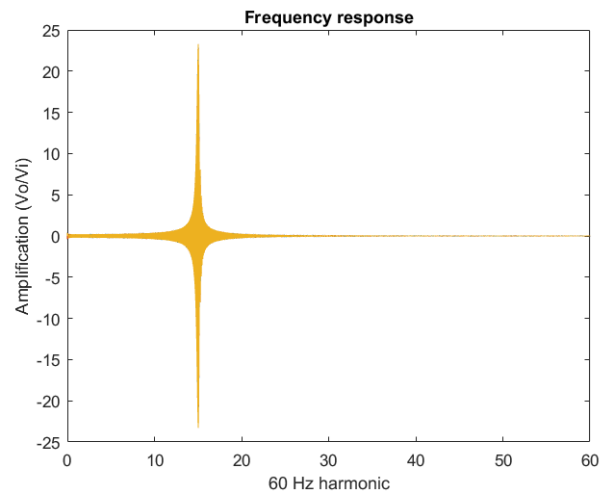


**Figure 4.21.** Frequency response results in Simulink

In light of those findings, an in order to avoid any missing data, a final visit was requested to check the wiring organization that was in place from the transformer to the input side of the Active Front End in the drive room. As **Figure 4.22** shows, after leaving the transformer the wires are divided in triads comprised of all three phases in one package. As four conductors per-phase left the transformer low-voltage side, four triad groups followed the trail to the AFE inputs, where they are all divided by phase again.



**Figure 4.22.** Wire organization at transformer output

Such organization is for the sake of avoiding the creation of an increased magnetic field that would appear by organizing all wiring per-phase, creating a parasitic inductance. Such inductance would hit system performance in the mid-term, as energy would be wasted in the creation of such magnetic field in the form of heat, diminishing the lifetime of the insulation material of the conductors.

As such an arrangement was not found, it was deemed that any additional inductance wouldn't have much of an effect in the modelled system. Which brings to mind the difference between the resonant interharmonic (14.80, 887.82 Hz) and the prevalent harmonic through the ELSPEC data (17<sup>th</sup>, 1.02 kHz), the one with the highest value through the entire period. A possible explanation for this phenomenon involves the rectifier characteristic harmonic spectrum – which includes 13<sup>th</sup> and 17<sup>th</sup>, but no 14<sup>th</sup> naturally – and the fact that the control scheme remains a blackbox. A combination of those two factors makes the possibility of the 17<sup>th</sup> harmonic being excited and amplified instead of the 14.8 harmonic look plausible.

Disregarding that detail, the fact remains that the LCL filter is responsible of the excitation of low-order harmonics, as seen in the simulation and the PQ data, in exchange of filtering the carrier frequency. The fact that almost no 60<sup>th</sup> harmonic is seen in both datasets cements this function.

But the distortion is still a problem. Researchers working at Rockwell, the manufacturer, have published some papers about how to deal with it – reducing the possibilities to three main ones:

- *Passive* damping
- *Active* filtering
- *Hybrid* approach [22]

Active damping requires a higher control bandwidth and sampling rate alongside highly accurate sensors and low propagation delay [23]. This would add needless complexity and increase the cost of the final product to attack a problem that might not need too much resources to be solved. On the other extreme, passive damping simply consists of a resistor put in series with the filter capacitance to dissipate the harmonic content trapped within it, while reducing core loss in the rectifier side inductor [23]. The cost of a such a simple scheme is the reduction of power efficiency of the system by the dissipation done by the resistor, although its effectiveness can be demonstrated with **Figure 4.23**, showing that amplification doesn't occur at the previous resonance frequency.

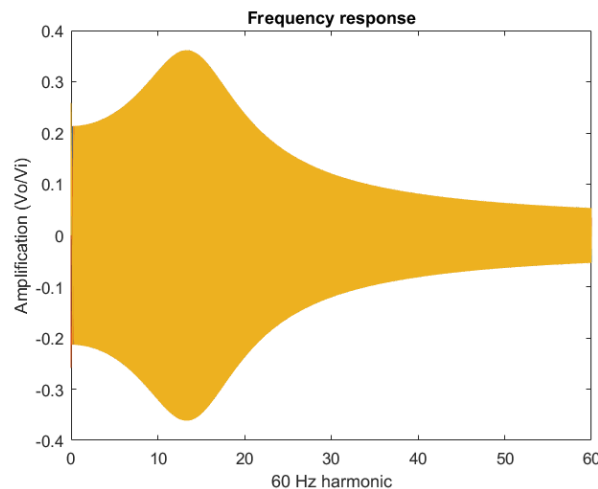


**Figure 4.23.** Damped frequency response

Of course, it doesn't mean that the resistor needs to be connected all the time if unneeded. Rockwell proposed (and patented [28]) the circuit shown in **Figure 4.24**, where a breaker may close or not depending of the harmonic content in the grid side voltages and currents.

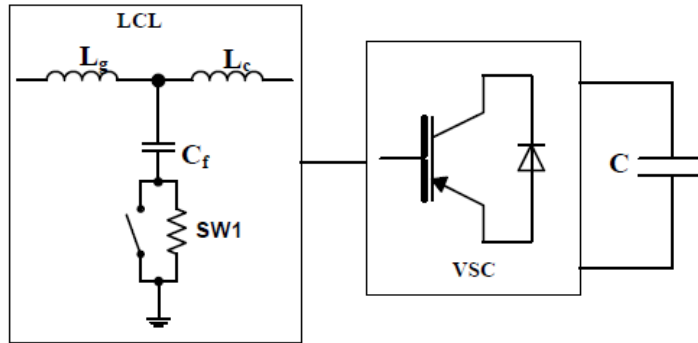


**Figure 4.24.** LCL damping switching circuit

This proposal is realizable in the Electrolytic Cleaning line in Pesquería, as an active approach may be too complicated for its own good, while a hybrid approach would need changing the AFE device as it relies on a virtual resistor scheme made possible by a change in the control characteristics of the rectifier [22].

As for the size of the resistor, its value should not be too big to void the filter action, and it cannot be too small as to draw a high current and further reduce the power efficiency of the system. In this spirit, and to show the difference between the original scheme and the damped one, a damped system two different resistor values were simulated during the initial steps of the reference roll process, with **Figure 4.25**, **4.26**, and **4.27** showing the difference made by the added resistance.

As for the circuit, the simulation not only considered the resistor in series with the filter capacitance, but it also includes the proposed connection to ground of the common-mode capacitors at the grid side of the filter.



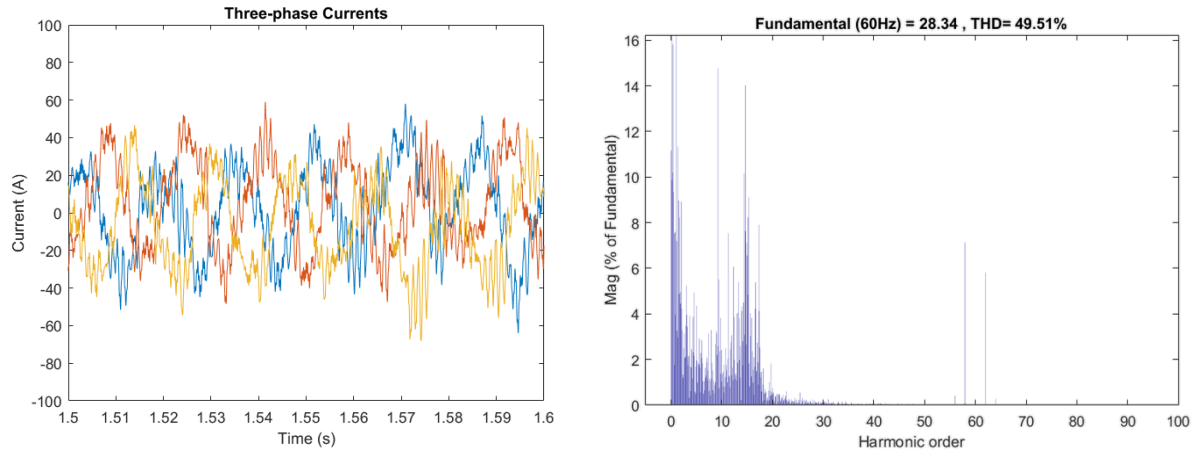


**Figure 4.25.** Currents and harmonic spectrum with no damping resistor

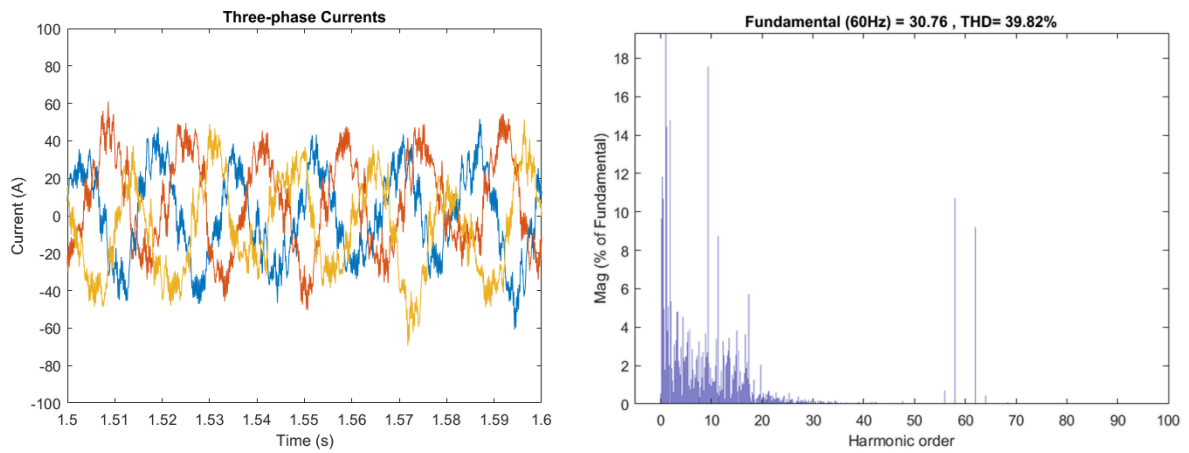


**Figure 4.26.** Currents and harmonic spectrum with 0.1  $\Omega$  damping resistor

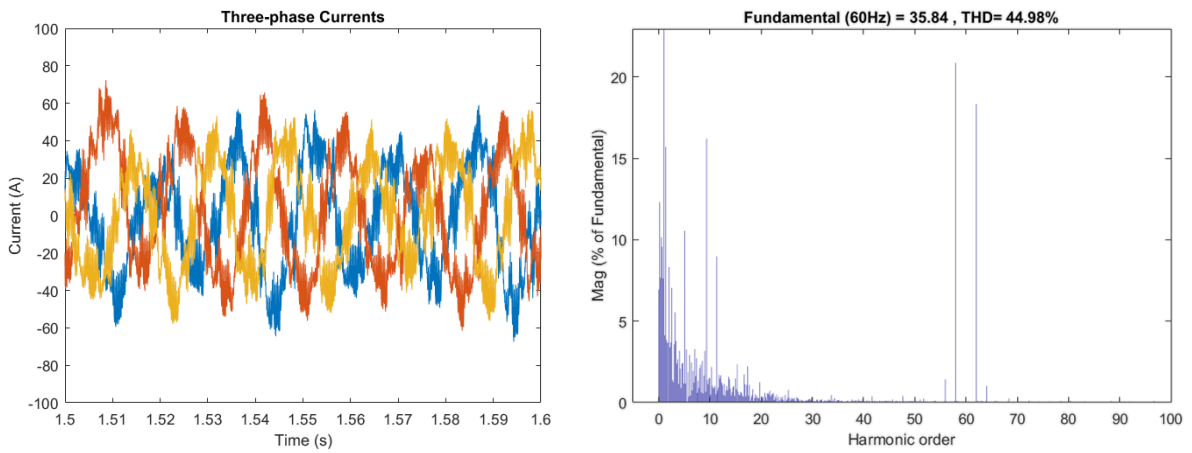


**Figure 4.27.** Currents and harmonic spectrum with a 0.3  $\Omega$  damping resistor

The tradeoff when increasing the resistor value is the appearance of the carrier frequency as an important harmonic component. Also, the power consumed by the damping resistor must be considered as it has a direct impact in the power efficiency of the system. The power taken during a 100 ms sample can be seen in **Figure 4.28**. Considering this, it can be easily understood that an equilibrium must be reached between harmonic distortion requirements and power consumption, chosen in a case-per-case basis.

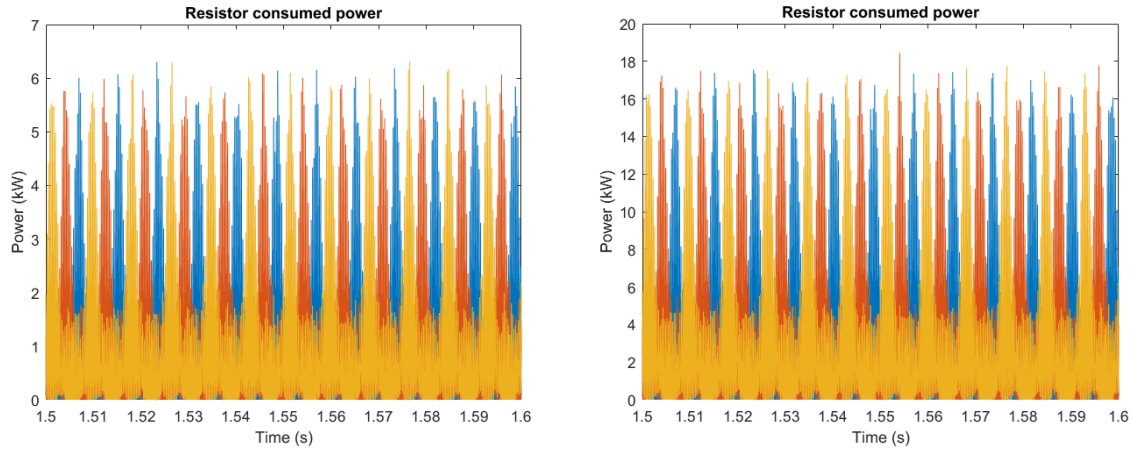


**Figure 4.28.** Three-phase power consumption, 0.1  $\Omega$  and 0.3  $\Omega$  respectively

As for the obtained data, it seems the 0.1  $\Omega$  value in the damping resistance is the most effective one, as it reduces the observed THD in a 10% while the increase of the 60<sup>th</sup> harmonic relevance just raises from 8% to 10% of the fundamental value. Also, and according to the simulation data, the 0.1  $\Omega$  resistor takes less power from the network, with 6 kW peaks compared to the 16 kW ones taken by the 0.3  $\Omega$  one.

## **V. Conclusions and Recommendations**

Considering the main objective of this thesis was both an assessment of the conditions prevalent in the Electrolytic Cleaning line in the Pesquería Industrial Complex, and the creation of a simulated model to understand the interactions between the different variables involved in the control of the main motors of the line, in view of the obtained results this work can be considered a success.

Both the model and the real data support the notion that the main problem is the amount of harmonic distortion in the power supply, which has its effects in the quantity of power wasted by the production of such pollution. The produced model presents a close view to the behavior of the circuit, although the obscuring of the control scheme by the manufacturer inevitably leads to differences between both datasets. Nevertheless, the model is workable by virtue of how it reproduces the operative behavior and its effects on the power source.

The fact that the common-mode capacitors are disconnected from ground in the series LCL filter supplied for the AFE circuit feeding the EC line is perplexing, as from observations in the area such modification doesn't seem in line with the manufacturer recommended practice. This becomes even more questionable when contrasting the prevailing situation in the Pickling line, so grounding those in order for their purpose to be fulfilled might be a good first approach in tackling the harmonic pollution problem.

In a related topic, the possibility of introducing a series resistor with the filter capacitance embedded to the mentioned LCL filter has been demonstrated to work in the reduction of harmonic components in the current waveforms, so an implementation of such modification is recommended. With it comes a series of contrasting priorities between the actual physical space available for such modification, the power that would be consumed by its addition and its impact on power efficiency, and the reduction of harmonic distortion. A middle ground must be found to achieve an improved performance of the machine.



## **VI. Future Work**

The main source of disconnect between simulation and the real circuit is the control scheme used by the manufacturer. It would be advisable in further work to detail in a closer manner to reality such algorithm to completely verify the validity of the complete model.

Also, as noted during the results chapter, the computing power available was a crutch for the simulation at large, needing to modify the raw data from the simulation in order to be able to manipulate it with ease, so an increased amount of resources would be a boon for the model. It would make plausible the change of the step size used through the simulation, improving the control behavior of the loads.

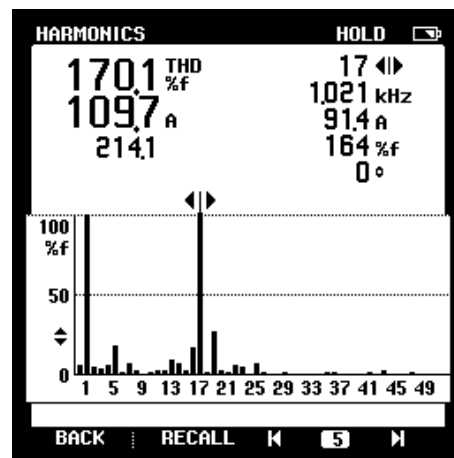
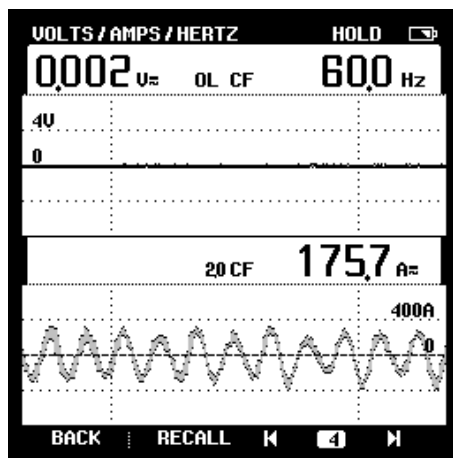
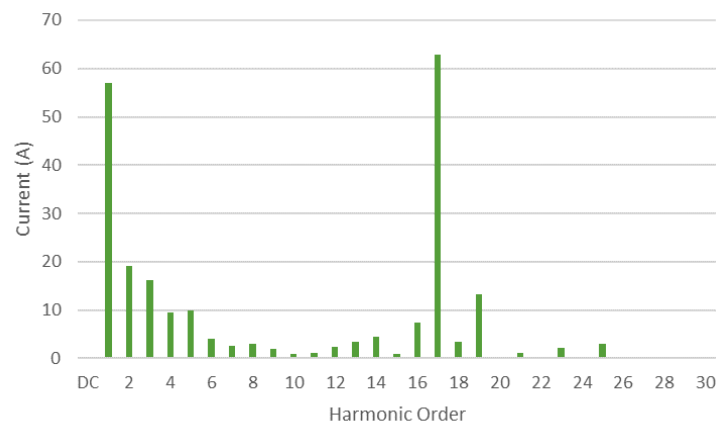
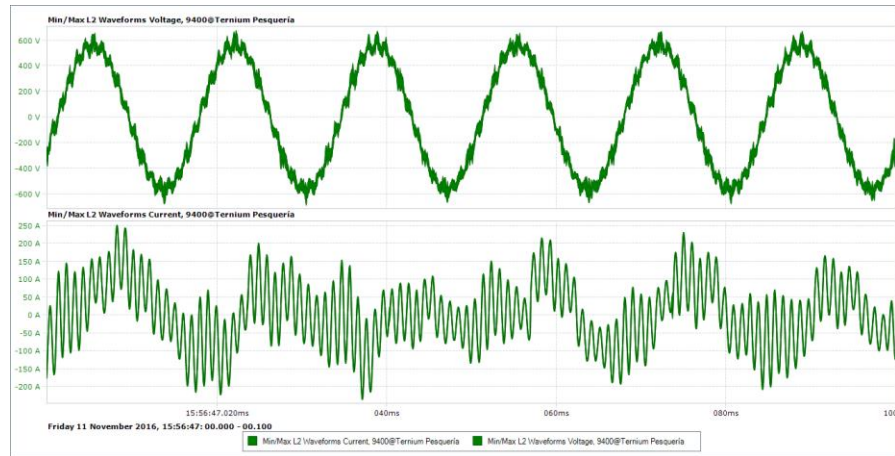
As a final comment, some data initially considered for this work was ultimately dismissed because of time constraints. Introducing concepts such as the impact of the length of the wiring from the drive systems to the motor loads, the power loss model of such conductive materials, and the filters implemented to reduce and/or eliminate their impact would paint a more comprehensive image of the process happening while a roll is going through the Electrolytic Cleaning line at Ternium Pesquería.



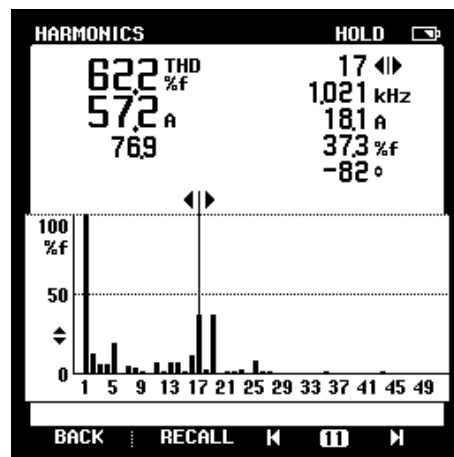
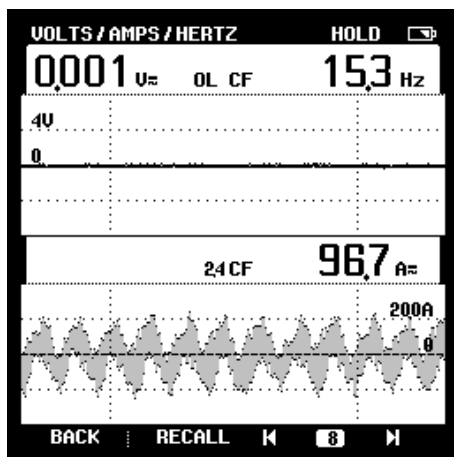
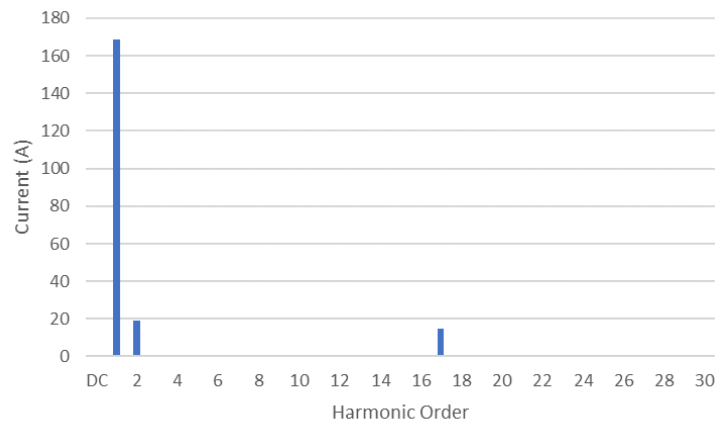
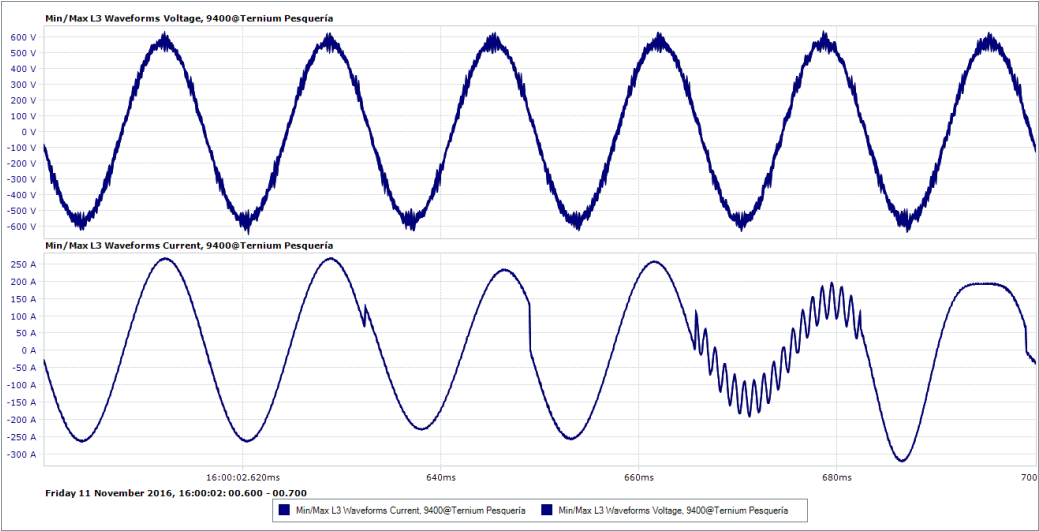
## Annex I

### ELSPEC Verification Data

#### Phase B



Phase C

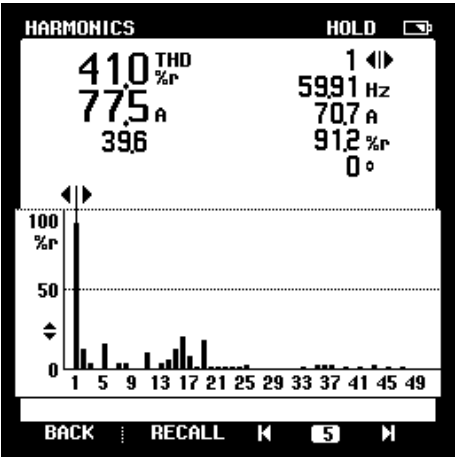
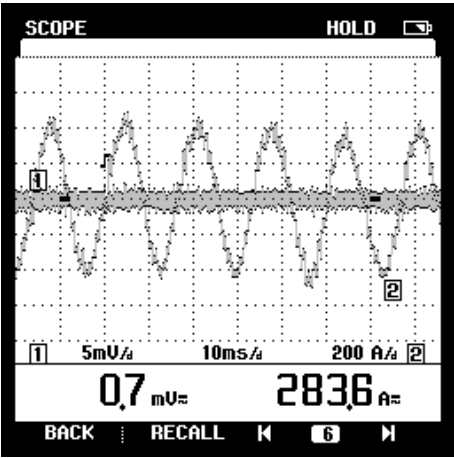




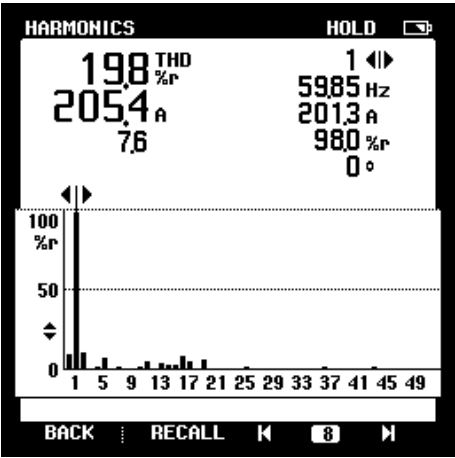
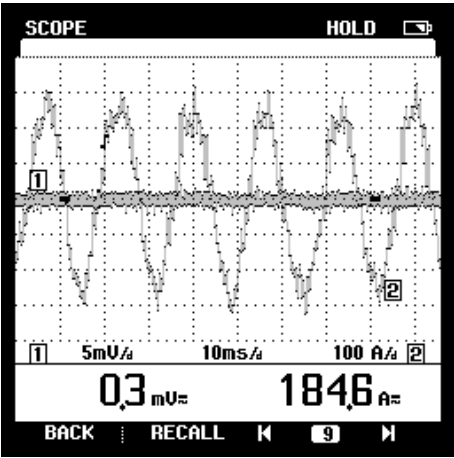
Annex II

Pickling Line Waveform Data

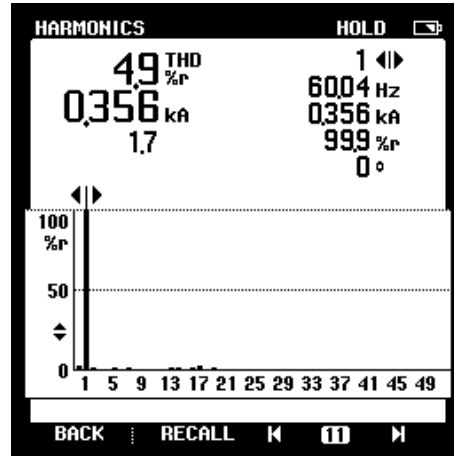
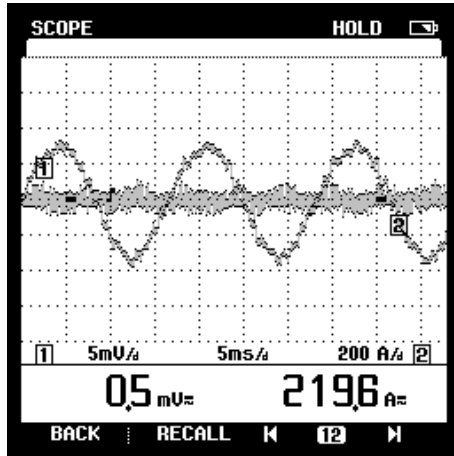
690V System, Phase B



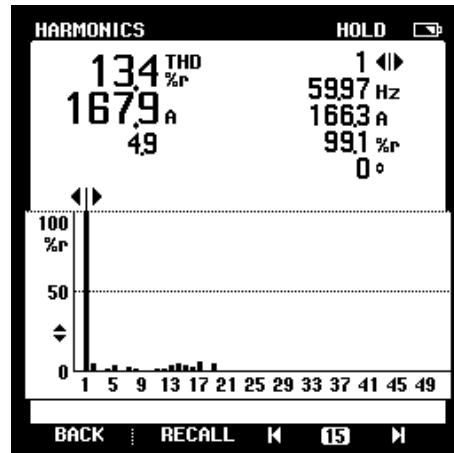
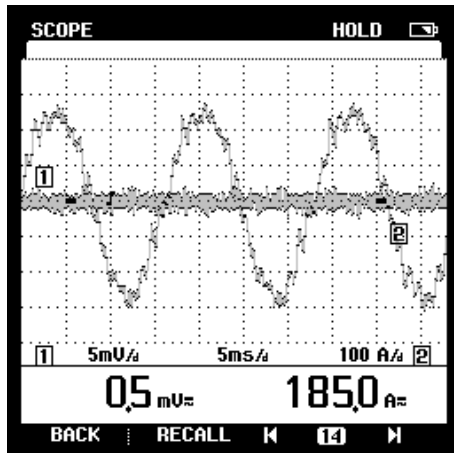
690 V System, Phase C



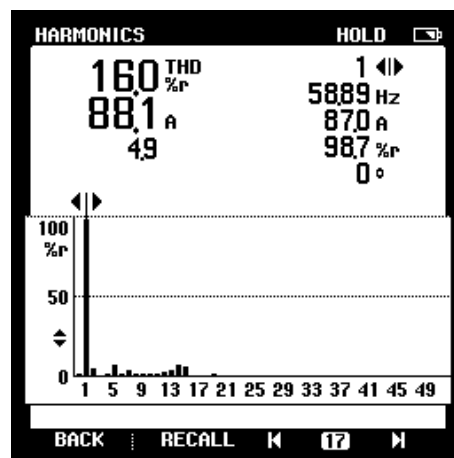
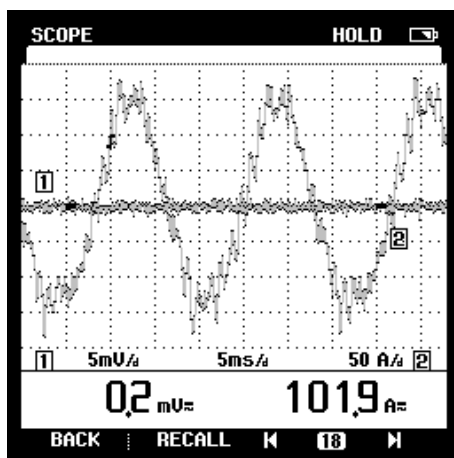
480 V System, Phase A



480 V System, Phase B



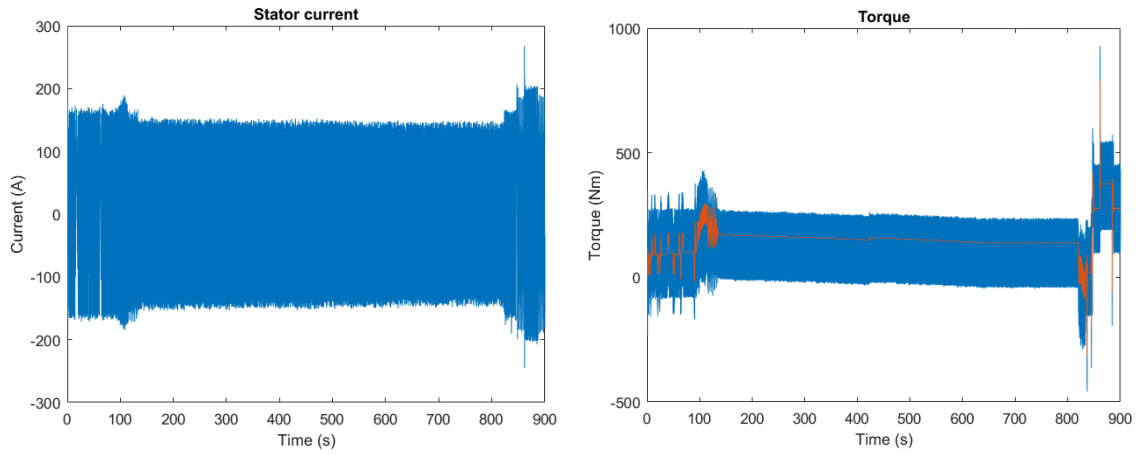
480 V System, Phase C



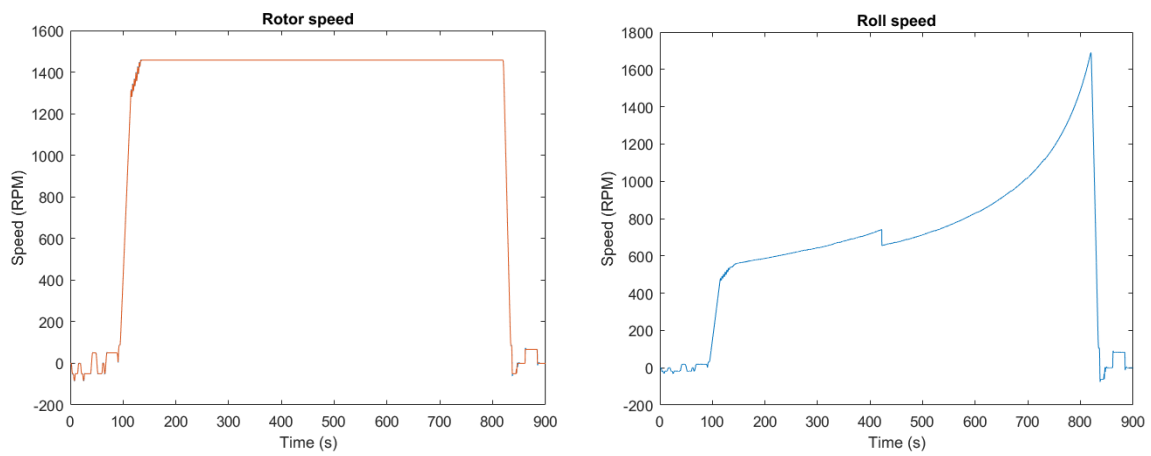
## Annex III

### Load Simulation Results

*Pay Off Reel*

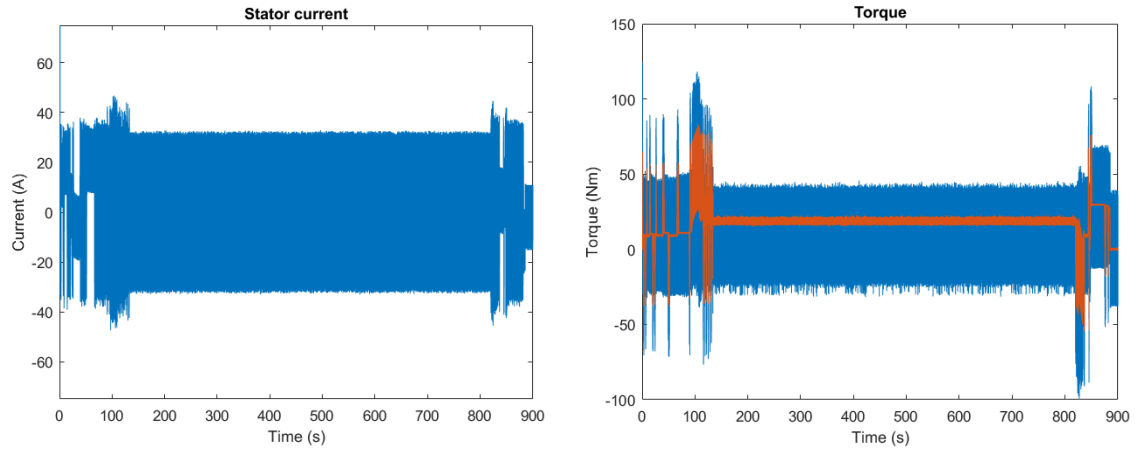


Stator current and Generated torque

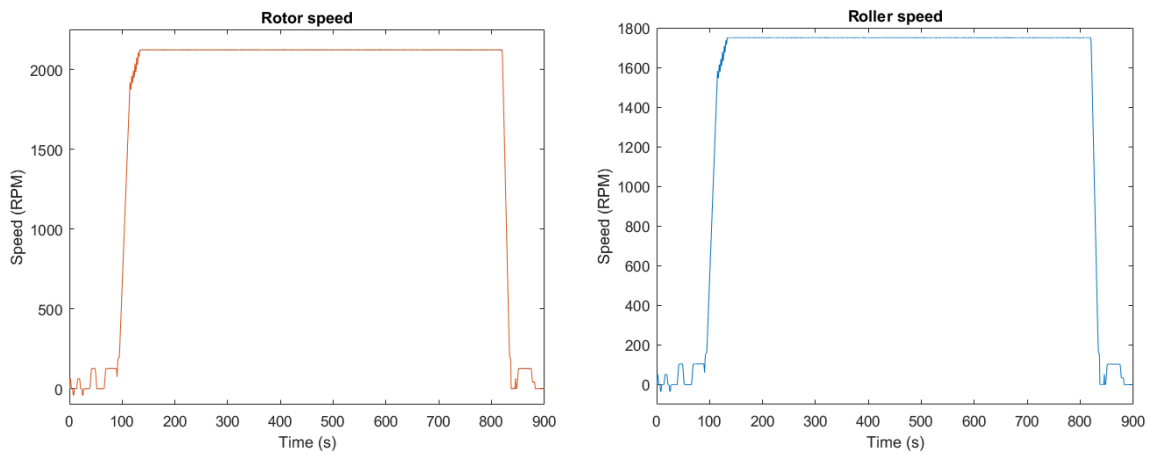


Rotor and roll speed

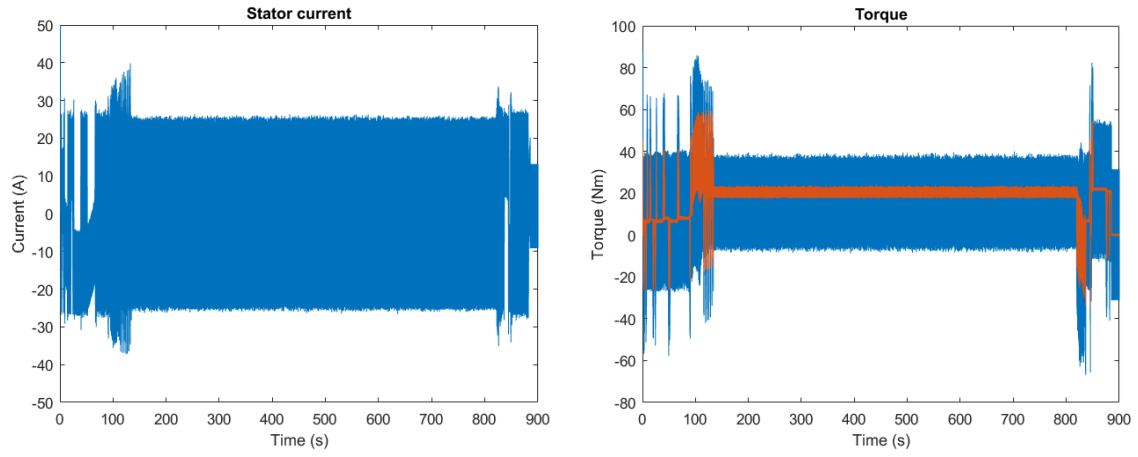
## Bridle Roll 1 Unit 1



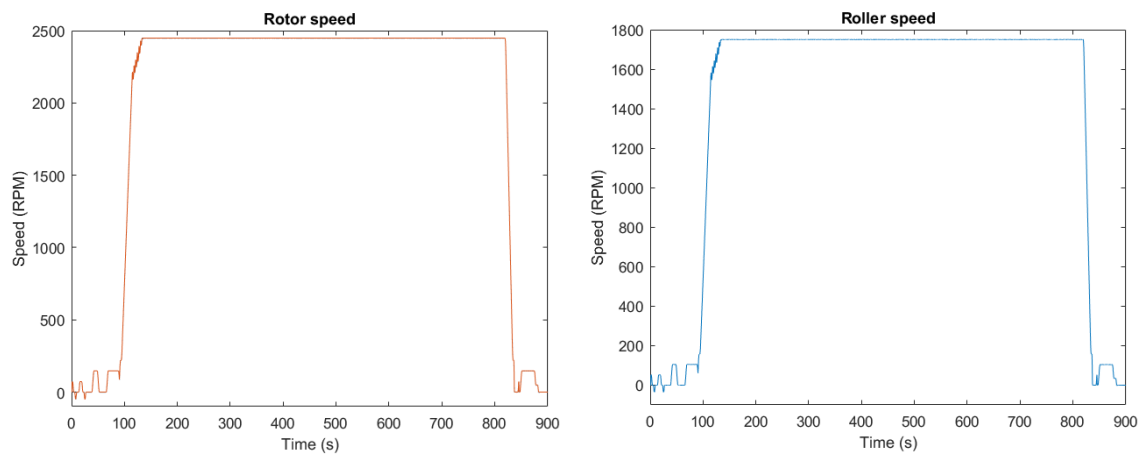
Stator current and Generated torque



Rotor and roller speed

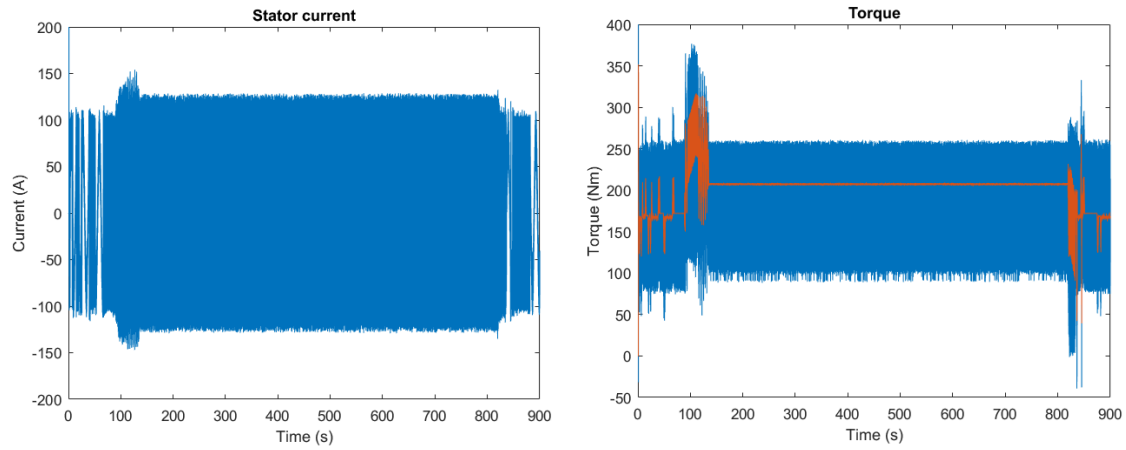


Stator current and Generated torque

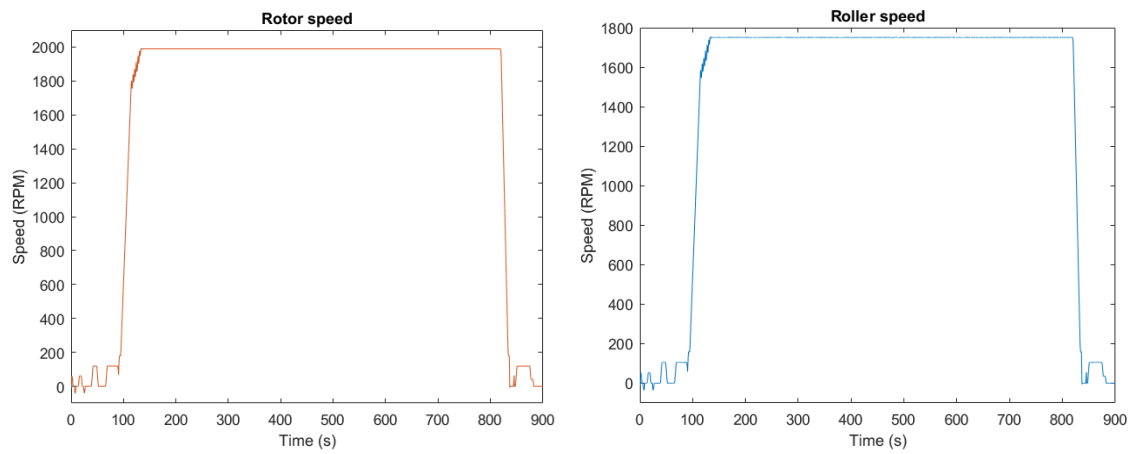


Rotor and roller speed

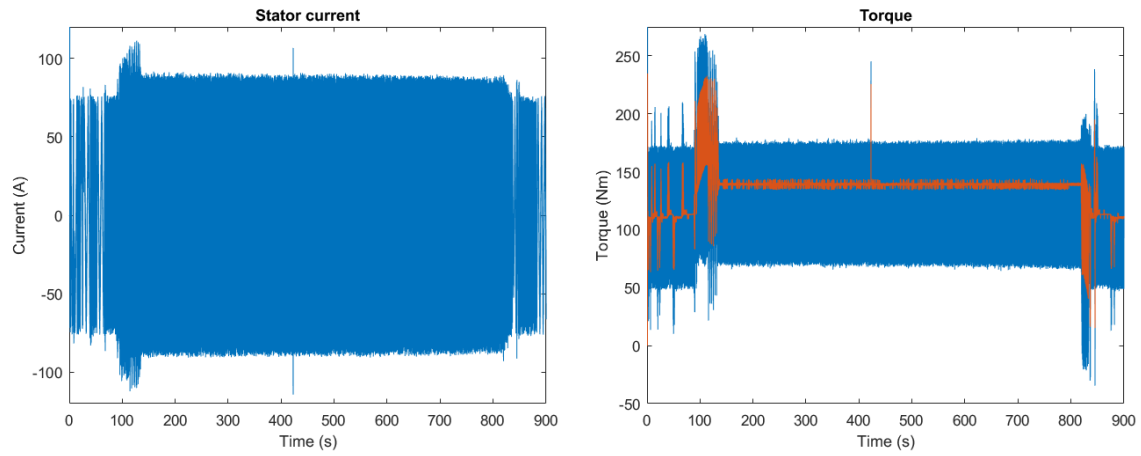
## Bridle Roll 2 Unit 1



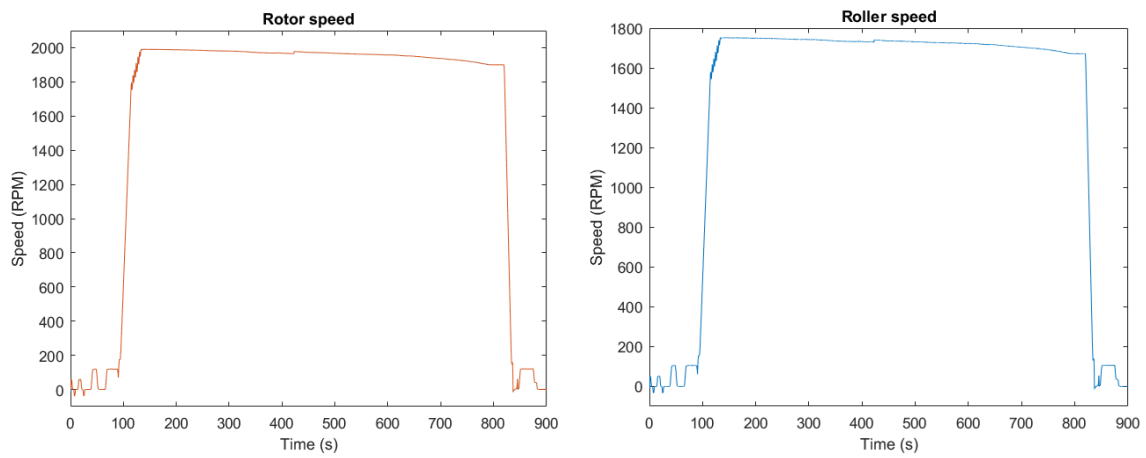
Stator current and Generated torque



Rotor and roller speed



Stator current and Generated torque



Rotor and roller speed





## References

- [1] ABB drives – Technical guide book, 2014.
- [2] H. Abu-Rub, *High performance AC drives with Matlab*, 1st ed. Oxford: Wiley-Blackwell, 2012.
- [3] B. A. Acharya and V. John, "Common mode DC bus filter for Active Front-End converter", *2010 Joint International Conference on Power Electronics, Drives and Energy Systems & 2010 Power India*, 2010.
- [4] F. Blaabjerg and J. Pedersen, "An integrated high power factor three-phase AC-DC-AC converter for AC-machines implemented in one microcontroller", *Proceedings of IEEE Power Electronics Specialist Conference - PESC '93*, 1993.
- [5] P. Brogan and R. Yacamini, "Harmonic control using an active drive", *IEE Proceedings - Electric Power Applications*, vol. 150, no. 1, p. 14, 2003.
- [6] G. Di Napoli, "Use of Active Front End to increase power quality", *2016 International Symposium on Power Electronics, Electrical Drives, Automation, and Motion (SPEEDAM)*, 2016.
- [7] Aswathi G., S. Nalini, and R. Sudeep Kumar, "Simulation of Active Front End Converter Based VFD for Induction Motors", *International Journal of Scientific & Engineering Research*, vol. 4, no. 6, p. 322-327, 2013.
- [8] J. He, Z. Vrankovic, P. Ozimek, and C. Winterhalter, "Investigation of common mode current related dc-bus overvoltage in multiple converter systems", *2016 IEEE Applied Power Electronics Conference and Exposition (APEC)*, 2016.
- [9] D. Holmes and T. Lipo, *Pulse width modulation for power converters*, 1st ed. Hoboken, N.J.: Wiley-Interscience, 2003.
- [10] *IEEE Recommended Practice and Requirements for Harmonic Control in Electric Power Systems*, 1st ed. New York: Institute of Electrical and Electronics Engineers, 2014.
- [11] *IEEE Recommended Practice for Monitoring Electric Power Quality*, 1st ed. New York: Institute of Electrical and Electronics Engineers, 2009.
- [12] V. John, B.A. Acharya, S. Murthy, M.H. Hedayati, and T. Saboo, "Filters for Active Front End Drives", *Tech Report – ISTC HH*, 2012.
- [13] P. Jonas, "Comparing harmonics mitigation techniques", *EE Publishers*, 2014. [Online]. Available: <http://www.ee.co.za/article/comparing-harmonics-mitigation-techniques.html>.

- [14] M. Liserre, F. Blaabjerg, and S. Hansen, "Design and control of an LCL-filter based three-phase active rectifier", *Conference Record of the 2001 IEEE Industry Applications Conference. 36th IAS Annual Meeting (Cat. No.01CH37248)*.
- [15] A. Llamas, *Armónicas en sistemas eléctricos industriales*, 1st ed. México: Innovación Editorial Lagares, 2004.
- [16] A. Llamas, "Sesión #1 - Disturbios eléctricos", Tecnológico de Monterrey, Campus Monterrey, 2016.
- [17] F. Luo and H. Ye, *Power electronics*, 1st ed. Boca Raton: CRC Press/Taylor & Francis, 2010.
- [18] Hydro-Québec, *SimPowerSystems User's Guide R2013a*, 25th ed. United States: The MathWorks, 2013.
- [19] L. Moran, J. Espinoza, M. Ortiz, J. Rodriguez, and J. Dixon, "Practical problems associated with the operation of ASDs based on active front end converters in power distribution systems", *Conference Record of the 2004 IEEE Industry Applications Conference, 2004. 39th IAS Annual Meeting*.
- [20] A. Ndokaj and A. Di Napoli, "Behavior of an Active Front End in presence of voltage sags", *2014 International Symposium on Power Electronics, Electrical Drives, Automation and Motion*, 2014.
- [21] P.P. Pandit, "Modeling and Analysis of Active Front-End Induction Motor Drive for Reactive Power Compensation", Master's Thesis, University of Tennessee, 2005.
- [22] Y. Patel, A. Ahmed and L. Wei, "Hybrid damping for active front end converter", *2016 IEEE Energy Conversion Congress and Exposition (ECCE)*, 2016.
- [23] Y. Patel, L. Wei and A. Nasiri, "LCL filter resonance mitigation technique for voltage source converters", *2014 International Conference on Renewable Energy Research and Application (ICRERA)*, 2014.
- [24] D. Rathod and M. Shah, "Modelling and simulation of front end converter for power quality improvement", *2016 International Conference on Electrical, Electronics, and Optimization Techniques (ICEEOT)*, 2016.
- [25] Rockwell Automation, "PowerFlex Active Front End User Manual", 2014.
- [26] Rockwell Automation, "PowerFlex 700S High Performance AC Drive", 2014.
- [27] Rockwell Automation, "Straight Talk about PWM AC Drive Harmonic Problems and Solutions", *Technical Paper*, 2006.

- [28] Rockwell Automation Technologies, Inc., "LCL Filter Resonance Mitigation Technique for Voltage Source Converters", US 2016/0013715 A1, 2016.
- [29] Siemens Industry Inc., "Harmonics in power systems: Causes, effects and control", *Whitepaper*, 2013.
- [30] J. Siva Prasad, T. Bhavsar, R. Ghosh, and G. Narayanan, "Vector control of three-phase AC/DC front-end converter", *Sadhana*, vol. 33, no. 5, pp. 591-613, 2008.
- [31] Ternium, *Proceso Productivo*. 2015.
- [32] U.S. Energy Information Agency, "International Energy Outlook 2016", 2016.
- [33] Vacon Plc., "Active Front End (AFE) User Manual", 2015.
- [34] P. Waide and C. Brunner, "Energy-Efficiency Policy Opportunities for Electric Motor-Driven Systems", *IEA Energy Papers*, 2011.
- [35] E. Worrell, P. Blinde, M. Neelis, E. Blomen, and E. Masanet, "Energy Efficiency Improvement and Cost Saving Opportunities for the U.S. Iron and Steel Industry," *U.S. Environmental Protection Agency*, 2010.



## **Curriculum Vitae**

César Suárez was born in Monterrey, N.L., Mexico in 1992. He received his B.S. in Mechatronics Engineering from the Facultad de Ingeniería Mecánica y Eléctrica of the Universidad Autónoma de Nuevo León in June 2014, obtaining the Academic Merit for obtaining the best grades in his generation. With the support and a scholarship from Ternium México he began his M.Sc. in Energy Engineering degree at Instituto Tecnológico y Estudios Superiores de Monterrey in August 2015 as one of the students of the Industrial Consortium to Foster Applied Research and Technological Development in Mexico. During his stay, his research focused on Power Quality issues at an Electrolytic Cleaning process used in the steelmaking industry.

This document was typed in using Microsoft Word by César Eduardo Suárez Guerrero.